THE UNIVERSITY OF TOKYO

Evolution of Population III Very Massive Stars with Mass Accretion

A DISSERTATION SUBMITTED TO
THE SCHOOL OF SCIENCE
IN CANDIDACY FOR THE DEGREE OF
DOCTOR OF PHILOSOPHY

DEPARTMENT OF ASTRONOMY

BY
TAKUYA OHKUBO

TOKYO, JAPAN
DECEMBER, 2008

Adviser:
Prof. Ken'ichi Nomoto : The Institute for the Physics and Mathematics of the Universe, University of Tokyo

Committee in charge:

Prof. Toshikazu Shigeyama (Chair) : Research Center for the Early Universe, School of Science, University of Tokyo

Prof. Hiroyasu Ando : National Astronomical Observatory

Prof. Yoshiharu Eriguchi : Department of Earth Science and Astronomy, Graduate school of Arts and Sciences, University of Tokyo

Prof. Toshitaka Kajino : National Astronomical Observatory

Prof. Hirokazu Yoshimura : Department of Astronomy, School of Science, University of Tokyo

ACKNOWLEDGMENTS

First of all, I would like to express my sincere gratitude to my supervisor, Prof. Ken'ichi Nomoto, for introducing me to this wonderful world of theoretical astronomy. He has helped, advised, and encouraged me in many aspects, not only on specialty in research, but also on attitude important to perform scientific research. Without his help, I would never have been through doctoral course and completed this thesis.

There are also many people who have helped me to complete this thesis. I would like to thank Dr. Chiaki Kobayashi, Dr. Takayoshi Nakamura, and Ms. Marii Shirouzu for firstly teaching me how to operate computer machines and basic backgrounds of astronomy, which I was not familiar with. Without their helps, I would have hesitated to even enter this field.

I wish to thank Prof. Hideyuki Umeda, Dr. Keiichi Maeda, Prof. Naohito Nakasato, Dr. Tomoharu Suzuki, Dr. Nobuyuki Iwamoto, Dr. Takashi Yoshida, Dr. Shinya Wanajo, Prof. Yuuri Ishimaru, Dr. Jinsong Deng for mentoring me and giving useful advice, especially since I entered graduate school and started my own research. Prof. Umeda kindly provided me with stellar evolution code and nucleosynthesis code and how to operate them. Dr. Maeda gave me many useful comments about my research, presentation, and paper drafts. Prof. Nakasato and Dr. Suzuki administered computers for calculation, and I learned a lot about computer knowledge from them. Dr. Iwamoto, Dr. Yoshida, Dr. Wanajo, Prof. Ishimaru, and Dr. Deng gave me useful advice in seminars. Dr. Yoshida also improved nucleosynthesis code. I would thank Dr. Nozomu Tominaga, Mr. Masaomi Tanaka, Mr. Tatsuhiro Uenishi, Ms. Szeting Chan for useful discussion. They did help me a lot not only on research but also on private things. They made my graduate school life enjoyable. Mr. Takami Kuroda, Mr. Yasuomi Kamiya, Ms. Natsuko Izutani also discussed many topics with me.

I am also indebted to many people outside the laboratory, in Japan or foreign countries. Prof. Naoki Yoshida kindly provided me with his results of cosmological simulation, which is directly related to this thesis, and gave me many useful suggestions. Prof. Sachiko Tsuruta discussed an interesting field of intermediate mass black holes with us, and checked my English expression in my articles. Prof. Martin J. Rees gave us useful comments on cosmological reionization from the standpoint of cosmology. These suggestions enriched my research and helped me broaden my

horizon.

I would thank my thesis committee members, Prof. Toshikazu Shigeyama, Prof. Hiroyasu Ando, Prof. Yoshiharu Eriguchi, Prof. Toshitaka Kajino, Prof. Hirokazu Yoshimura, for reading this thesis and giving me helpful suggestions to improve this thesis.

Financial supports from many organizations were very important. The grant from the laboratory, 21st global COE program, and Japan Society for the Promotion of Science (JSPS) supported me financially to travel for attending conferences, purchase machines. Incentive wages from them also supported my life.

Finally, I would express my appreciation to all people related to me through my daily life. I especially thank my parents for letting me go to graduate school and supporting my life. I also thank Dr. Hiromitsu Takayanagi for giving me a chance to start thinking my career path after Ph.D course.

ABSTRACT

In this thesis, we calculate the evolution of population III (Pop III) stars whose masses grow from the initial masses of $\sim 1 M_\odot$ by accreting the surrounding gases. My calculations cover all evolutionary stages from the pre-main sequence, via various nuclear burning stages, through the final core collapse or pair-creation instability phases. We calculate models with various mass accretion rates: (1) constant accretion rates throughout the evolution, (2) stellar mass dependent accretion rates which are derived from cosmological simulations of early structure formation (Pop III.1 stars) based on the low mass dark matter halos at redshifts $z \sim 20$, (3) mass dependent accretion rates which are affected by radiative feedback, (4) mass dependent accretion rates for zero-metallicity but second generation (Pop III.2) stars which are affected by radiation from the first generation (Pop III.1) stars. The evolutions of massive stars without mass accretion are also calculated and compared with the results of mass accreting models.

This thesis focuses mainly on the following two points: (I) the influences of mass accretion on the final fate, and (II) the later evolution stages after central helium burning of Pop III massive stars. We unveil these aspects and summarize my findings as follows.

(I) Final stellar masses, and the final fates

We find that unless the accretion rate is significantly reduced by feedback effects, the final stellar mass $M_{\rm f}$ can be even as large as $M_{\rm f} \gtrsim 300 M_\odot$. Such a massive star undergoes core collapse and would form an intermediate mass black hole (IMBH). Compared with the non accreting models whose masses are almost equal to the final masses of $M_{\rm f}$, the mass accreting stars have the following features. (i) The stellar lifetime is longer because the stellar mass is smaller during hydrogen burning. (ii)The CO core masses are smaller because M is smaller and still increasing during helium burning. (iii) However, these differences are too small to significantly change the final fates of stars as a function of $M_{\rm f}$. Therefore, we expect that the pair instability supernovae (PISNe) mass range hardly changes.

The final mass of Pop III.1 stars can be very large ($M \gtrsim 300 M_\odot$), beyond the PISNe mass range. Such massive stars form IMBHs, which may be the seeds for merger tree to supermassive black holes. On the other hand, Pop III.2 stars are less massive ($M \lesssim 40-60 M_\odot$), being in the mass range of ordinary iron core-collapse stars.

Such stars explode and eject heavy elements to contribute to chemical enrichment of the early universe. The stars in this mass range are favorable candidates for elemental origin of extremely metal-poor stars in the Galactic halo. We can explain why the signature of PISNe are not seen with the scenario that Pop III.1 stars are very massive, i.e., $M \gtrsim 300 M_\odot$ and Pop III.2 stars are less massive, i.e., $M \lesssim 40 - 60 M_\odot$, although there is some uncertainty in radiative feedback. Verification of existence of CVMS and IMBH are expected by future detection of neutrino or gravitational wave emitted along with the collapse of CVMS, and gravitational wave radiation along with the merging of binary IMBHs.

(II) Later evolutionary stages after helium burning

There are many previous works in Pop III stellar evolution for each mass range. However, most of such calculations have been carried out only through the stage before the end of central helium burning, and only few calculations have been performed until late stages of oxygen, silicon burning, and pre-core-collapse. The detailed study of the characteristics of such late stages of evolution for stars with $M \gtrsim 300 M_\odot$ and $M \sim 100 M_\odot$ is also one of the purpose of this thesis.

For very-massive stars, carbon does not ignite until the central temperature exceeds 10^9 K. During core collapse, the silicon layer and iron core grow in mass considerably, and then the final size of the iron core is much larger than for ordinary massive stars due to the explosive oxygen and silicon shell burnings. On the other hand, less massive stars ($M \lesssim 140 M_\odot$), oxygen and silicon shell burnings occurs stably and the burning time scale is much longer than collapse time scale. As a result, the iron core and the silicon layer are small to the whole mass.

For stars in the mass range $80 M_\odot \lesssim M \lesssim 140 M_\odot$ the CO core oscillates during oxygen and silicon burnings. The amplitude is larger and oscillation period is longer for more massive models. This phenomenon is typical for this mass range, and occurs even if metallicity is not zero. Such stars are considered as origin of very bright supernovae.

TABLE OF CONTENTS

CHAPTER 1
INTRODUCTION

One of the most interesting challenges in astronomy is to investigate the mass and properties of first generation "Population III (Pop III)" stars, and how various elements have been synthesized in the early universe. Just after the Big Bang these elements were mostly only H, He and a small amount of light elements (Li, Be, B, etc). Heavier elements, such as C, O, Ne, Mg, Si and Fe, were synthesized during the evolution of later generation stars, and massive stars exploded as supernovae (SNe), releasing heavy elements into space.

It is very important to find how massive Pop III stars are. It has been suggested that the initial mass function (IMF) of Pop III first stars may be different from the present one - that more massive stars existed in the early universe (e.g., Nakamura & Umemura 1999; Abel, Bryan, & Norman 2000; Omukai & Palla 2003). Some authors (e.g., Wasserburg & Qian 2000; Qian, Sargent, Wasserburg 2002a; Qian & Wasserburg 2002b; Yoshida et al. 2006) argued that the existence of very massive stars (VMSs) in the early universe is consistent with the abundance data of Lyα systems. Numerical simulations by, e.g., Bromm & Loeb (2004), indicate that the maximum mass of Pop III stars to be formed will be $\sim 300M_{\odot}$ – $500M_{\odot}$. Omukai & Palla (2003), however, point out that under certain conditions VMSs much heavier than $300M_{\odot}$ can be formed in the zero-metallicity environment. Tan & McKee (2004) calculated star formation by taking rotation and disk structure and concluded that first stars should be much more massive than $30M_{\odot}$. Another scenario for the formation of VMSs for any metallicity has been presented by Ebisuzaki et al. (2001); Portegies Zwart et al. (1999, 2004a); Portegies Zwart (2004b), where VMSs are formed by merging of less massive stars in the environment of very dense star clusters.

1.1 Formation of first generation stars

The current standard ΛCDM model suggests that cosmological structure was built up hierarchically from smaller scales (bottom-up scenario; Kirshner 2003; Ostriker & Steinhardt 2003). Slight density fluctuations at the beginning of the universe are the seeds for the structure formation. According to this scenario, smaller objects such as stars formed first and then larger structures such as galaxies are built. The

exact epoch when first generation stars formed is not determined. Theoretically the standard ΛCDM model predicts that it is $z \sim 30$ (Couchman & Rees 1986) whereas observationally the WMAP data suggests that it is $z \sim 10$ (Sanchez et al. 2006; Spergel et al. 2007).

It is dark matter that plays an important role for the formation of first generation stars. Dark matter gathers due to gravity and forms minihalos and the typical mass is $\sim 10^6 M_\odot$ (Haiman et al. 1996; Tegmark et al. 1997; Fuller & Couchman. 2000). After the formation of minihalos, the baryon gas collapses gravitationally to form a star. Since the primordial gas contains no heavy elements, the efficient coolant indispensable for star formation by collapse is molecular hydrogen H_2 (Peebles & Dicke. 1968; Matsuda, Sato, & Takeda. 1969; Palla, Salpeter, & Stahler 1983).

There are many numerical studies for the formation of first stars from cosmological simulations: one-dimension studies (Haiman et al. 1996, Omukai & Nishi 1998; Nakamura & Umemura 2002; Ahn & Shapiro 2007) or three dimension studies (Abel, Bryan, & Norman 2000, 2002; Bromm, Coppi, & Larson 1999, 2002; Bromm & Larson 2003; Fuller & Couchman. 2000; Yoshida et al. 2003, 2006; O'Shea & Norman 2006a,b; Gao et al. 2007; Yoshida et al. 2008). The typical mass of a primordial gas cloud is $\sim 10^3 M_\odot$ (Abel et al.2000, 2002; Bromm et al.1999, 2002; Tsuribe & Inutsuka 2001). In the central region of the cloud, a protostellar core ($\sim 10^{-3} M_\odot$) is formed (Omukai & Nishi 1998) and then the gas surrounding this core accretes onto it. The stellar mass increases eventually.

The accretion rate is an important factor to determine the typical mass of Pop III stars. It is evaluated from the cosmological simulation. Many authors (Abel et al.2002; Yoshida et al. 2006; Gao et al. 2007) pointed out that the accretion rate is as high as $\sim 10^{-2} M_\odot$/yr when the core mass is small ($M \lesssim 10 M_\odot$) and it decreases with increasing core mass. These studies suggest that first stars might be more massive than $100 M_\odot$. Omukai & Palla (2003) calculated protostar evolution with constant accretion rates. They treat the accretion rate as a free parameter and set it the order of $10^{-2} M_\odot$/yr and obtained that the final mass could be over $300 M_\odot$. Tan & McKee (2004) calculated star formation by including rotation and disk structure and concluded that first stars should be heavier than $30 M_\odot$.

1.2 Evolution of different mass stars and their fates

Stars end their lives differently depending on their initial masses M. Here the Pop III stars are assumed to undergo too little mass loss to affect the later core evolution (without mass accretion or mass loss, e.g. Bond et al. 1984; Heger et al. 2001, 2003; Ohkubo et al. 2006). Then the fates of such stars are summarized as follows. Those stars lighter than $8M_\odot$ form white dwarfs. Those with $8M_\odot$ – $140M_\odot$ undergo ONe-Fe core collapse at a last stage of their evolution leaving neutron stars or black holes. Some of these stars explode as the core-collapse supernovae. Stars with $140M_\odot$ – $300M_\odot$ undergo electron-positron pair creation instability during oxygen burning, releasing more energy by nuclear burning than the gravitational binding energy of the whole star, and hence these stars disrupt completely as the pair-instability supernovae (PISN). Stars with $300M_\odot$ - $10^5 M_\odot$ also enter into the pair-instability region but continue to collapse. Fryer et al. (2001) calculated evolution of 260 and 300 $M_\odot$ stars and obtained the result that a 260 $M_\odot$ star ends up as a PISN and a 300 $M_\odot$ star collapsed. Stars over $\sim 10^5 M_\odot$ collapse owing to general relativistic instability before reaching the main-sequence. The core collapse SNe (Type II, Ib and Ic SNe) release mainly α-elements such as O, Mg, Si and Ca and some Fe-peak elements as well.

In the present paper, we call the stars with $M \gtrsim 10^5 M_\odot$ "Super-Massive Stars (SMSs)", and the stars with $M \sim 10^2 M_\odot - 10^5 M_\odot$ "Very Massive Stars (VMSs)". Among "VMSs" we define $M > 300 M_\odot$ stars as "Core-Collapse Very Massive Stars (CVMSs)", in order to clarify the distinction between the PISN mass range and the core-collapse range.

1.3 Evolution and explosion of very massive stars and early chemical enrichment of the universe

VMSs are important as a form of Pop III stars. The possibility of the formation of VMSs as Pop III stars has renewed the interest in the final fates of such VMSs. Previous studies have shown that stars in the range of $140M_\odot - 300M_\odot$ undergo pair instability supernovae (PISNe) and disrupt completely, ejecting a large amount of heavy elements (e.g., Barkat et al. 1967; Rakavy & Shaviv 1968; Ober et al. 1983; Bond et al. 1984). If $M > 300M_\odot$, the stars undergo core-collapse to form intermediate mass black holes (IMBHs) ($\sim 5 \times 10^{(2-5)} M_\odot$). Thus PISNe have been suggested to

be the main source of chemical enrichment in the early universe. However, recent detailed comparisons between the observations of extremely metal poor (EMP) stars (Cayrel et al. 2004) and the nucleosynthesis yields of PISN models (Umeda & Nomoto 2002; Heger & Woosley 2002) have shown that the PISN yields are hard to reproduce the abundance patterns of EMP stars (Cayrel et al. 2004).

It is interesting to examine theoretically under what condition the Pop III.1 stars end their lives as PISNe or IMBHs. For this purpose, we adopt the realistic mass accretion rate obtained by Yoshida et al. (2006).

The question of whether CVMSs ($\sim 300M_\odot - 10^5 M_\odot$) actually existed is of great importance, for instance, to understand the origin of IMBHs. Stellar mass black holes ($\sim 10M_\odot$) are formed as the central compact remnants of ordinary massive (25 - $140M_\odot$) stars at the end of their evolution, while supermassive black holes(SMBHs) ($\sim 10^5$ - $10^9 M_\odot$) are now known to exist in the center of almost all galaxies (e.g., Kormendy & Richstone 1995; Bender 2005). IMBHs have not been found until recently. However, there is a strong possibility that some IMBHs have been, indeed, found (Barth et al. 2005). Matsumoto et al. (2001) reported possible identification of a $\gtrsim 700M_\odot$ black hole in M82, by using *Chandra* data. As to formation of SMBHs there are several scenarios (e.g., Rees 2002, 2003). SMBHs may be formed directly from supermassive halos of dark matter (e.g., Marchant & Shapiro 1980; Bromm & Loeb 2003). Ebisuzaki et al. (2001) suggested a scenario where IMBHs grow to a SMBH by merging and swallowing of many of these objects. If CVMSs actually existed, they could be considered as natural progenitors of IMBHs.

1.4 Summary of previous works of Pop III stellar evolution and main goals in our present study

Pop III stellar evolution has been studied by many authors with many approaches. It ranges from proto star formation to main sequence, later nuclear burning stages, collapse, and explosion. Bond et al. (1984); Heger et al. (2001); Ohkubo et al. (2006) calculated the evolution of VMS from main sequence to core collapse or explosion by pair instability. They assumed that such stars have their mass from their starting point of their life and hold their mass through the evolution. A Pop III star has no metal, and so the effect of radiation pressure is negligible (Kudritzki 2000). There is another instability which leads to mass loss, pulsational instability by the ϵ or κ

mechanism. However, the time scale for which such oscillations amplify is longer than the nuclear burning time scale of the main sequence ($\sim 10^6$ years) for Pop III stars, and so a star can evolve while holding most of their initial mass. On the other hand, there are other stellar evolution researches carried out with mass loss even for very low metal massive stars. Meynet et al. (2006), Hirschi (2007), and Hirschi (2008) calculated pre-supernova evolution of very metal poor stars (down to $Z = 10^{-8}$) with rotation and found that such metal poor stars can lose mass with dredge-up – the CNO elements which are synthesized in the deep interior are transported to the surface due to the rotational mixing. They pointed out that this occurs during the latter half of helium burning when the star becomes red super giant (RSG), and nitrogen synthesized by CNO cycle in hydrogen burning shell. However, for metal-free (Pop III) stars, the central helium burning ends before star becomes RSG, so metal-free stars can keep most of their masses at the end of core helium burning even for fast rotating models (Ekström et al. 2006, 2008).

As to the final stages of Pop III stars, Heger & Woosley (2002); Umeda & Nomoto (2002) studied explosion and nucleosynthesis by PISN. Fryer et al. (2001), Nakazato et al. (2006) studied core collapse of rotating $M > 300 M_\odot$ stars which form a black hole. Suwa et al. (2006, 2007) investigated core collapse of VMS with magnetic fields in addition to rotation, and showed the possibility of a jet-like explosion and detection of gravitational wave and neutrino by such stars.

It is very important to examine how such massive stars are formed, i.e., how a proto star obtains such high mass. Research on this theme is performed in the star formation field (Palla, Salpeter, & Stahler 1983; Omukai & Nishi 1998; Omukai & Palla 2003; Yoshida et al. 2006). After a small proto stellar core is formed, the gas surrounding it accretes on the proto star and the stellar mass increases through the pre-main sequence stage. According to the cosmological simulation, mass accretion rate is as high as of the order of $10^{-3} M_\odot \mathrm{yr}^{-1}$, and the stellar mass can reach $\gtrsim 60 M_\odot$ before the star settles into the main sequence. Tan & McKee (2004) calculated star formation by taking into account rotation and disk structure, and concluded that first stars should be much more massive than $30 M_\odot$. If mass accretion continues through its lifetime ($\sim$ a few $\times 10^6$ years), i.e., if mass accretion is not impeded by feedback from the star itself, the final mass can reach several $\times 10^2 M_\odot$ or more. However, there are no studies about how such massive Pop III objects evolve after they start hydrogen burning. We follow the pre-main sequence evolution studied in Omukai &

Palla (2003); Yoshida et al. (2006) and calculate stellar evolution for each nuclear burning stage. Especially for CVMS, the later burning phases after CO core formed (i.e. central helium burning has ended), there are very few calculations that are performed until collapse ($500M_\odot$ and $1000M_\odot$ by Ohkubo et al. 2006, $300M_\odot$ by Heger & Woosley 2002 translated from a $155M_\odot$ helium star). The characteristics of oxygen and silicon burning stages and core collapse phase for CVMS have hardly discussed in detail. It is also one of our main goals that we discuss later evolution.

1.5 This thesis

Pop III stars are formed along with cosmological structure formation. The mass increases by accretion and the final mass may be in the range of VMS ($M \gtrsim 100M_\odot$). We stand on this point, we calculate evolution of Pop III stars with mass accretion from the small mass comparable to the solar mass before main sequence until core collapse or pair instability explosion. Following the introduction in this section, our models are described in chapter 2 and our results are presented in chapter 3. In the last two chapters, 4 and 5, we give discussion and conclusions.

CHAPTER 2
MODELS OF STELLAR EVOLUTION

2.1 Models in Present Studies

In Ohkubo et al. (2006), we calculated evolution, nucleosynthesis, explosion and collapse of Pop III CVMSs starting from the zero-main sequence in the absence of mass accretion. Our current work is based on Ohkubo et al. (2006). More realistically Pop III stars are formed along with cosmological structure formation, and the mass increases by accretion and the final mass may be in the range of VMS ($M \gtrsim 100 M_{\odot}$). Assuming that this is the case, in this paper we calculate the evolution of Pop III stars with mass accretion, starting with small mass comparable to the solar mass before the main sequence, until core collapse or pair instability explosion. In this subsection we summarize our models and assumptions at the initial and each subsequent stage.

We start from a $1.5 M_{\odot}$ star, a typical mass size in the range of low-mass stars. We investigate how this low mass stellar core grows up to a massive one with gas accretion. The starting mass $1.5_{\odot}$ is larger than the initial mass set in (Omukai & Palla 2003), $0.01 M_{\odot}$, by more than two orders of magnitude. However, the time it takes for the star to increase its mass from $0.01 M_{\odot}$ to $1 M_{\odot}$ is in the order of 10^2 years. This is negligible compared with the overall lifetime of a star. Physically, convection over the whole star occurs in the contracting phase. So the starting point little affects the later evolution, and as one can see later, we can qualitatively reproduce the protostellar evolution shown in (Omukai & Palla 2003). We treat Pop III stars, so we set the chemical composition as $X(\mathrm{H}) = 0.753, X(^4\mathrm{He}) = 0.247$. Other minor nuclear species are listed in Table 2.1.

The most important parameter in this work is the mass accretion rate, $\dot{M} = dM/dt$. We change this value and investigate how the star evolves and how large the final mass is. We choose the mass accretion rate in four ways.

(1) Constant value over the whole evolution, changed from $10^{-5} M_{\odot}\,\mathrm{yr}^{-1}$ to $10^{-4}\ M_{\odot}\,\mathrm{yr}^{-1}$. We call this series of models 'C-models'.

(2) The mass accretion rate calculated with three dimensional cosmological simulations by Yoshida et al. (2006). These authors calculated cosmological structure formation in a ΛCDM universe and evaluated the accretion rate for the first generation stars, which is called 'Pop III.1 stars'.

Table 2.1. Initial chemical composition for a Pop III star. Other species which are not listed here are zero.

Nuclear Spieces	Mass Fraction
p	7.53E-01
d	2.00E-05
^{3}He	2.00E-05
^{4}He	2.47E-01
^{7}Li	2.00E-10

We adopt $\dot{M}$ by Yoshida et al. (2006) and it is written as a function of stellar mass M:

$$\frac{dM}{dt} = \begin{cases} 0.0450 \times M^{-2/3}\, M_\odot\, \mathrm{yr}^{-1} & M < 300 M_\odot \\ 16.3 \times M^{-1.7}\, M_\odot\, \mathrm{yr}^{-1} & M > 300 M_\odot. \end{cases} \tag{2.1}$$

We mark this accretion rate with a subscript 'Y', as dM_Y/dt. We also adopt models with accretion rates smaller than dM_Y/dt by a factor of 2, 3, 10, and 20. We call these models 'Y-series'.

(3) The accretion rate calculated in Yoshida et al. (2007). The secondly formed stars (second generation stars), which has no metal but formation of these second generation stars are affected by first generation stars (Pop III.1 stars). For such stars, cooling mechanism and the gaseous mass is totally different from that of PopIII.1 stars.

Pop III.1 stars radiates a large amount of UV photons around them, and build up HII regions with as large as a few kiloparsec diameter (Yoshida et al. 2007). This environment promotes the formation of HD molecules, which can cool the gas down to as low as $40 - 50$ K. In a gas cloud at such low temperatures (note still warmer than the present-day molecular gas clouds), typical formed stellar mass is $\sim 40 M_\odot$, smaller than Pop III stars. Stars formed in such environment are called 'Pop III.2' stars (McKee & Tan 2008; Johnson et al. 2008). Accretion rate are as follows:

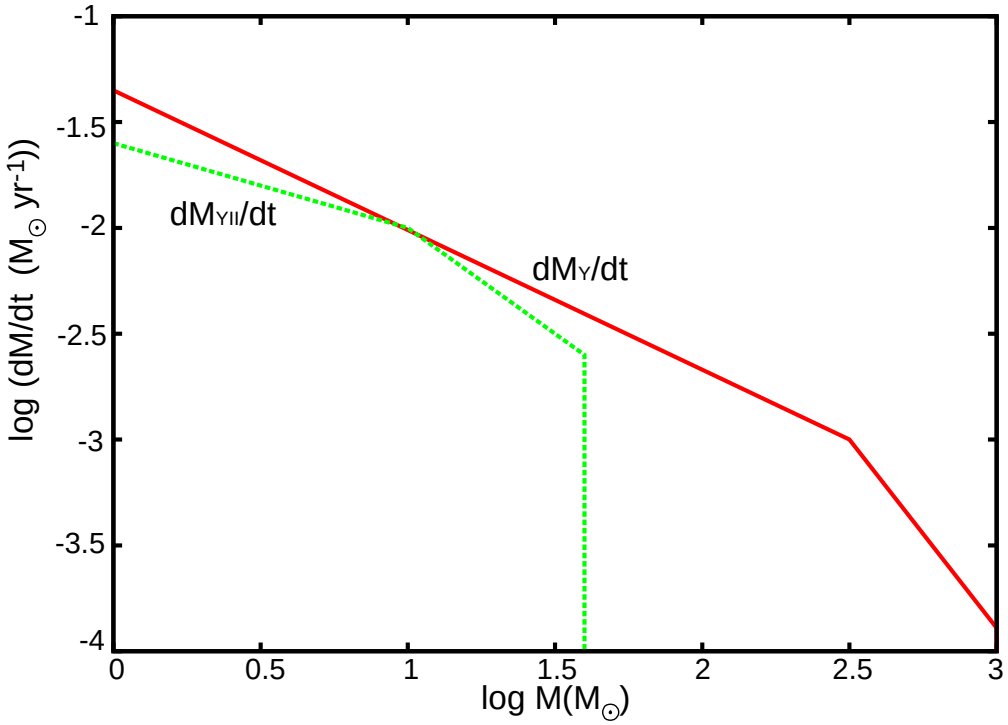

Figure 2.1 Mass accretion rate for first generation stars as a function of stellar mass calculated with cosmological simulations by Yoshida et al. (2006).

$$\frac{dM}{dt} = \begin{cases} 0.0250 \times M^{-0.4}\, M_\odot\, \mathrm{yr}^{-1} & M \leq 10 M_\odot \\ 0.10 \times M^{-1.0}\, M_\odot\, \mathrm{yr}^{-1} & 10 M_\odot < M < 40 M_\odot \\ 0 & M \geq 40 M_\odot. \end{cases} \tag{2.2}$$

We call this model 'YII', and $\dot{M}$ is labeled 'dM_{YII}/dt'. we distinguish this model from 'Y-series'. For this model, accretion rate is much lower than dM_Y/dt, because HII region created by radiation from first generation stars makes accretion rate lower, and gaseous mass is much smaller, only $40 M_\odot$. Accretion late for (2) and (3) is shown in the upper panel in Figure 2.1.

(4) Mass accretion rates by McKee & Tan (2008), who take interruption by feedback into consideration. They parametrized a measure of entropy of the accreting gas, and subsequent accretion rate varies by more than one order of magnitude by changing this parameter. In this paper, we adopt typical three accretion rates. We express $\dot{M}$ by reading and simplifying them from figure 9 in McKee & Tan (2008) as follows

$$\frac{dM_{\rm M1}}{dt} = \begin{cases} 0.125 \times M^{-0.44}\, M_\odot\, {\rm yr}^{-1} & M \leq 81 M_\odot \\ 178 \times M^{-2.1}\, M_\odot\, {\rm yr}^{-1} & 81 M_\odot < M < 321 M_\odot \\ 0 & M \geq 321 M_\odot \end{cases} \tag{2.3}$$

,

$$\frac{dM_{\rm M2}}{dt} = \begin{cases} 0.0250 \times M^{-0.44}\, M_\odot\, {\rm yr}^{-1} & M \leq 41 M_\odot \\ 20.0 \times M^{-2.3}\, M_\odot\, {\rm yr}^{-1} & 41 M_\odot < M < 135 M_\odot \\ 0 & M \geq 135 M_\odot \end{cases} \tag{2.4}$$

, and

$$\frac{dM_{\rm M3}}{dt} = \begin{cases} 0.005 \times M^{-0.44}\, M_\odot\, {\rm yr}^{-1} & M \leq 25 M_\odot \\ 32 \times M^{-3.2}\, M_\odot\, {\rm yr}^{-1} & 25 M_\odot < M < 57 M_\odot \\ 0 & M \geq 57 M_\odot. \end{cases} \tag{2.5}$$

These are marked 'M', as $dM_{\rm Mi}/dt$ $(i = 1, 2, 3)$. We call these models 'M-series'. These accretion rates are shown in Figure 2.2.

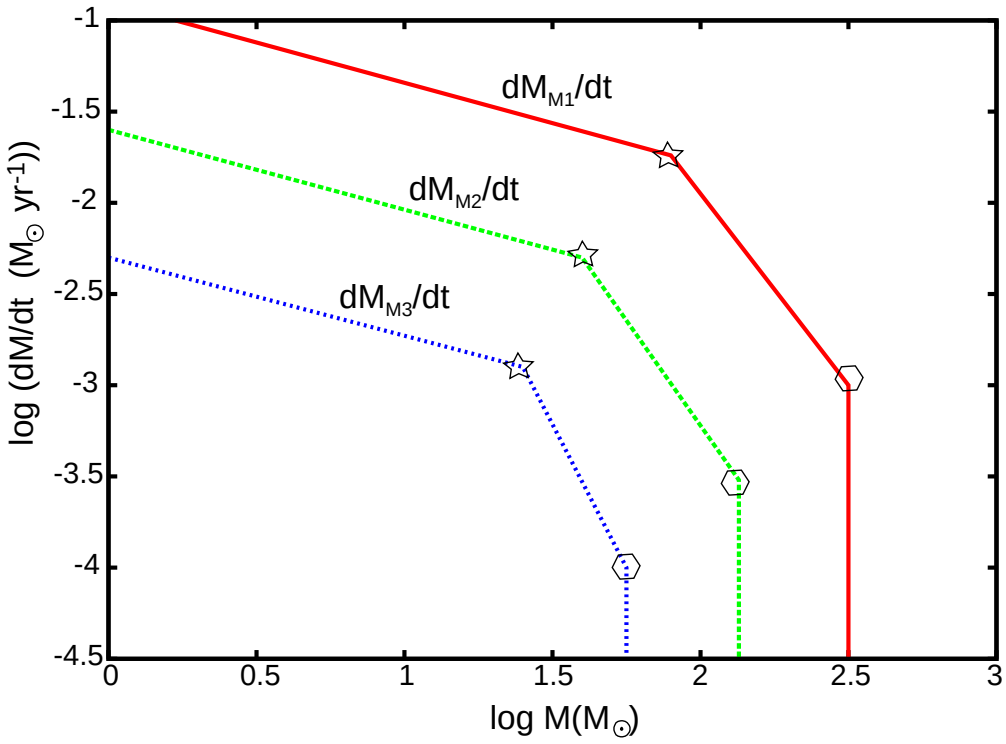

Figure 2.2 Mass accretion rate for first generation stars as a function of stellar mass by McKee & Tan (2008).

Table 2.2. Stellar evolution models with constant mass accretion rate.

Models	Mass accretion rate($M_\odot\,\mathrm{yr}^{-1}$)
C-1	1.00E-05
C-2	3.00E-05
C-3	1.00E-04

Table 2.3. Stellar evolution models with mass accretion rates as a function of stellar mass. The mass accretion rates $dM_{\rm Y}/dt$ and $dM_{\rm YII}/dt$ are illustrated in Figure 2.1. The mass accretion rates $dM_{\rm Mi}/dt$ are displayed in Figure 2.2.

Models	Mass accretion rate($M_\odot\,\mathrm{yr}^{-1}$)
Y-1	$dM_{\rm Y}/dt$
Y-2	$0.5 \times dM_{\rm Y}/dt$
Y-3	$0.33 \times dM_{\rm Y}/dt$
Y-4	$0.1 \times dM_{\rm Y}/dt$
Y-5	$0.05 \times dM_{\rm Y}/dt$
YII	$dM_{\rm YII}/dt$
M-1	$dM_{\rm M1}/dt$
M-2	$dM_{\rm M2}/dt$
M-3	$dM_{\rm M3}/dt$

In Table 2.2 and Table 2.3, the models we calculate are summarized. In summary, (1) 'C-series' is stars with constant $M_\odot$, no feedback. (2) 'Y-series' is PopIII.1 stars with time-dependent $M_\odot$, no feedback. (3) 'YII' is PopIII.2 stars with time-dependent $M_\odot$, limited gaseous material. (4) 'M-series' is stars with time-dependent $M_\odot$, with feedback.

2.2 Physical inputs and mathematical equations

To calculate presupernova evolution we adopt the stellar evolution code constructed by Umeda & Nomoto (2002, 2005) based on the Henyey method. This code is developed from the codes constructed by Nomoto & Hashimoto (1988), and Umeda et

al. (1999). In the following sections, we summarize physical inputs and basic mathematical equations to simulate. The detailed numerical procedure is described in Appendix.

2.2.1 Basic equations of stellar structure

Structure and evolution of a spherically symmetric star are described mathematically as the following differential equations:

$$\frac{dr}{dq} = \frac{M}{4\pi r^2 \rho} \tag{2.6}$$

$$\frac{dP}{dq} = -\frac{GM^2 q}{4\pi r^4} - \frac{M}{4\pi r^2}\frac{\partial^2 r}{\partial t^2} \tag{2.7}$$

$$\frac{dT}{dq} = -\frac{GM^2 qT}{4\pi r^4 P}\nabla \tag{2.8}$$

$$\frac{dl}{dq} = \varepsilon_{\rm n} - \varepsilon_{\nu} + \varepsilon_{\rm g} \tag{2.9}$$

.

We adopt mass coordinate q normalized by total stellar mass M, that is, $q = m/M$ in our code. P is pressure, T is temperature, t is time, G is the newtonian gravitational constant. Equation 2.7 describes equation of motion, i.e. difference of pressure gradient and gravity formulates acceleration. In the situation where one can assume hydrostatic equilibrium, the inertia term can be dropped. However, dynamically stars over $140 M_{\odot}$ enter the pair instability region when the central temperature reaches around 10^9 K where the oxygen burning starts. In this situation the hydrostatic equilibrium does not hold any longer. Dynamical instability also occurs by Fe decomposition. All stars whose central temperature reach $\log T$ (K) $\sim$ 9.7 meet this situation. We drop the hydrostatic equilibrium and take acceleration into consideration. Equation 2.8 describes energy transport. $\nabla = d\ln T/d\ln P = \min(\nabla_{\rm rad}, \nabla_{\rm ad})$,

written as:

$$\nabla_{\rm rad} = \frac{3}{16\pi acG}\frac{\kappa l P}{m T^4}, \quad \nabla_{\rm ad} = \frac{d\ln T}{d\ln P}_{\rm ad} \tag{2.10}$$

where $a = 7.56 \times 10^{-15}{\rm ergcm^{-3}K^{-4}}$ is the radiation energy density constant, $c =$ is the light speed, and κ is a radiative cross section per unit mass averaged over frequency. Equation 2.9 is energy equation. $\varepsilon_{\rm n}$ means energy generation by nuclear reaction per unit volume, ε_ν is energy loss via neutrinos, and $\varepsilon_{\rm g}$ is gravitational energy release, written as the entropy change as

$$\varepsilon_{\rm g} = -T\left(\frac{\partial s}{\partial t}\right)_{\rm M_r} \tag{2.11}$$

Chemical composition in stellar interior changes with time by nuclear reactions. The change of nuclear species i is described as:

$$\begin{aligned} \frac{dX_i}{dt} &= \frac{\partial X_i}{\partial t} - \frac{\partial}{\partial M_r}(D\frac{\partial X_i}{\partial M_r}), \\ \frac{\partial X_i}{\partial t} &= \sum_j c_i(j)\lambda_j X_j + \sum_{j,k} c_i(j,k)\rho N_A\langle jk\rangle X_j\mu_k X_k + \sum_{j,k,l} c_i(j,k,l)\rho^2 {N_A}^2\langle jkl\rangle X_j\mu_k X_k\mu_l X_l, \\ i &= 1, ..., I \end{aligned} \tag{2.12}$$

where X_i is the nuclear mass fraction, D diffusion coefficient of convective mixing by Spruit (1992):

$$D = \max(0,\ \nabla_{\rm rad} - \nabla_{\rm ad}) f_k K_t (4\pi r^2\rho)^2 (\frac{4}{\beta} - 3)/\nabla_\mu. \tag{2.13}$$

N_A Avogadro's number, and ρ the density, respectively. In the right hand side, the first term denotes weak interaction and photodisintegration. λ is the rate of these phenomena. β is the ratio of gas pressure to total pressure, ∇_μ is mean molecular weight gradient as a function of pressure in log scale:

$$\nabla_\mu = \frac{d\ln\mu}{d\ln p}. \tag{2.14}$$

K_t is the thermal diffusivity:

$$K_t = \frac{4acT^3}{3\kappa\rho^2 c_P}. \tag{2.15}$$

f_k is the parameter as to the thermal diffusivity, and is set to 0.3 in this research, same in Umeda & Nomoto (2002, 2005).

The second and third terms in Equation 2.13 describe two-body and three-body reactions, respectively. $\langle jk \rangle$ and $\langle jkl \rangle$ are the thermally averaged cross section times relative velocity for the reactions. The coefficient c_i are:

$$c_i = \pm N_i \tag{2.16}$$

$$c_i(j,k) = \pm \frac{N_i}{N_j! N_k!} \tag{2.17}$$

$$c_i(j,k,l) = \pm \frac{N_i}{N_j! N_k! N_l!}. \tag{2.18}$$

The sign + is adopted when the nuclear species i are created and $-$ is adopted otherwise.

The nuclear reaction network for calculating nucleosynthesis and energy generation at each stage of the evolution is developed by Hix & Thielemann (1996). We include 51 isotopes up to Si until He burning ends, and 240 up to Ge afterwards. The nuclear species included in this network is listed in Table 2.4. When the temperature reaches 5×10^9 K, where "nuclear statistical equilibrium" (NSE hereafter) is realized, the abundance of each isotope is determined for a given set of density, temperature, and $Y_{\rm e}$. Here $Y_{\rm e}$ is the number of electrons per nucleon, defined as:

$$Y_{\rm e} = \sum_i \frac{Z_i}{A_i} X_i. \tag{2.19}$$

where Z_i is the atomic number, A_i is the mass number, and X_i is the mass fraction of species i. $Y_{\rm e}$, as well as density and temperature, is a key quantity to determine the abundance of each element. We assume NSE at $\log T$ (K) ≥ 9.75.

Table 2.4. Nuclear species included in the network for the stellar evolution.

Elements	Mass number	Elements	Mass number	Elements	Mass number
n	1	Al	22 - 27	Co	51 - 61
H	1 - 2	Si	26 - 32	Ni	54 - 65
He	3, 4	P	27 - 34	Cu	56 - 66
Li	6, 7	S	30 - 36	Zn	62 - 70
Be	7, 9	Cl	33 - 37	Ga	67 - 72
B	8, 10, 11	Ar	34 - 40	Ge	68 - 74, 76
C	11 - 13	K	37 - 41	As	75
N	12 - 15	Ca	38 - 48	Se	74, 76 - 78, 80, 82
O	14 - 18	Sc	40 - 47	Br	79, 81
F	17 - 19	Ti	42 - 51	Kr	78, 80, 82 - 84, 86
Ne	18 - 22	V	44 - 53	Rb	85, 87
Na	21 - 23	Cr	46 - 55	Sr	84, 86 - 88
Mg	18 - 22	Mn	48 - 57	Y	89

2.2.2 Effect of mass accretion

The mass coordinate of each mesh is kept constant if the stellar mass does not change, as we did for stars calculated in Ohkubo et al. (2006). However, here we treat stars which grow by mass accretion. Therefore, as the stellar mass increases, it is convenient to use q as an independent variable (Sugimoto & Nomoto 1975). That is why we choose q instead of M_r.

While gas continues to accrete, a part of it is fed into the star and the rest is accumulated on the stellar surface. Such mass flux releases gravitational energy and contributes to the term $\varepsilon_{\rm g}$ Equation 2.9 (see also Equation 2.11. $\varepsilon_{\rm g}$ can be divided into two terms (Neo et al. 1976; Nomoto 1982):

$$\varepsilon_{\rm g} = -T\left(\frac{\partial s}{\partial t}\right)_{\rm M_r} = \varepsilon_{\rm g}^{\rm (h)} + \varepsilon_{\rm g}^{\rm (nh)}, \tag{2.20}$$

where

$$\varepsilon_{\rm g}^{\rm (h)} = T\frac{d\ln M}{dt}\left(\frac{\partial s}{\partial \ln q}\right)_t, \tag{2.21}$$

and

$$\varepsilon_{\rm g}^{\rm (nh)} = -T\left(\frac{\partial s}{\partial t}\right)_q. \tag{2.22}$$

Here mathematically differential procedure is transformed as follows

$$\left(\frac{d}{dt}\right)_{\rm M_r} = \left(\frac{\partial}{\partial t}\right)_{\rm q} - \left(\frac{d\ln M}{dt}\right)\left(\frac{\partial}{\partial \ln q}\right)_t. \tag{2.23}$$

The inflowing matter also releases gravitational energy before reaching the stellar surface and converts it to thermal energy, which is radiated away as X-rays or UV radiation. This is accretion luminosity, $L_{\rm acc}$

$$L_{\rm acc} = \frac{GM}{R}\frac{dM}{dt}. \tag{2.24}$$

The total radiative luminosity L is calculated as $L = L_{\rm acc} + L_{\rm g} + L_{\rm n}$ where $L_{\rm g}$ and $L_{\rm n}$ is integration of $\varepsilon_{\rm g}$ described above and nuclear energy generation rate $\varepsilon_{\rm n}$, respectively:

$$L_{\rm g} = \int_0^M \varepsilon_{\rm g} dM_r, \tag{2.25}$$

and

$$L_{\rm n} = \int_0^M \varepsilon_{\rm n} dM_r. \tag{2.26}$$

In the rapid inflow case, the stellar radius increases, then $L_{\rm acc}$ decreases, and radiated away into the space. Therefore, we do not include $L_{\rm acc}$ in L as calculating stellar luminosity.

We initially set about 400 meshes to calculate interior structure ($m \leq m_{\rm F}$ where $m_{\rm F}$ indicates the fitting point mass; see Appendix) at the start of the calculation. We treat meshes in two ways to do so. In the outer area, the mass coordinates change as the stellar mass increases so that the mass coordinates m normalized to the stellar mass M ($q = m/M$) are constant. In the inner area, the mass coordinates are constant as in the case without mass accretion. The boundary of two areas can be chosen at any point. The boundary meshnumber is '$j_{\rm lag}$' in the code. In other

words, $m(j)$ is constant for $j < j_{\rm lag}$, and $q(j)$ is constant for $j \geq j_{\rm lag}$. The interval between $m(j_{\rm lag}-1)$ and $m(j_{\rm lag})$ becomes as stellar mass increases, so we insert new meshes properly. $j_{\rm lag}$ can be changed freely, and we move $j_{\rm lag}$ outward as the star evolves, because the mass accretion rate drops or the timestep becomes shorter and it is not necessary to move the mass coordinate outward for so many meshes.

2.3 Final mass evaluation

We can follow mass increase for each mass accretion rate by integrating them with regard to time before calculating actual stellar evolution:

$$M(t) = \int_0^t \frac{dM}{dt} dt. \tag{2.27}$$

For constant mass accretion rate models 'C-series', this is simple; mass accretion rate multiplied by time. Stellar mass increases in proportion to time. After 2 million years, stellar mass reaches $20M_\odot$ for the model C-1, $60M_\odot$ for C-2, and $200M_\odot$ for C-3, respectively. After 5 million years, stellar mass reaches $50M_\odot$ for the model C-1, $150M_\odot$ for C-2, and $500M_\odot$ for C-3, respectively. We show stellar mass increase in Figure 2.3 for changing mass accretion rate models 'Y-series', YII, and 'M-series'. It is likely to reach the VMS mass range ($M \gtrsim 100M_\odot$) even for low mass accretion rate cases among our models for Y-series. On the contrary, for models YII and 'M-series', it is suggested that mass accretion stops in 10^5 years, well before the star ends its life. The lifetime of VMSs is at least 2×10^6 years (the pre-main sequence stage is $\sim 10^5$ years, short for the main sequence phase). Of course the exact stellar lifetime should be determined by actual calculations. Especially for 'Y-series', a slight change of lifetime, i.e. the time it takes for hydrogen and helium burning makes difference if a star ends its life as a PISN or core-collapse to form a black hole. It is possible that the lifetime changes between the models with and without mass accretion even if the final mass is the same. We examine and compare the lifetime in the results.

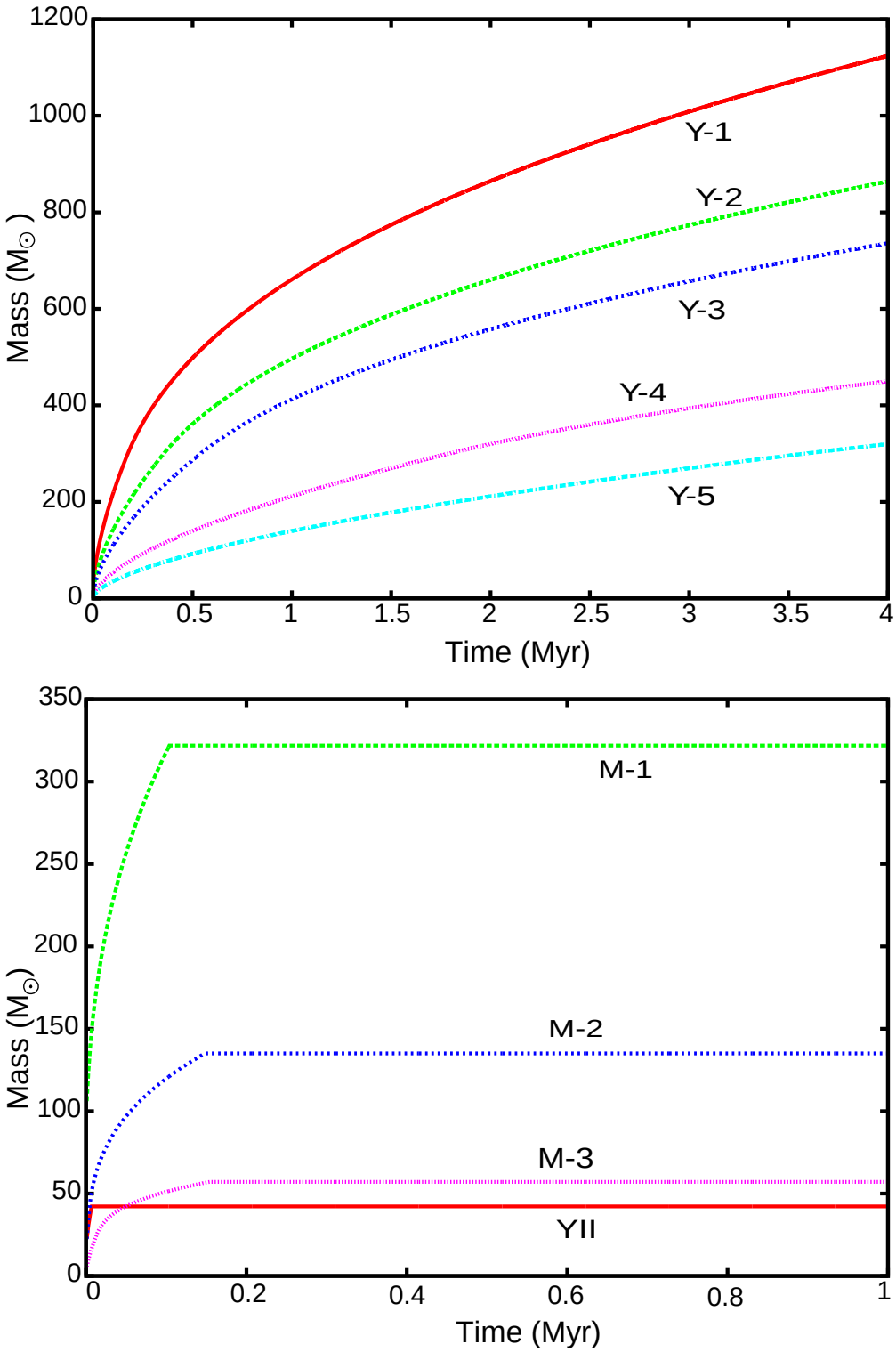

Figure 2.3 Mass increase with time obtained by integrating mass accretion rate by equation 2.27. Upper panel: for 'Y-series'. Under panel: for models YII and 'M-series'.

CHAPTER 3
EVOLUTION OF VERY-MASSIVE STARS WITH ACCRETION

3.1 Overview

We carried out stellar evolution of very-massive stars with or without accretion. The evolution is divided into several stages: pre-main sequence, main sequence (hydrogen burning), helium burning, later burning stages (carbon, neon ,oxygen, silicon burning), and the final stage (core-collapse or explosion as a PISN). We describe results for each stage in detail in each section. In this section, we summarize overall characteristics through the evolution.

3.1.1 Mass increase through evolution

Figure 3.1 shows for each model stellar mass radius relation through evolution. Similar relation is shown in figure 1 of Omukai & Palla (2003) and figure 13 of Yoshida et al. (2006). Our Y-1 model uses the same mass accretion rates as those in Yoshida et al. (2006), although their calculation ends at the end of the proto-stellar phase. Examining Figure 3.1, one can clearly see a few distinct evolution phases - proto-stellar phase, main sequence (hydrogen burning) phase, and later phase. Each phase is partitioned with marks in the figure. Stellar radius reaches to as large as $\sim 10^2 R_\odot$ just after calculation started except for 'C-series'. At this point mass accretion rate is of the order of $10^{-2} M_\odot \mathrm{yr}^{-1}$. In more realistic calculations Omukai & Palla (2003) and Yoshida et al. (2006) started their simulation of proto-stellar evolution with mass accretion with the very first core mass of $\sim 10^{-3} M_\odot$ (comparable to Jupiter mass). After rapid expansion the star settles into the portion where radius increase only gradually while adjusting to the mass accretion rate (see also Figure 3 in Neo et al. 1976). For models C-2 and C-3 considerable expansion occurs, but accretion rate is lower than that of 'Y-series' or 'M-series', so stellar radius is moderate. For model C-1, the star shows a slight radius increase at the very first stage, but after that the star contracts toward the main sequence phase because mass accretion rate is too low. At this stage the stellar radius is proportional to the stellar mass and mass accretion rate as:

$$R \propto M^{0.27}\dot{M}^{0.41} \tag{3.1}$$

(Stahler et al. 1986; Omukai & Palla 2003). Our results exhibit the same trend in the subsequent evolution as in Omukai & Palla (2003) and Yoshida et al. (2006). What is more, the time it takes for the star to grow from $10^{-3}M_{\odot}$ to $1.5M_{\odot}$ is negligible compared with that in later phases, and this initial stage does not affect at all such discussions as how massive the star can grow. Therefore, our starting calculations at $1.5M_{\odot}$ is justified.

After this stage of the protostar phase, the evolution depends on the timescales of accretion, $\tau_{\rm acc} = M/\dot{M}$, relative to that of Kelvin-Helmholz (KH) contraction, $\tau_{\rm KH}$, as shown in Figure 3.2.

(1) During the phase which the stage with the filled square in Figure 3.1 and Figure 3.2, $\tau_{\rm acc} \sim \tau_{\rm KH}$, so that the radiative energy loss (L) is supplied by the gravitational energy release due to mass accretion. The star does not contract, i.e., the radius stays almost constant (Figure 3.1).

(2) During the phase between the filled square and the star mark in Figure 3.1 and Figure 3.2, the accretion gets closer than the radiative energy loss, i.e., $\tau_{\rm acc} > \tau_{\rm KH}$. Thus the K-H contraction release the gravitational energy to supply the radiative luminosity at enough rate. As a result, the star contracts as seen in the decrease in the radius (Figure 3.1).

During these stages our results reproduced a similar trend found in Yoshida et al. (2006). For 'C-series', the star expands to some extent and turns to KH contraction quickly because of relatively low mass accretion rate. We describe these stages in detail in section 3.2.

In the stellar interior temperature rises during KH contraction and the central temperature reaches 10^8 K. The star settles into the main sequence phase, i.e., nuclear energy generation supplies stellar luminosity. This is approximately the turning point in the stellar radius after KH contraction (see Figure 3.1. The starting point of the main sequence is marked as the filled stars in Figure 3.1). The time it takes to reach the main sequence is about 10^5 years, and the stellar mass reaches several $10 - 100M_{\odot}$ at that time already in a massive star range. This rapid mass increase means that most Pop III.1 stars are very massive, $M \gtrsim 100M_{\odot}$. For 'Y-series', mass accretion continues through evolution. For 'M-series', mass accretion stops during

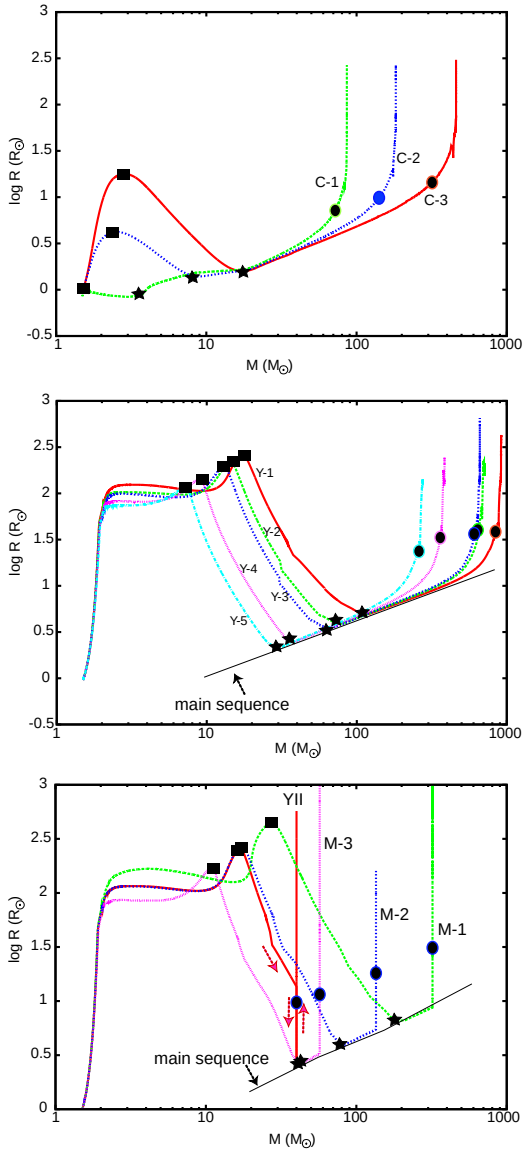

Figure 3.1 Mass radius relations for each model star evolving with mass accretion. The filled circles on the lines show the end of main sequence (hydrogen exhaustion at the center). Top panel: for 'C-series' (constant mass accretion rates). middle panel: for 'Y-series' (mass accretion rates based on cosmological simulation; Yoshida et al. 2006). bottom panel: for models YII and 'M-series' (mass accretion rated based on Yoshida et al. 2007 for YII, and McKee & Tan 2008 for 'M-series', respectively).

main sequence phase. These models (Pop III.1 stars) are very massive. Model YII (Pop III.2 star) is the only case in which accretion stops during the KH contraction

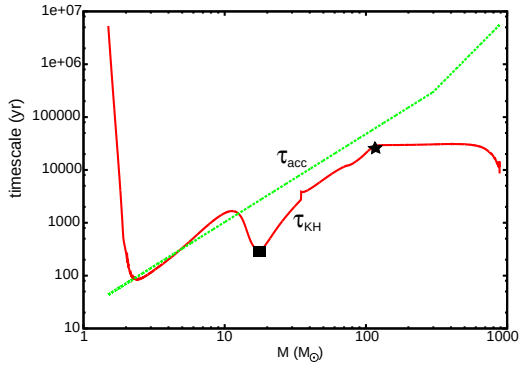

Figure 3.2 The timescales of accretion, $\tau_{\rm acc} = M/\dot{M}$, and Kelvin-Helmholz (KH) contraction, $\tau_{\rm KH}$ for model Y-1.

phase because we assume that there are limited gas material (typically $40M_{\odot}$) for Pop III.2 star formation. In this cause stellar mass is in the range of ordinary massive stars ($20M_{\odot} \lesssim M \lesssim 60M_{\odot}$).

Pop III massive stars keep the central temperature as high as $\sim 10^8$K through the main sequence. The stellar luminosity is of the order of $\sim 10^6 - 10^7 L_{\odot}$. The main source of nuclear energy generation is CNO cycle, and such high temperature is necessary to continue to supply enough energy to support the high luminosity.

We assume that mass accretion continues through the evolution for 'Y-series'. For 'M-series' accretion stops during main sequence (for YII model accretion stops before main sequence). After accretion stops, the star evolves vertically in Figure 3.1. While mass accretion continues, the star adjusts itself to the same condition of main sequence with corresponding mass with increasing mass (along the main sequence line in Figure 3.1). Therefore the stellar radius increases with mass. The main sequence phase is the longest in the stellar life. A star spends about 90 % of its life at this phase. Therefore the final mass is roughly determined by how much mass accretes through the main sequence. The filled circles in Figure 3.1 show the end of the main sequence (hydrogen exhaustion at the center). The star grows up to be very-massive. The details are summarized in section 3.1.2.

After central hydrogen burning, central helium burning follows. This lasts for about one tenth of the time it takes for hydrogen burning. The star expands and the stellar radius becomes more than 10 times larger at the end of helium burning than that in the main sequence due to a kind of instability called 'κ-mechanism' (Baraffe

et al. 2001).

Figure 3.3 shows the evolution of each model on the HR diagram. These figures correspond to figure 8 in Omukai & Palla (2003). First the stellar radius is large and surface effective temperature is low ($\sim$ 6000K). This is due to strong sensitivity of the H^- bound-free opacity on temperature, the main source of opacity around this temperature. This corresponds to the adiabatic mass accretion stage (see Figure 3.1). After this stage, the effective temperature shifts toward higher regions and reaches near 10^5K. The main opacity source changes from H^- bound-free absorption to electron scattering at such high temperatures. During the shift stellar radius decreases, and this corresponds to the KH contraction.

The star reaches main sequence, and that point on the HR diagram is roughly identical to that of a $Z = 0$ star with no accretion. After reaching main sequence, the star evolves on the main sequence line at each mass with increasing mass. For model C-1, mass accretion rate is too low and the star evolves on the main sequence line from the very early phase. As hydrogen is consumed, the star leaves the main sequence point and the effective temperature starts to decrease. At the end of hydrogen burning, the stellar mass reaches near its final mass. Near the end of helium burning, stellar radius increases and effective temperature decreases.

Figure 3.4 shows mass luminosity relation for each model. For comparison, the main sequence points of several stars with no mass accretion are also shown. One can match the mass of each point on HR diagram by comparing this figure and Figure 3.3. After reaching main sequence, the stars evolve along the main sequence lines of corresponding stars with no mass accretion.

For later phases (carbon, neon, oxygen, silicon burning and iron core-collapse or explosion by pair instability) one can obtain no information from Figure 3.1 - 3.4. We sketch each nuclear burning stage.

Figure 3.5 shows the evolutionary tracks of the central density and central temperature relation. For 'Y-series', only two (Y-1, which ends up as a core-collapse, and Y-5, which ends up as a PISN) of five models are plotted to refrain from making the graph too crowded. In bottom panel, models YII and 'M-2' are shown. These figures are convenient to see the later phase after helium burning (carbon, neon, oxygen, and silicon burning). We also plot $25M_\odot$ (from Umeda & Nomoto 2002) and $1000M_\odot$ (from Ohkubo et al. 2006) stars with no mass accretion for comparison. Generally speaking, more massive stars have higher entropies (lower densities) at the same tem-

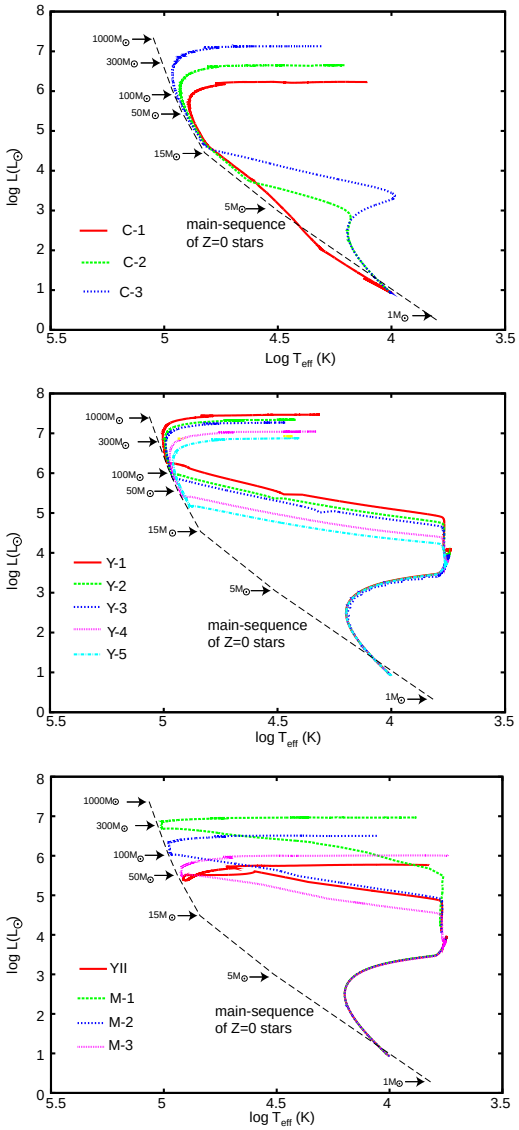

Figure 3.3 The evolution of stars on the HR diagram with mass accretion. The long dashed line shows the location of main sequence stars with $Z = 0$. We adopt the location for $M \leq 100 M_{\odot}$ stars from Marigo et al. (2001), and for $M \geq 100 M_{\odot}$ stars from Ohkubo et al. (2006). Top panel: for 'C-series'. Middle panel: for 'Y-series'. Bottom panel: for models YII and 'M-series'.

peratures. For the models with mass accretion, the density-temperature location shifts toward the lower side with mass increase through hydrogen burning, while the central temperature is kept at $\sim 1 \times 10^8$K. After helium burning ($\log T_c \sim 8.5$), the star with mass accretion evolves parallel to stars with no mass accretion. After

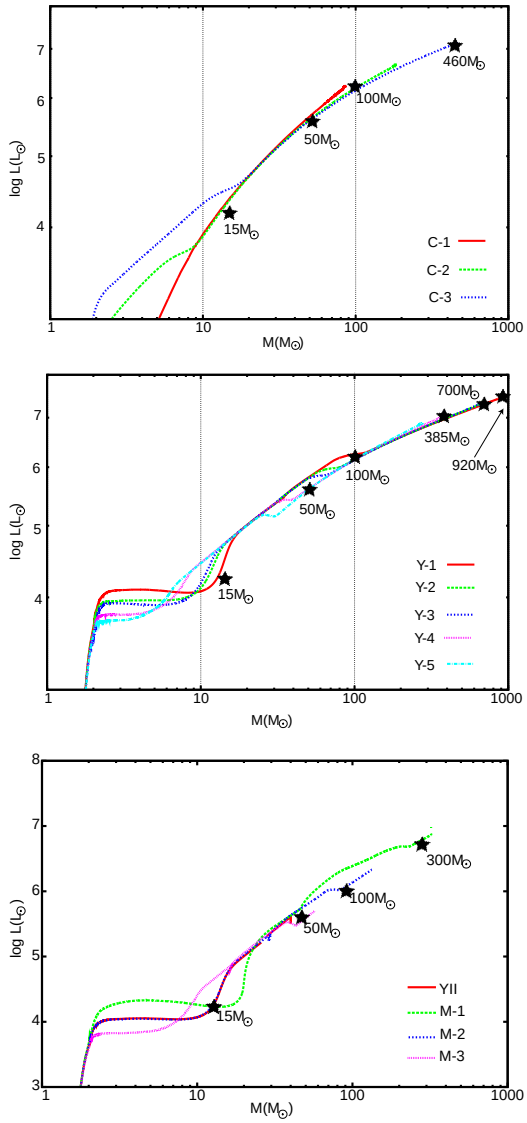

Figure 3.4 Mass luminosity relations for each model star evolving with mass accretion. The filled star marks and the attached numbers on the graph show the point at main sequence of stars with no mass accretion. 15, 50, and $100 M_{\odot}$ from Marigo et al. (2001). 385, 460, 700, and $920 M_{\odot}$ from this research (N-3, N-4, N-5, N-6, respectively). Top panel: for 'C-series'. Middle panel: for 'Y-series'. Bottom panel: for models YII and 'M-series'.

helium burning, the evolving time scale ($\lesssim 10^4$ years from central helium exhaustion to core-collapse or explosion as a PISN and $\lesssim 1$ year after T_c reaches 10^9K) is much shorter than accreting timescale ($\tau_{\rm acc} = M/\dot{M}$). Therefore, the core evolves indepen-

dently from the outer envelope. The change in the outer parts does not affect the core structure and evolution.

The models Y-5 and C-2 end as a PSIN because they enter the pair-instability region (at log $T_c \sim 9$) The central region collapses, which induces thermonuclear runaway of oxygen and silicon burning due to the rapid temperature increase. The thermal pressure generating by the runaway nuclear burning stops the core contraction, expands and explodes the star (Rakavy et al. 1967; Ober et al. 1983; Bond et al. 1984; Glatzel et al. 1985; Woosley 1986). This appears as the turning point of evolutionary tracks on the graph.

The models Y-1, Y-2, Y-3, Y-4, M-1, and C-3 also enter the pair-instability region. However, they do not explode as a PISN, form an iron core, and then cause core-collapse to become a black hole. These very massive stars have large gravitational binding energy. The energy released by the nuclear processes can not exceed this binding energy of the star.

The final masses of model YII ($40M_\odot$) and model M-3 ($57M_\odot$) are in the range of ordinary massive stars ($M \lesssim 60M_\odot$), and so the evolutionary track is similar to that of $25M_\odot$ in the top panel. It ends as core-collapse and forms a black hole. Model M-2, whose final mass is $137M_\odot$, causes pair instability pulsations by central oxygen and silicon burnings. In stars with mass $80M_\odot \lesssim M \lesssim 140M_\odot$, slightly under the PISN mass range, this typical phenomenon appears (Umeda & Nomoto 2008; Woosley et al. 2007). The energy released at this stage is not enough to explode the whole star in this mass range, it falls back, and central temperature and density rise again. The star finally collapses to form a black hole after several oscillations.

3.1.2 Stellar lifetime, final mass, and final fate

In section 2.3, a simple estimate of final mass for each mass accretion rate model is described. Here we describe stellar lifetime, final mass, and final fate, i.e., whether the star finally ends its life with core collapse to form a black hole or a PISN. In Table 3.1 these results are summarized.

Firstly, we discuss 'C-series' and 'Y-series' models, for which mass accretion continues through the evolution. In such situation, final mass is determined by the actual stellar lifetime. For models C-3, Y-1, Y-2, Y-3, and Y-4, the final mass reaches over $300M_\odot$ and they end their life with iron core-collapse, whereas the final mass of model

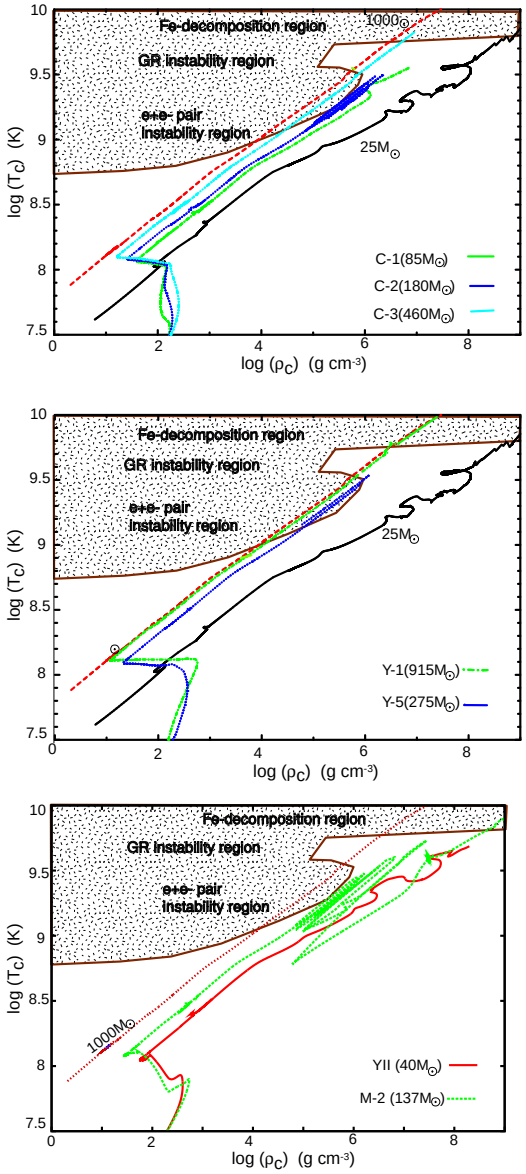

Figure 3.5 Evolutionary tracks of central temperature and central density of stars with each model. For comparison, tracks of $25M_{\odot}$ (from Umeda & Nomoto 2002) and $1000M_{\odot}$ (from Ohkubo et al. 2006) are also plotted. Top panel: for 'C-series'. Middle panel: for 'Y-series'. Bottom panel: for models YII and 'M-series'.

C-2 is $180M_{\odot}$ and that of model Y-5 is $275M_{\odot}$, respectively, and they end their life as a PISN. For model C-1 the final mass is $85M_{\odot}$. This star forms an iron core and collapses to form a black hole, but this star does not go through the pair instability

Table 3.1. Stellar lifetime, final mass, and final fate for each model.

Models	lifetime (yr)	final mass ($M_\odot$)	final fate
C-1	8.5×10^6	85	Core-Collpase
C-2	6.0×10^6	180	PISN
C-3	4.6×10^6	460	Core-Collapse
Y-1	2.3×10^6	915	Core-Collpase
Y-2	2.4×10^6	710	Core-Collpase
Y-3	2.5×10^6	610	Core-Collpase
Y-4	2.9×10^6	385	Core-Collpase
Y-5	3.1×10^6	275	PISN
YII	5.5×10^6	40	Core-Collpase
M-1	2.2×10^6	321	Core-Collpase
M-2	3.1×10^6	137	Core-Collpase
M-3	4.5×10^6	57	Core-Collpase

region. One notable point is that generally final mass reaches rather high even for very low mass accretion rate cases. For constant mass accretion rate models ('C-series'), mass accretion rates are much lower than those in Omukai & Palla (2003), in the order of $10^{-3} M_\odot\,\mathrm{yr}^{-1}$. They concluded that the final mass can reach $\gtrsim 400 M_\odot$ with such high rates. Our results, however, show a star can grow to the VMS range in mass scale with rather low mass accretion rates (order of $10^{-5} - 10^{-4} M_\odot\,\mathrm{yr}^{-1}$) unless some feedback from the star stops mass accretion. For 'Y-series' models, realistic mass accretion rates obtained with cosmological simulations, the tendency is similar. The final mass reaches over $300 M_\odot$, in the mass range where the star causes core-collapse to form a black hole, even for the model with mass accretion rate dropped by one order of magnitude from dM_Y/dt.

This is primarily due to long lifetime of the star. We calculate VMS stellar evolution with no accretion, i.e., the star initially has the same mass and evolve holding its mass. It is very useful that we compare models with and without mass accretion. We perform 85, 180, 385, 460, 700, $920 M_\odot$ star models, whose mass corresponds to the final masses of our models with accretion ('C-' or 'Y-series'). We call these no mass accretion models 'N-series'. These models are calculated in the same way as 500 and $1000 M_\odot$ stellar evolution in Ohkubo et al. (2006). In Table 3.2 we list

Table 3.2. Stellar mass, lifetime, and final fate for 'N-series'.

Models	Mass ($M_\odot$)	lifetime (yr)	final fate
N-1	85	3.7×10^6	Core-Collpase
N-2	180	2.8×10^6	PISN
N-3	275	2.6×10^6	PISN
N-4	460	2.4×10^6	Core-Collapse
N-5	700	2.2×10^6	Core-Collapse
N-6	920	2.2×10^6	Core-Collapse

lifetime and final fate of 'N-series'. The lifetime of a very-massive star without accretion is $2-3 \times 10^6$ years, which does not sensitively depend on mass because there is relation $L \propto M$. Especially stars over $\gtrsim 400 M_\odot$ have almost identical lifetime, $(2.2 \pm 0.2) \times 10^6$ years (see, e.g. Heger et al. 2005; Ohkubo et al. 2006). On the other hand, our 'C-series' and 'Y-series' models with mass accretion have longer lifetime compared with the 'N-series' even if the final mass is the same. For example, the final mass of model C-3 is $460 M_\odot$, and its lifetime is 4.6×10^6 years, nearly twice that of $460 M_\odot$ model without accretion (model N-3). Stars with mass accretion go through the lower mass phase. Model C-3 star reaches main sequence phase at $\sim 17 M_\odot$, in an ordinary massive star range. At this stage, luminosity is lower, and the stellar luminosity increases with mass. This makes stellar lifetimes longer. This trend is conspicuous for lower mass accretion rate. For 'Y-series', lifetime is also longer for models Y-3, Y-4, Y-5, but the situation is not as clear as 'C-series'. The lifetime of model Y-4 is much shorter than that of model C-3 although the final mass for model Y-4 is $385 M_\odot$, smaller than that of model C-3. This is because mass accretion rates of 'Y-series' are very high in the low mass phase, $\gtrsim 10^{-3} M_\odot \, \mathrm{yr}^{-1}$. For model Y-3, stellar mass reaches $\sim 100 M_\odot$, in the range of VMS, when the star settles into the main sequence. This contrasts to the model C-3. That is why lifetime of model Y-3 is short. For models Y-1 and Y-2, stellar mass already exceeds $100 M_\odot$ and mass increases rapidly. Therefore lifetime does not become shorter compared to that of the corresponding mass star without mass accretion (models N-5 and N-6).

For models YII and 'M-series', mass accretion stops during KH contraction or the early stage of H burning. Therefore, the final mass is fixed at the very point

where mass accretion stops, and the stellar lifetime is almost identical with no mass accretion stellar models. For example, for model M-1, whose final mass is $321 M_{\odot}$, the lifetime is 2.2×10^6 years. This is same as those of models N-4 through N-6. Regards to the lifetimes of models YII and M-3, they are also compatible with the lifetimes of no accretion stellar models (see table 1 in Marigo et al. 2001).

Figure 3.6 clearly shows the timescales of central hydrogen and helium burning. For massive stars ($M \gtrsim 20 M_{\odot}$), CNO cycle is main energy source at main sequence, and the central temperature is around 1×10^8K and kept constant. One example of a very massive star without mass accretion is also plotted for comparison. For mass accreting models, the timescale of hydrogen burning is longer even if the final mass is in the range of VMS. After hydrogen exhaustion, the central temperature increases and central helium burning follows. At that phase $\log T_c$ is $8.4 - 8.5$. After helium exhaustion, the star contracts and the central temperature increases in short timescale toward a later burning phase. For C-1, mass accretion is too low, and so the star reached the main sequence phase before stellar mass reaches $\gtrsim 20 M_{\odot}$. At lower mass, nuclear energy generation by *pp* chain stops contraction and central temperature is below 10^8K (see figure 3 in Marigo et al. 2001). Note that Pop III stars do not have carbon, nitrogen, or oxygen (CNO) at first. Temperature higher than 10^8K is necessary to produce CNO by the 3α reaction. Therefore, the CNO cycle does not operate below 10^8K. The central temperature of the star of model C-1 also reaches 10^8K as stellar mass increases.

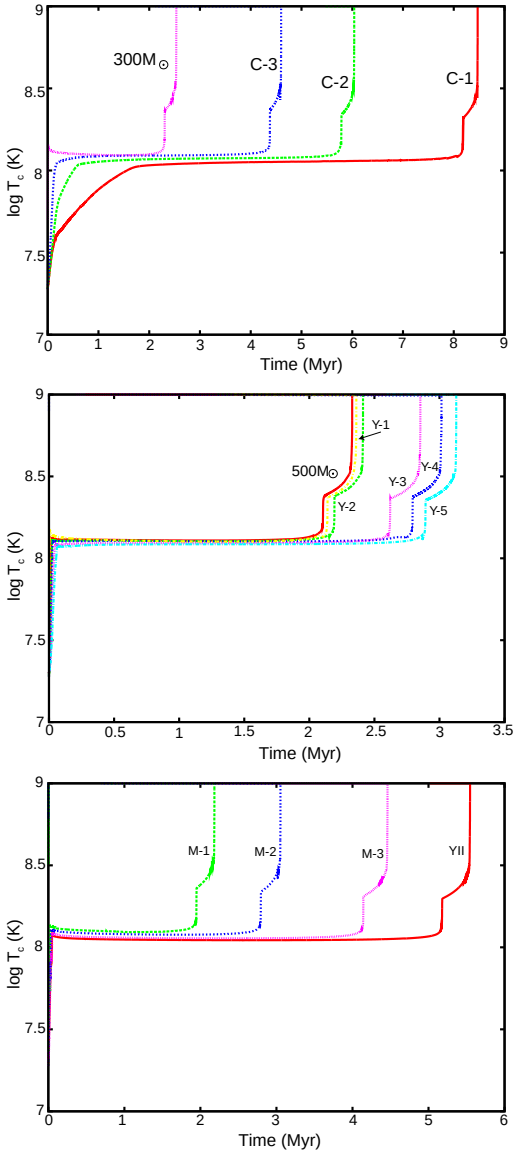

Figure 3.6 Central temperature as a function of time for each model. Note that time is expressed in a linear scale on the horizontal axis. Top panel: for 'C-series'. middle panel: for 'Y-series'. Bottom panel: for models YII and 'M-series'.

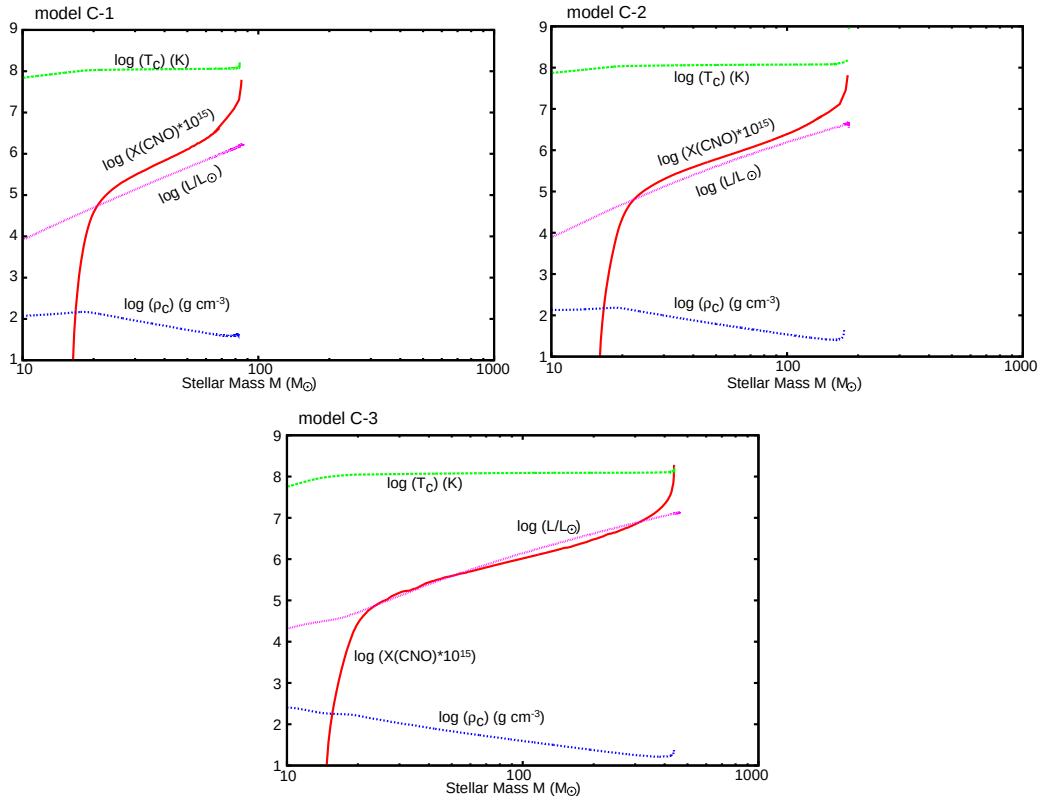

Figure 3.7 The Evolution of central temperature, central density, and CNO abundance (mass fraction) from proto stellar phase to main sequence stage for 'C-series'. Stellar luminosity is also plotted. The central CNO mass fraction is normalized to 10^{15} to put in one graph.

3.2 Proto stellar evolution before reaching main sequence

The overall situations through mass increase are sketched in the previous subsection. Stellar evolution before main sequence is roughly divided into two stages: early accreting stage and Kelvin-Helmholz (KH) contraction stage. Here we describe the characteristics of these stages. Figures 3.7 through 3.9 show the the evolution of central temperature, central density ,CNO abundance (mass fraction), and stellar luminosity. CNO abundance means the total quantity of carbon, nitrogen, and oxygen. Note that CNO mass fraction is normalized to 10^{15} to put in one graph. We discussed these cases using these figures and Figure 3.1 in section 3.1.1.

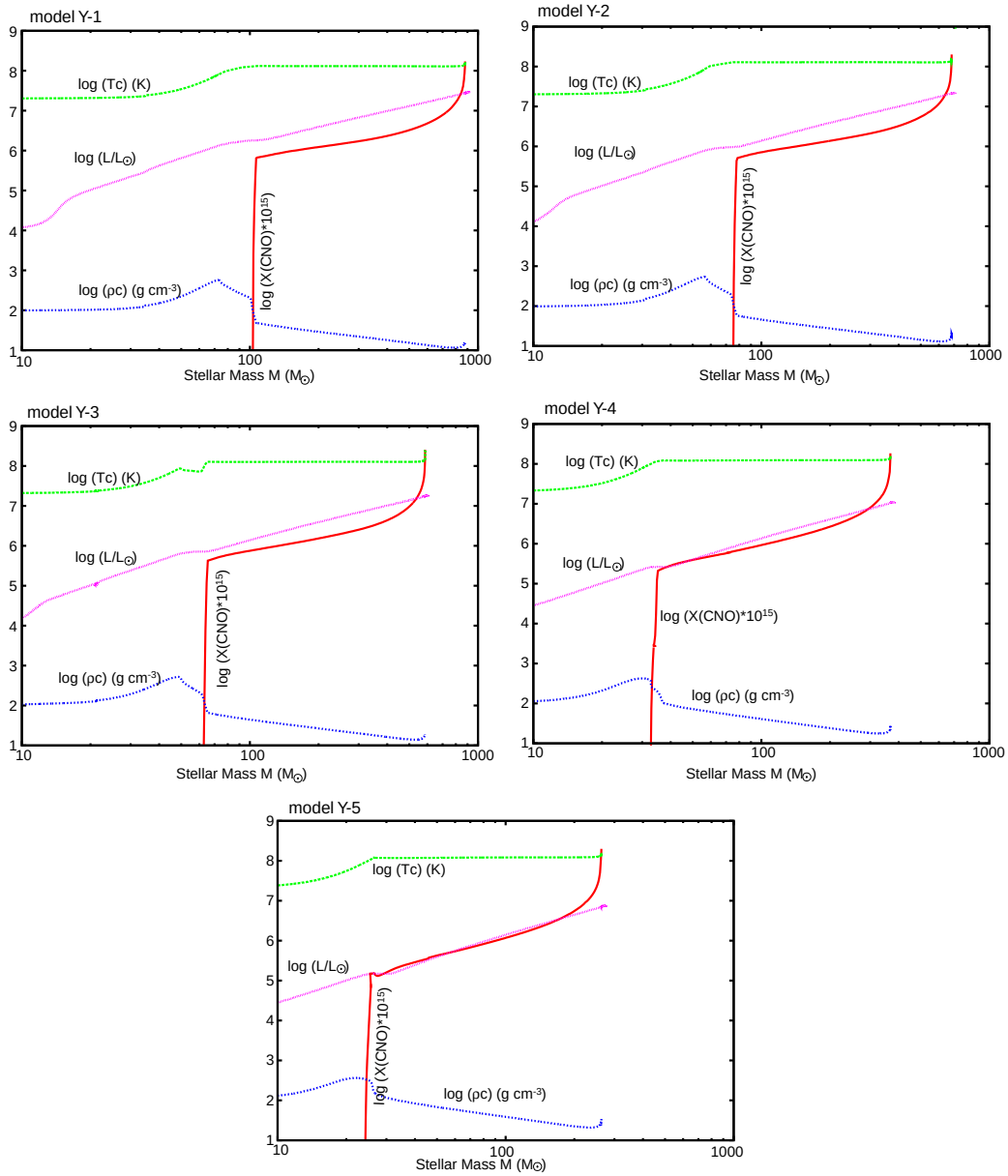

Figure 3.8 Same as Figure 3.7, but for 'Y-series'.

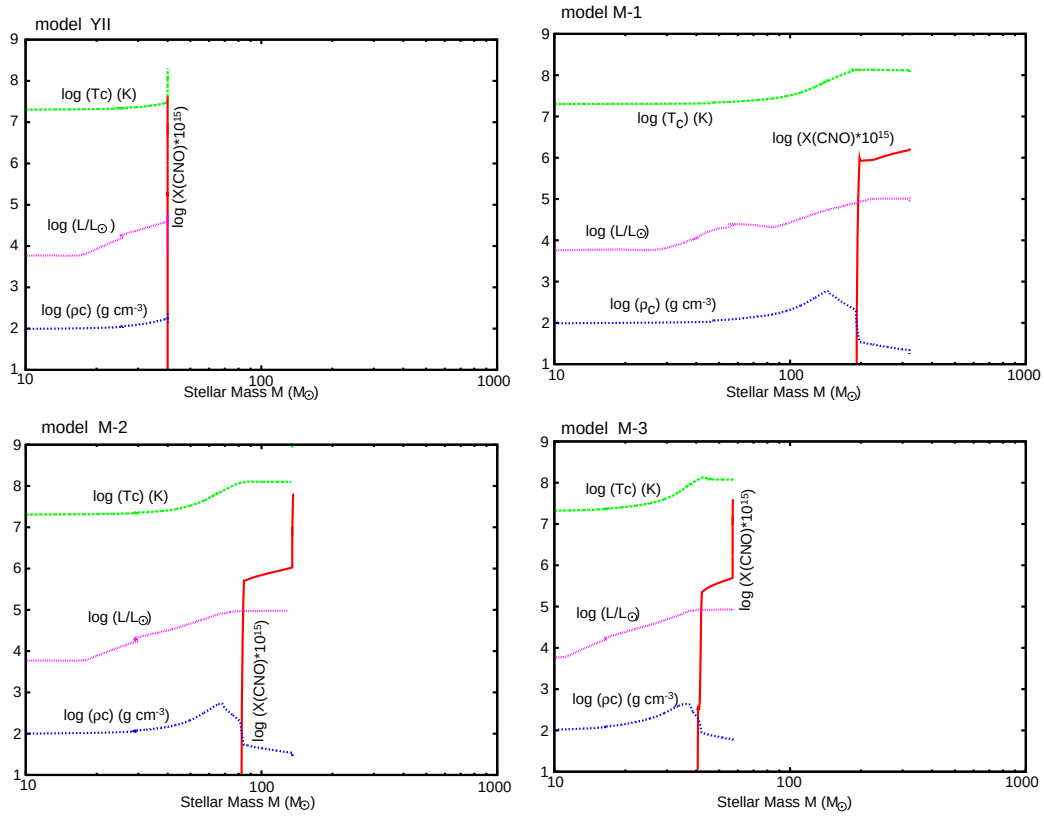

Figure 3.9 Same as Figure 3.7, but for models YII and 'M-series'.

3.2.1 Early accreting stage

In early evolutionary stages, accreted material piles up on the stellar surface. The Kelvin-Helmholz (KH) timescale ($\tau_{\rm KH} = GM^2/RL$, cooling time of stellar interior) is comparable to the accretion time scale ($\tau_{\rm acc} = M/\dot{M}$), as described in 3.1. The stellar radius is kept almost constant for 'Y-series' (see Figure 3.1). This situation continues until the stellar mass reaches $\sim 10 M_\odot$. As shown by Equation 3.1, the stellar radius is a function of stellar mass and mass accretion rate. We use mass accretion rate by Yoshida et al. (2006) as a function of stellar mass (Equation 2.1). Comparing the two equations, one can see that the stellar radius is almost constant through this phase. As stellar mass increases, the heat deposited in the stellar interior escapes outward as a luminosity wave, and the star swells. After that, the star begins to contract (KH contraction). The turning point from the adiabatic accretion to KH contraction

phase corresponds to the point at which the central temperature and central density begin to increase in Figure 3.8.

For 'C-series', mass accretion rates are low, and KH contraction directly follows after the initial expansion (section 3.1.1).

3.2.2 Kelvin-Helmholz (KH) contraction stage

Stellar luminosity increases (it exceeds $10^5 L_\odot$ for 'Y-series') and KH contraction time scale becomes shorter than the accretion time scale. The central temperature and central density gradually increase. However, the temperature is still below 10^8K. With the temperature in the order of 10^7K, most of hydrogen burning is operated by *pp* chain reaction. As mentioned in section 3.1.2, the primordial gas does not include CNO, which are not synthesized by big bang nucleosynthesis. Therefore CNO cycle is not operative below 10^8K. The energy supplied by *pp* chain is not enough to stop the contraction, because energy generation rate i.e. reaction rate of *pp* chain saturates at high temperatures. Therefore, the star continues to contract and hence the central temperature and central density increase further.

When the temperature exceeds 10^8K, 3α reaction (helium burning) occurs and a slight amount of carbon is produced. The synthesized carbon is the seed for CNO cycle and slight CNO abundance ($10^{-10} - 10^{-9}$) is enough to operate CNO cycle (Figures 3.7 through 3.9). A part of energy supplied by the nuclear burning is used to heat the stellar interior as well as offer a source for stellar luminosity, so the specific entropy increases and the central density decreases. The reaction rate of CNO cycle is much sensitive, i.e. a much higher power function of temperature ($\propto T^{16-18}$) than *pp* chain ($\propto T^{4-6}$), and so the energy generation is mainly supplied by CNO cycle. This stops the contraction of the star and the star settles into the main sequence phase. After reaching main sequence, moderate hydrogen burning continues for duration of the order of 10^6 years. Mass accretion continues through the evolution in our models. Stellar luminosity increases and central density decreases adjusting to of corresponding stellar mass of main sequence stars, whereas the central temperature is kept constant near 10^8K through main sequence.

Model C-1 provides an exceptional results. The star reaches main sequence i.e. stops to contract before the central temperature exceeds 10^8K.

3.3 Stellar evolution through nuclear burning

After settling into main sequence, the star evolves by consuming hydrogen. Helium is produced as ash and accumulates in the central region. After hydrogen exhaustion, central temperature increases and helium burns as a new fuel , and carbon and oxygen are left as ash. Carbon burning follows that, and then neon burning, oxygen burning, and silicon burning. It depends on the stellar mass whether the star causes iron core-collapse to form a black hole or explodes as a PISN. In this section, we describe each burning stage in detail and discuss characteristics comparing each model.

3.3.1 Hydrogen burning (main sequence)

The star spends longest time in the main sequence phase through its life ($\sim 90\%$). Its life time is mostly determined by the time scale of this phase and hence also the final mass it grows into with mass accretion. The discussion of lifetime and final mass is summarized in section 3.1.2. Here we describe the stellar interior condition, especially the site where the nuclear burning occurs.

Figure 3.10 shows evolution of central hydrogen mass fraction. The central temperature is kept at $\sim 1 \times 10^8$K throughout main sequence (Figure 3.6, but model C-1 is an exceptional case as described in section 3.1.2). In the latter half of main sequence, hydrogen decreasing pace accelerates. This is due to the combined effect of luminosity (i.e. the increase of hydrogen consumption per unit time) as the stellar mass increases by mass accretion and the decrease of a fully convective region, as described in the next paragraph. Hydrogen is exhausted in the center after $2-3 \times 10^6$ years for 'Y-series'. It takes longer time for the central hydrogen to be exhausted for 'C-series', model YII, and model M-3 for which luminosity is lower.

Figure 3.11 - 3.14 show hydrogen mass fraction as a function of mass coordinate at several points of hydrogen burning. One can see the convective core size at each point. At the very beginning of hydrogen burning, most of the whole star is fully convective. The fully convective (uniform chemical composition) region for the total stellar mass gradually becomes smaller as hydrogen is consumed. This tendency is common for a star with or without mass accretion. For stars with mass accretion ('C-' and 'Y-series'), the mass of a fully convective core becomes larger during the first half of hydrogen burning as the stellar mass increases, but smaller in the latter half in the mass fraction normalized to the total stellar mass. The fully convective core does not

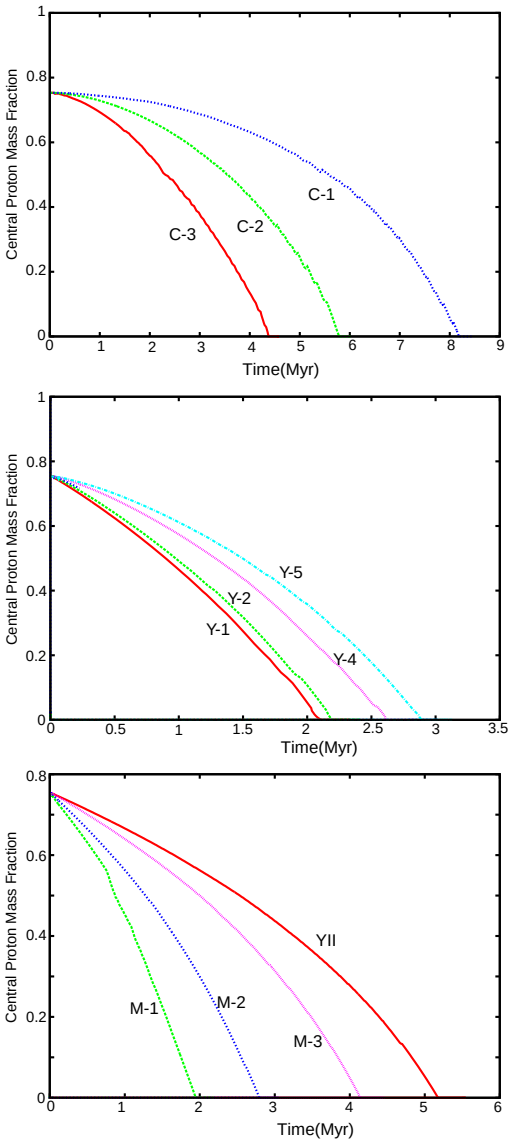

Figure 3.10 The change of central hydrogen mass fraction. The time on the horizontal axis is expressed in linear scale. Top panel: for 'C-series'. Middle panel: for 'Y-series'. Bottom panel: for models YII and 'M-series'.

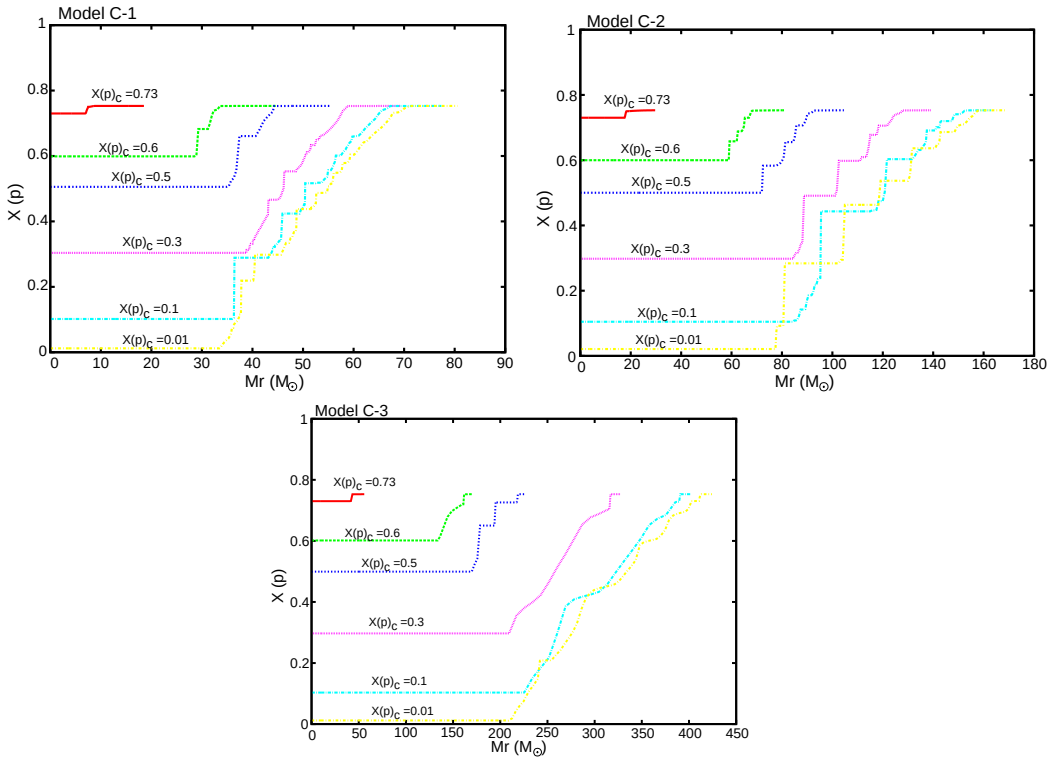

Figure 3.11 Snapshots of mass fraction of hydrogen as a function of mass coordinate when the central hydrogen mass fraction is 0.73 (the very beginning of main sequence), 0.6, 0.5, 0.3, 0.1, and 0.01 (the end of hydrogen burning). For 'C-series'.

grow in the latter half. At the end of main sequence, the fully convective region (i.e. a helium core) is $\sim 50\%$ of the whole star. For models YII and 'M-series', accretion stops before or during early stage in main sequence. The convective core shrinks as no accretion models ('N-series').

Figures 3.15 and 3.16 are temperature structure. Figure 3.17 and 3.18 are energy generation rate per unit mass by nuclear reaction ($\epsilon_{\rm n}$) for some models. For stars with mass accretion, temperature at the same mass coordinate increases as the stellar mass increases (i.e. the star evolves) and so does $\epsilon_{\rm n}$. The position at the same mass coordinate becomes further inward ($q = m/M$ becomes smaller) as the stellar mass increases. On the other hand, for stars without mass accretion ('N-series') or stopped mass accretion models (YII and 'M-series'), temperature and $\epsilon_{\rm n}$ slightly decreases. This is because the outer region slightly expands through the evolution.

The energy generation by nuclear reactions is considerably concentrated toward

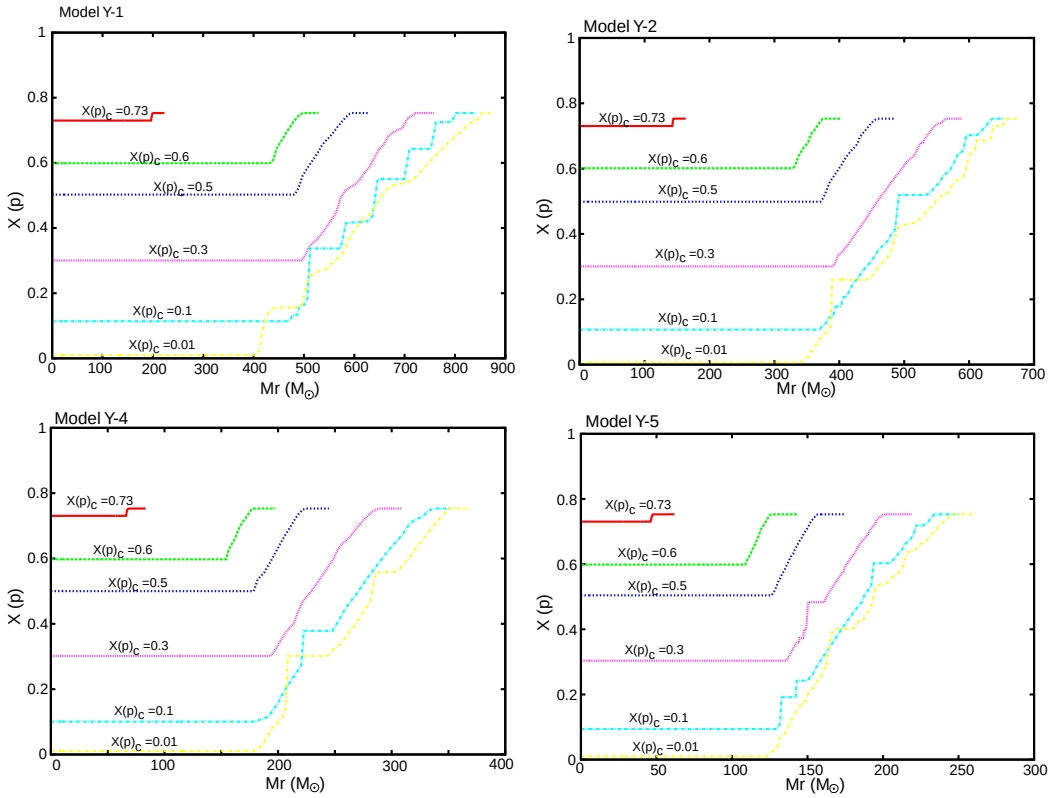

Figure 3.12 Same as Figure 3.11, but for 'Y-series'.

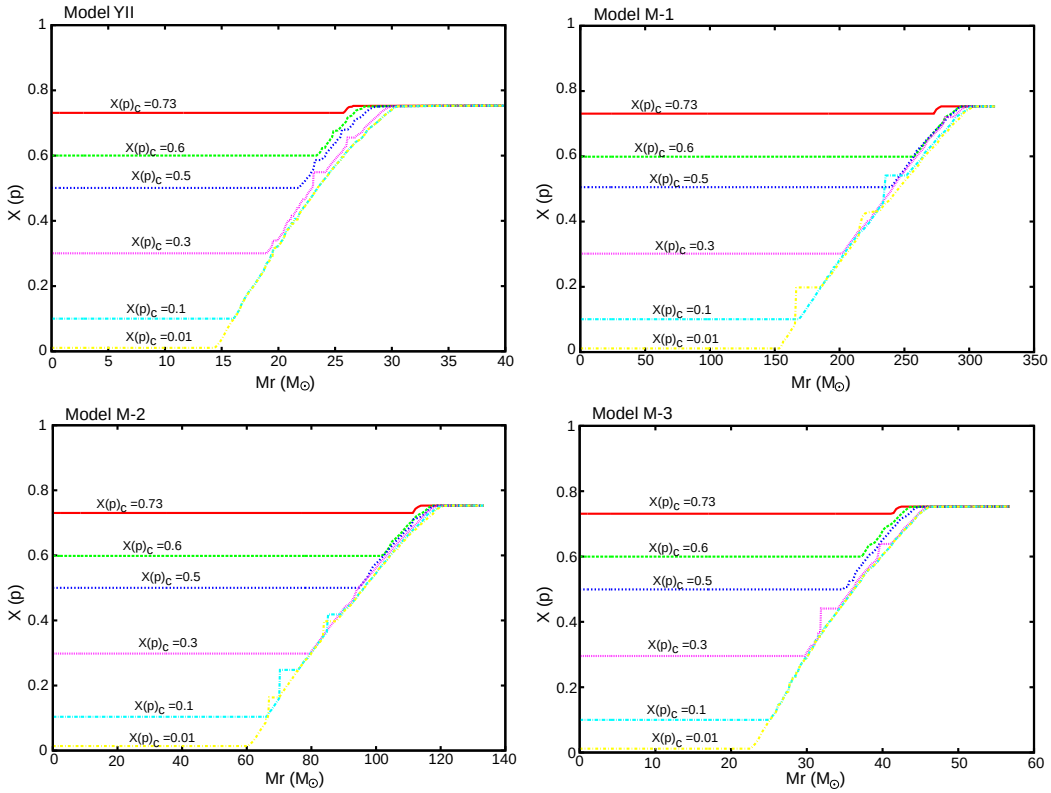

Figure 3.13 Same as Figure 3.11, but for models YII and 'M-series'.

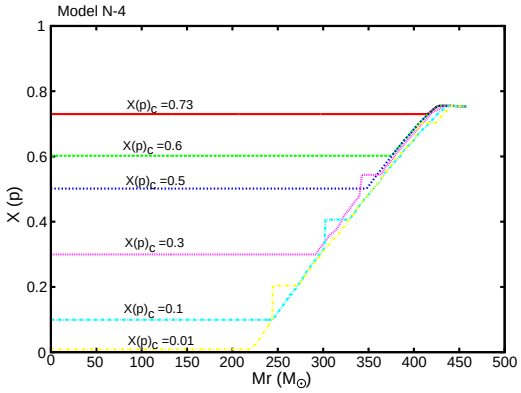

Figure 3.14 Same as Figure 3.11, but for Model N-4.

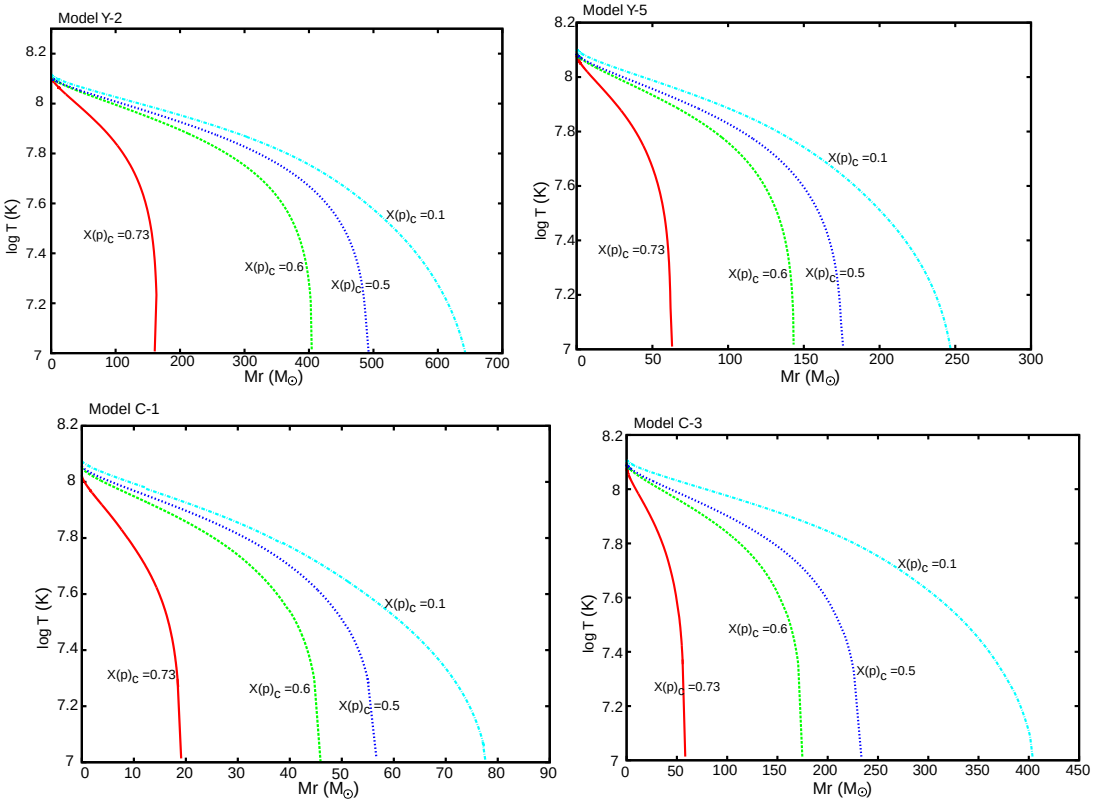

Figure 3.15 Temperature structure when the central hydrogen mass fraction is 0.73, 0.6, 0.5, and 0.1.

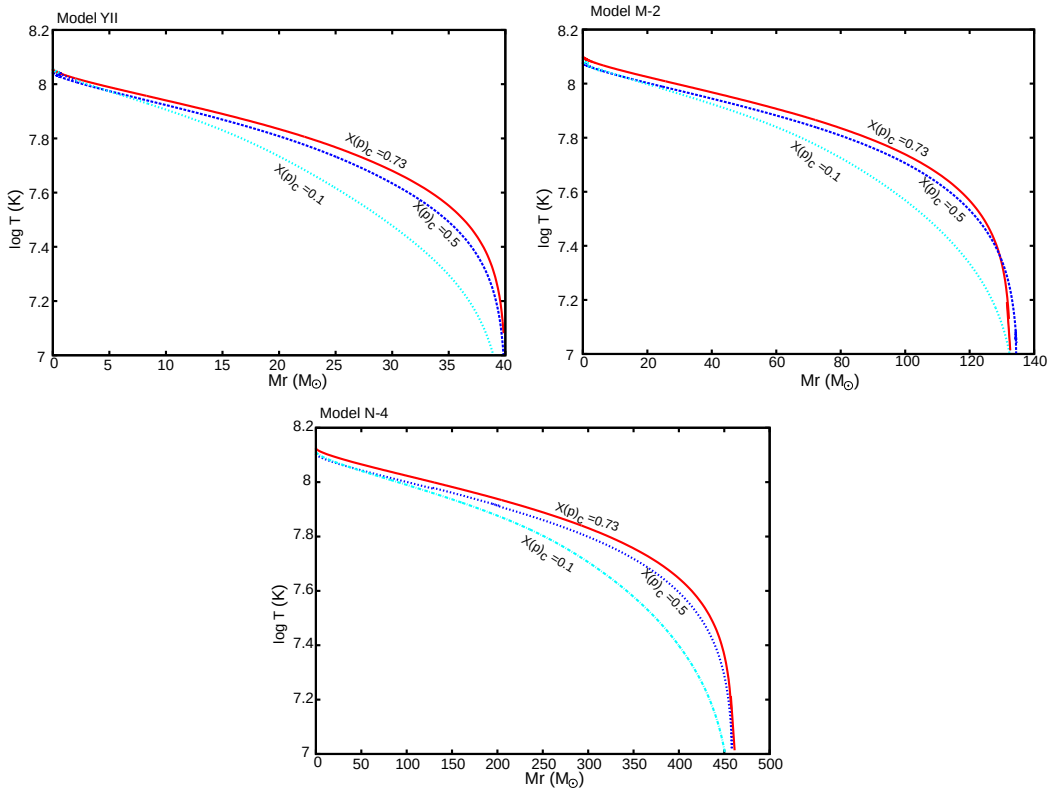

Figure 3.16 Same as Figure 3.15, but for models YII, M-2, and N-4. The structure for $X(p)_c = 0.6$ is not plotted to avoid making the graph too crowded.

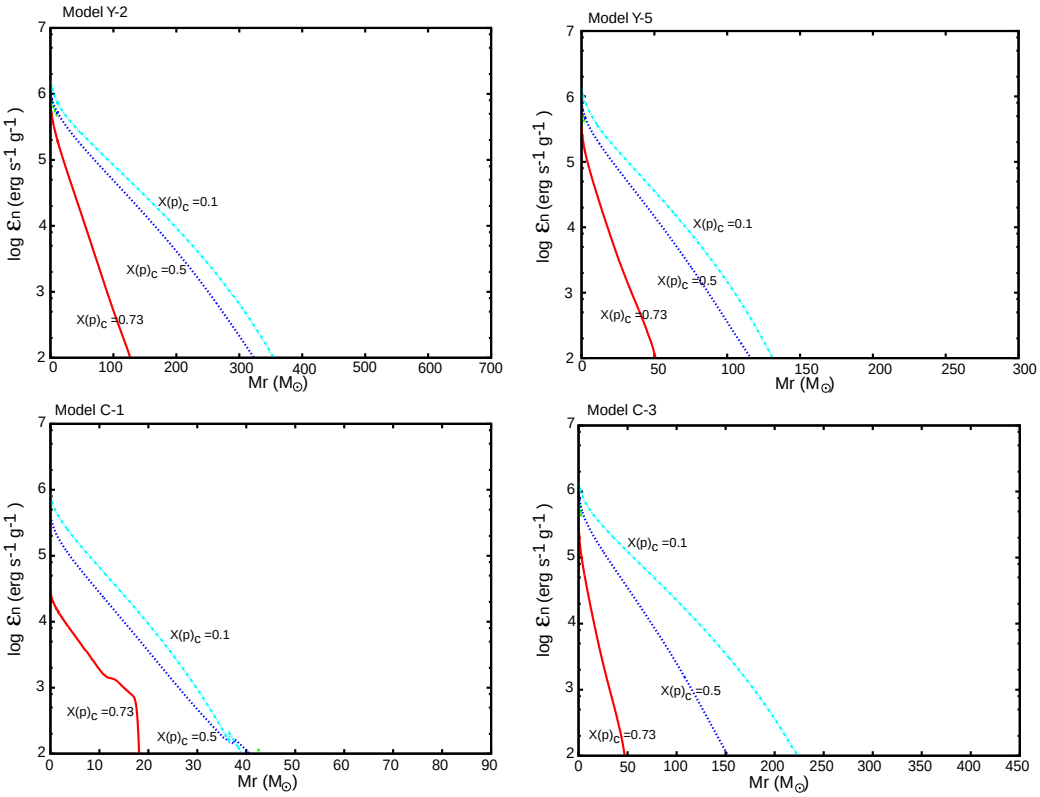

Figure 3.17 Nuclear energy generation rate per unit mass when the central hydrogen mass fraction is 0.73, 0.5, and 0.1.

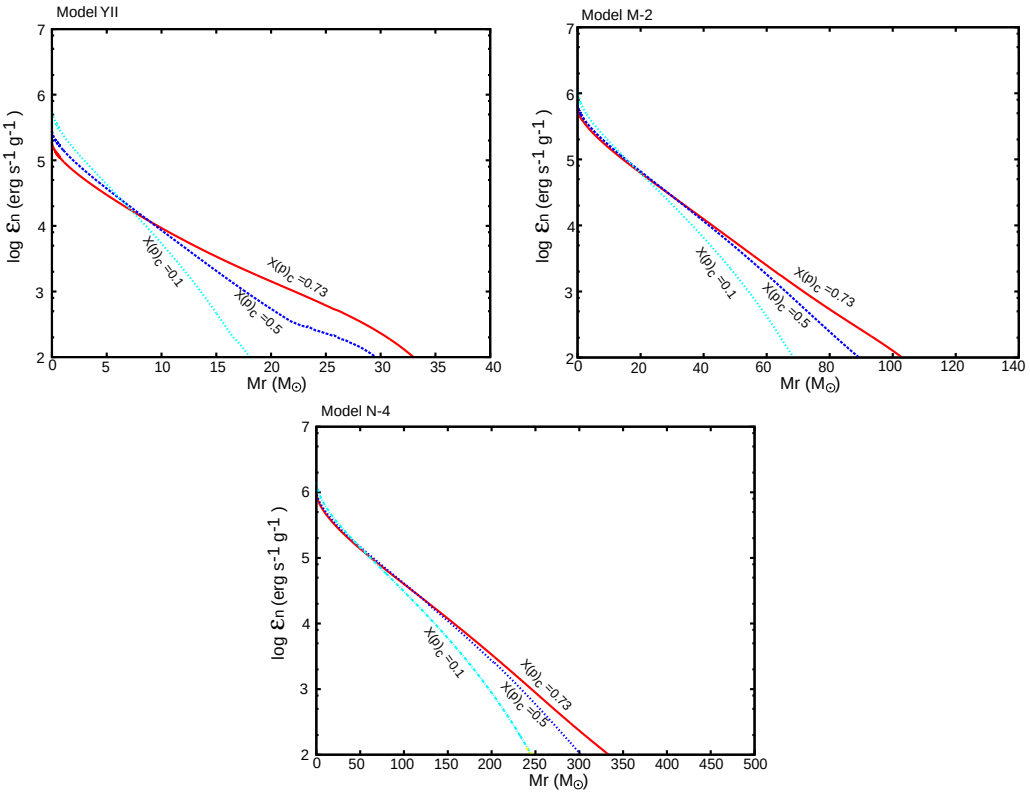

Figure 3.18 Same as Figure 3.17, but for models YII, M-2, and N-4.

the central region. For example, half of the total nuclear energy generation takes place in the central 0.7% of the total stellar mass, 90% in the central 5%, and 99% in the central 14% region, when $X(p)_c = 0.5$ for model Y-2. The total stellar mass at that time is $490 M_\odot$, the central temperature is $\log T_c = 8.105$, $\log T(q = 0.007) = 8.097$, $\log T(q = 0.05) = 8.071$, and $\log T(q = 0.14) = 8.033$, respectively. The fact that the temperature gradient is moderate whereas the $\epsilon_{\rm n}$ gradient is acute is the characteristics of the CNO cycle. Nuclear reaction rate of CNO cycle is very sensitive to temperature. In the left panel of Figure 3.19 we plot $\log T$ v.s. $\epsilon_{\rm n}$ for some models when $X(p)_c = 0.5$. In the inner area where $\log T > 7.8$ there is a relation $\epsilon_{\rm n} \propto T^{14}$. Note that contrary to the proto stellar phase, CNO cycle occurs in the region where $\log T < 8$ because CNO synthesized in the central ($\log T > 8$) region is first conveyed outward by convection, although the contribution of $\epsilon_{\rm n}$ there to the total stellar luminosity is negligible. In the right panel $\log T$ v.s. $\epsilon_{\rm n}$ when $X(p)_c = 0.73$ is plotted. In the beginning of hydrogen burning the difference between model C-1 and other models is clear. $\epsilon_{\rm n} \propto T^4$ in the inner region of model C-1 whereas $\epsilon_{\rm n} \propto T^{14}$ for model Y-2 already. This means that for the star of model C-1 the energy is supplied by *pp* chain reaction at that time, whose reaction rate dependence on temperature is much weaker than that of CNO cycle.

The central temperature is kept constant ($\sim 1 \times 10^8$ K) through main sequence. The luminosity changes due to accretion is covered by increasing mass fraction, X(CNO). X(CNO) $\sim 10^{-10}$ at the beginning of main sequence, but it increases up to $\sim 10^{-8}$ toward the end of this stage (see Figures 3.7 through 3.9).

In Table 3.3 we summarize total consumed hydrogen amount when the central hydrogen mass fraction $X(p)$ is 0.01 (the end of main sequence, $t = t_p$ hereafter). Roughly 70% of hydrogen supplied as fuel at that point is consumed for models Y-1 - 5, M-1, and C-3, whose mass reaches the VMS mass range at that point. This trend is common for models with and without mass accretion (see the data of model N-4). This ratio is lower for less massive models, 61% for model C-1, 53% for model YII. These stars are less massive than $100 M_\odot$, and the convective core is smaller.

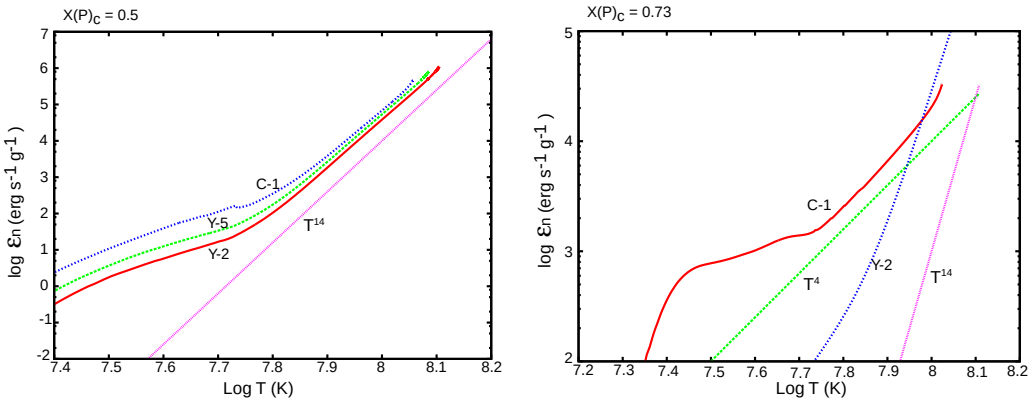

Figure 3.19 Left panel: nuclear energy generation rate as a function of temperature for model Y-2, Y-5, and C-1 when the central hydrogen mass fraction is 0.5. The line for the function $\epsilon_{\rm n} \propto T^{14}$ is plotted for comparison. Right panel: nuclear energy generation rate as a function of temperature for model Y-2 and C-1 when the central hydrogen mass fraction is 0.73. The lines for the functions $\epsilon_{\rm n} \propto T^{14}$ and $\epsilon_{\rm n} \propto T^{4}$ are plotted.

Table 3.3. Time when the central hydrogen mass fraction $X(p)$ is 0.01 ($t = t_p$ hereafter), stellar mass at $t = t_p$, consumed hydrogen mass Δp at $t = t_p$, and the mass fraction of consumed hydrogen (defined as $\Delta p/0.753M(t_p)$).

Models	t_p (yr)	Mass ($M_\odot$) at $t = t_p$	$\Delta p(M_\odot)$ at $t = t_p$	$\Delta p/0.753M(t_p)$
C-1	8.15×10^6	83	38	0.61
C-2	5.74×10^6	173	82	0.63
C-3	4.36×10^6	437	233	0.70
Y-1	2.07×10^6	876	451	0.68
Y-2	2.18×10^6	682	371	0.72
Y-3	2.20×10^6	585	415	0.71
Y-4	2.60×10^6	367	192	0.70
Y-5	2.87×10^6	262	134	0.68
YII	5.14×10^6	40	16	0.53
M-1	1.93×10^6	321	165	0.68
M-2	2.76×10^6	135	66	0.65
M-3	4.10×10^6	57	25	0.59
N-4	2.14×10^6	460	240	0.69

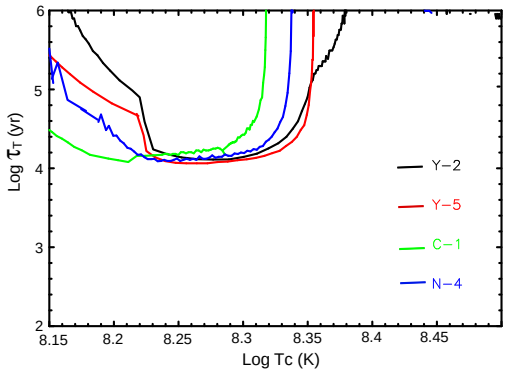

Figure 3.20 Time scale for central temperature increase as a function of central temperature $\log T_c$ from the end of hydrogen burning to the beginning of helium burning. It is defined by $\tau_T = T/\dot{T}$. The data for models Y-1, Y-5, C-1, and M-2 are plotted.

3.3.2 Helium burning

After hydrogen exhaustion at the center, the central helium core loses energy source and contracts. As the core contracts, the central density and temperature increases until the temperature becomes high enough for helium to burn so that energy supply can cover the stellar luminosity. This phase is much shorter than the time scales of hydrogen burning, the previous stage, or helium burning, the following stage. Figure 3.20 shows the time scale for central temperature increase in the form of $\tau_T = T/\dot{T}$ for several models. After central hydrogen is exhausted (when $\log T_c \sim 8.15$, τ_T becomes shorter, $\sim 10^4$ years during contraction. When $\log T_c$ exceeds 8.3, helium burning can supply enough energy to stop the contraction and τ_T becomes longer than 10^6 years. The star enters the helium burning stage.

Figures 3.21 - 3.27 show some characteristics during helium burning for several models. In panels (a) the evolution of proton, ^{4}He, ^{12}C, and ^{16}O mass fractions at the center are plotted. The time on the horizontal axis is taken in a linear scale. We plot from the last part of hydrogen burning ($X(\mathrm{p})_c \sim 0.1$) to the helium exhaustion. As described in the previous paragraph, the contracting stage between the hydrogen and helium burning phase is short, so one can see that just after central helium mass fraction $X(^4\mathrm{He})_c$ reaches 1, it starts to decrease (helium burning starts). In helium burning, helium is converted to carbon by the reaction $^4\mathrm{He}(2\alpha,\gamma)^{12}\mathrm{C}$ and part of synthesized carbon catches another α particle to become ^{16}O ($^{12}\mathrm{C}(\alpha,\gamma)^{16}\mathrm{O}$). Through helium burning, central temperature $\log T_c$ gradually increase (8.35 - 8.5,

see Figure 3.6). In the first half of helium burning, ^{12}C mass fraction increases and peaks at around 0.4. In the latter half carbon starts to decrease by the reaction $^{12}\mathrm{C}(\alpha,\gamma)^{16}\mathrm{O}$, and oxygen is the main product. At the end of helium burning, carbon mass fraction drops to as low as ~ 0.1 (~ 0.12 in C/O ratio, $X(\mathrm{C})_c/X(\mathrm{O})_c$, at the center). It is one of characteristics of VMS that C/O ratio is very low when central helium is exhausted. For a $25M_\odot$ star, a typical ordinary massive star, C/O ratio at that time is 0.45 according to the data calculated in Umeda & Nomoto (2002). Generally, C/O ratio becomes lower as stellar mass increases (see Table 4 in Marigo et al. 2001). We also see for model YII ($40M_\odot$) C/O ratio is 0.25 at He exhaustion. At the very last stage of helium exhaustion, oxygen also starts to decrease because of the reaction $^{16}\mathrm{O}(\alpha,\gamma)^{20}\mathrm{Ne}$.

For the rest, ((b)-(f)), in Figure 3.21 - 3.27 we show snapshots at a few points. In panels (b), temperature structure when $\log T_c = 8.25$, $X(^4\mathrm{He})_c = 0.95$, 0.5, and 0.1 is shown. In (c), nuclear energy generation rate per unit mass ϵ_n is shown when $\log T_c = 8.25$, $X(^4\mathrm{He})_c = 0.95$, and 0.1. During contraction after hydrogen exhaustion, temperature increases over the whole star, and central ϵ_n is low. As helium burns efficiently at the center, hydrogen neighboring the outer edge of the helium core also starts to burn (hydrogen shell burning, the jump of energy generation corresponds to the boundary of the helium core and hydrogen shell; panels (d)-(f)). The energy generation due to this burning is comparable to that by the central helium burning. The stellar luminosity is covered by these two sources. The central temperature and density increase through helium burning ($\log T_c \sim 8.35 - 8.50$) but helium mass fraction decreases. These factors balance and keep the central energy generation rate constant. Temperature where hydrogen shell burning occurs is about 1×10^8K (panels (b)), and so CNO cycle operates there. As helium is consumed in the central region, in the inner part of the star (the inner region with shell burning) temperature gradually increases, whereas in the outer part it decreases. The shell burning spot functions as a knot.

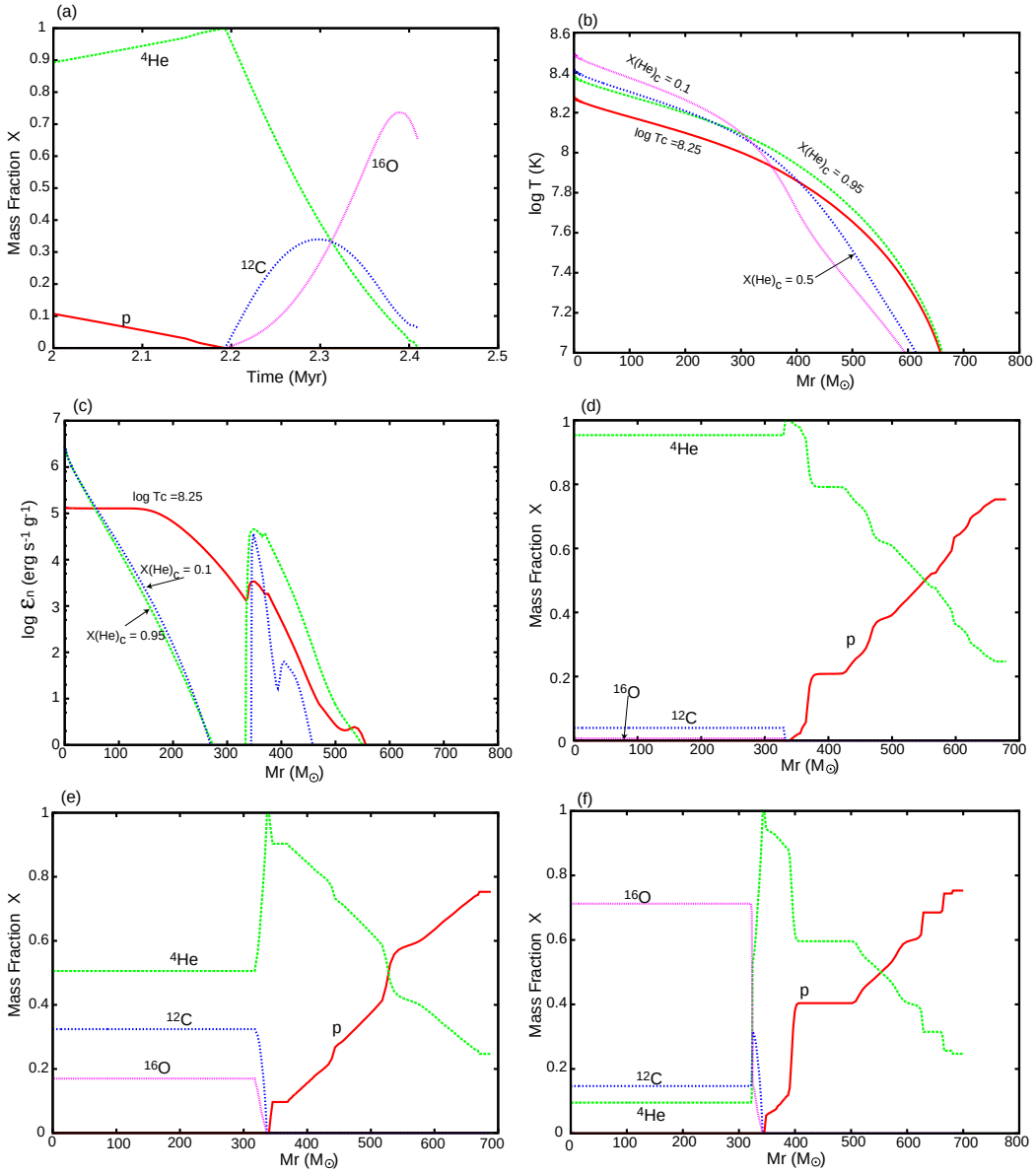

Figure 3.21 The evolution and structure during helium burning for model Y-2. (a): the evolution of central mass fractions of proton, ^{4}He, ^{12}C, and ^{16}O. (b): snapshots of temperature structure when $\log T_c = 8.25$, $X(^4\mathrm{He})_c = 0.95$, 0.5, and 0.1. (c): snapshots of nuclear energy generation rate per unit mass when $\log T_c = 8.25$, $X(^4\mathrm{He})_c = 0.95$, and 0.1. (d): the chemical composition when the central helium mass fraction $X(^4\mathrm{He})_c = 0.95$. Proton, ^{4}He, ^{12}C, and ^{16}O are plotted. (e): same as (d), but when $X(^4\mathrm{He})_c = 0.5$. (f): same as (d), but when $X(^4\mathrm{He})_c = 0.1$.

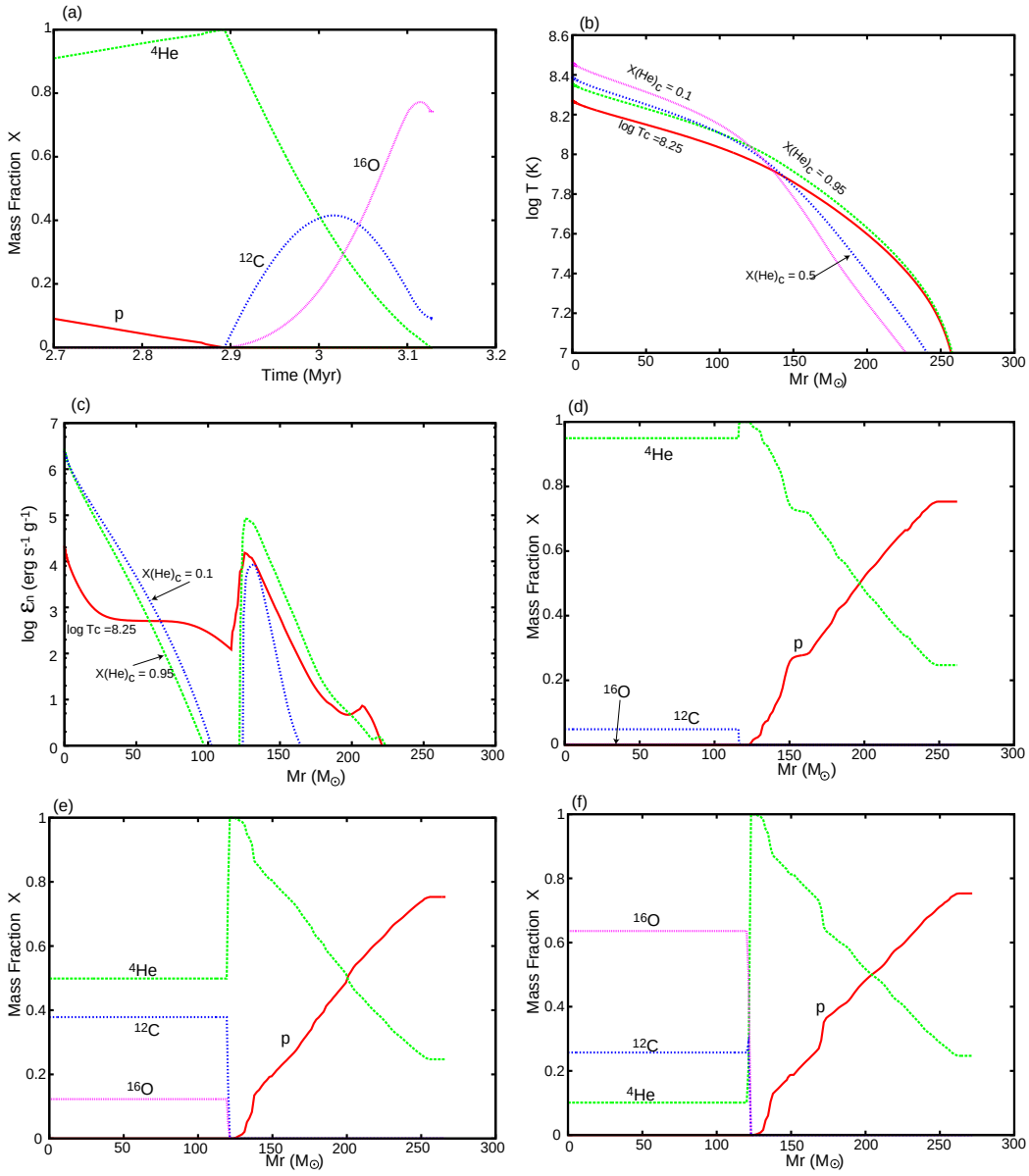

Figure 3.22 Same as Figure 3.21, but for model Y-5.

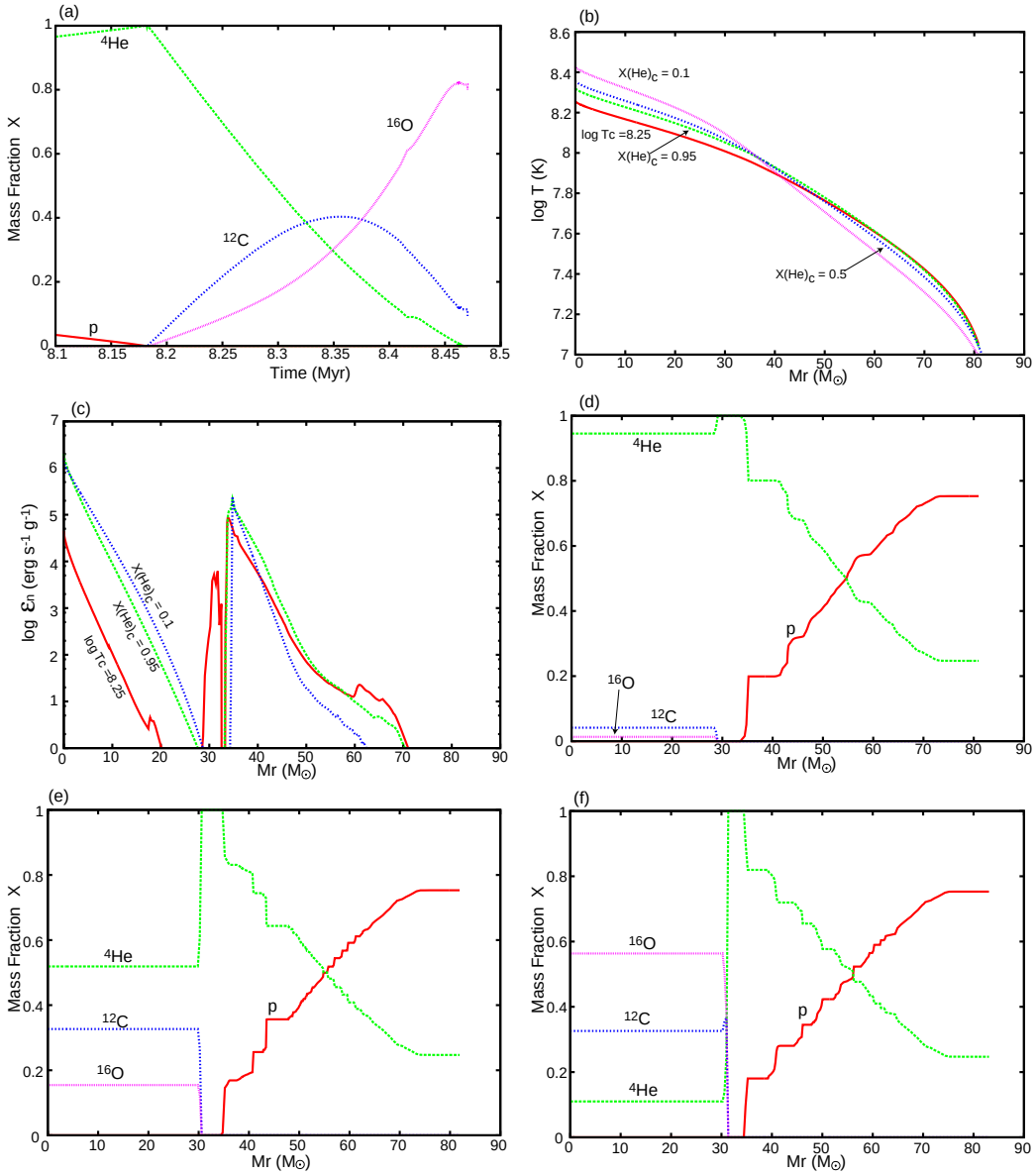

Figure 3.23 Same as Figure 3.21, but for model C-1.

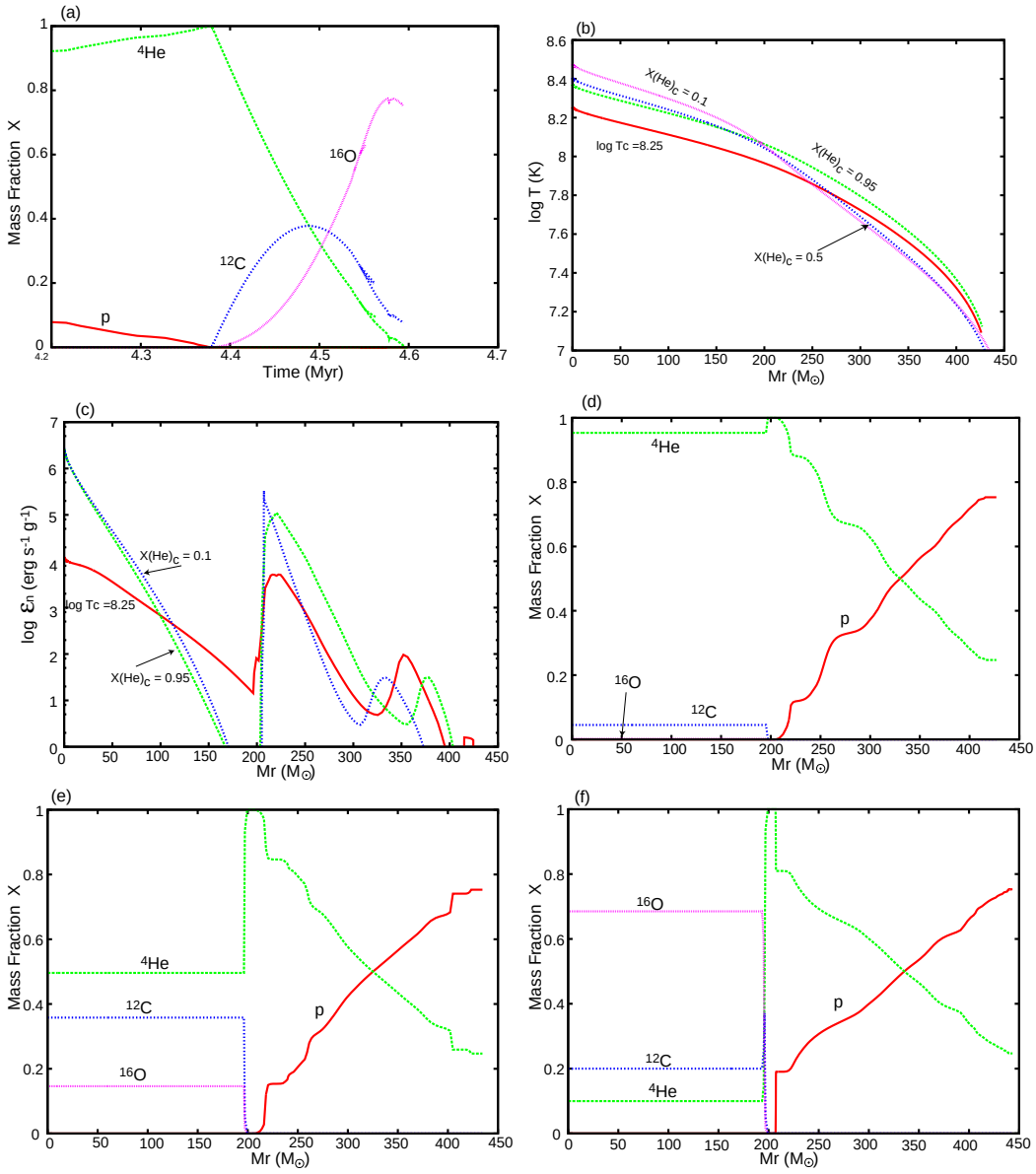

Figure 3.24 Same as Figure 3.21, but for model C-3.

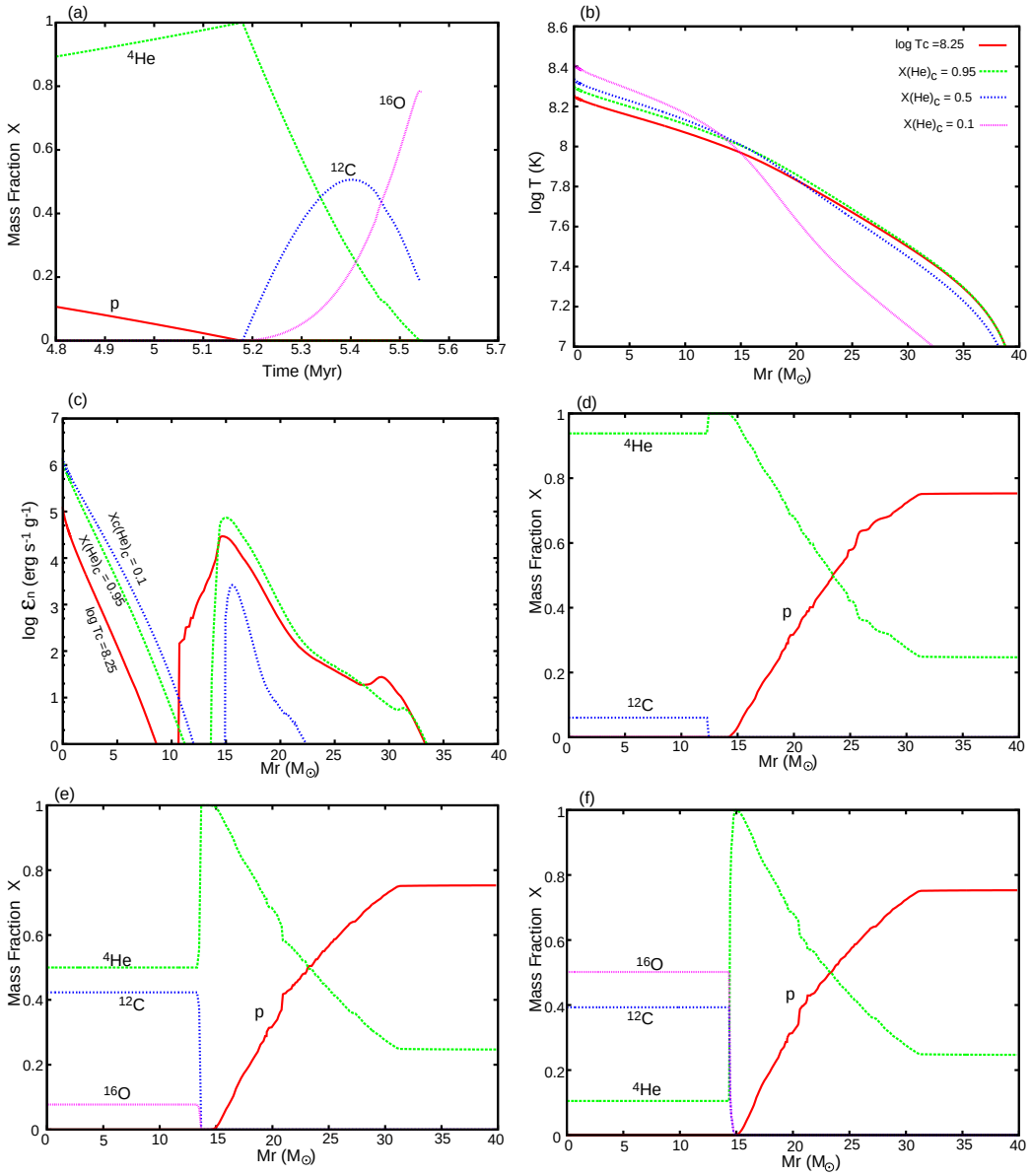

Figure 3.25 Same as Figure 3.21, but for model YII.

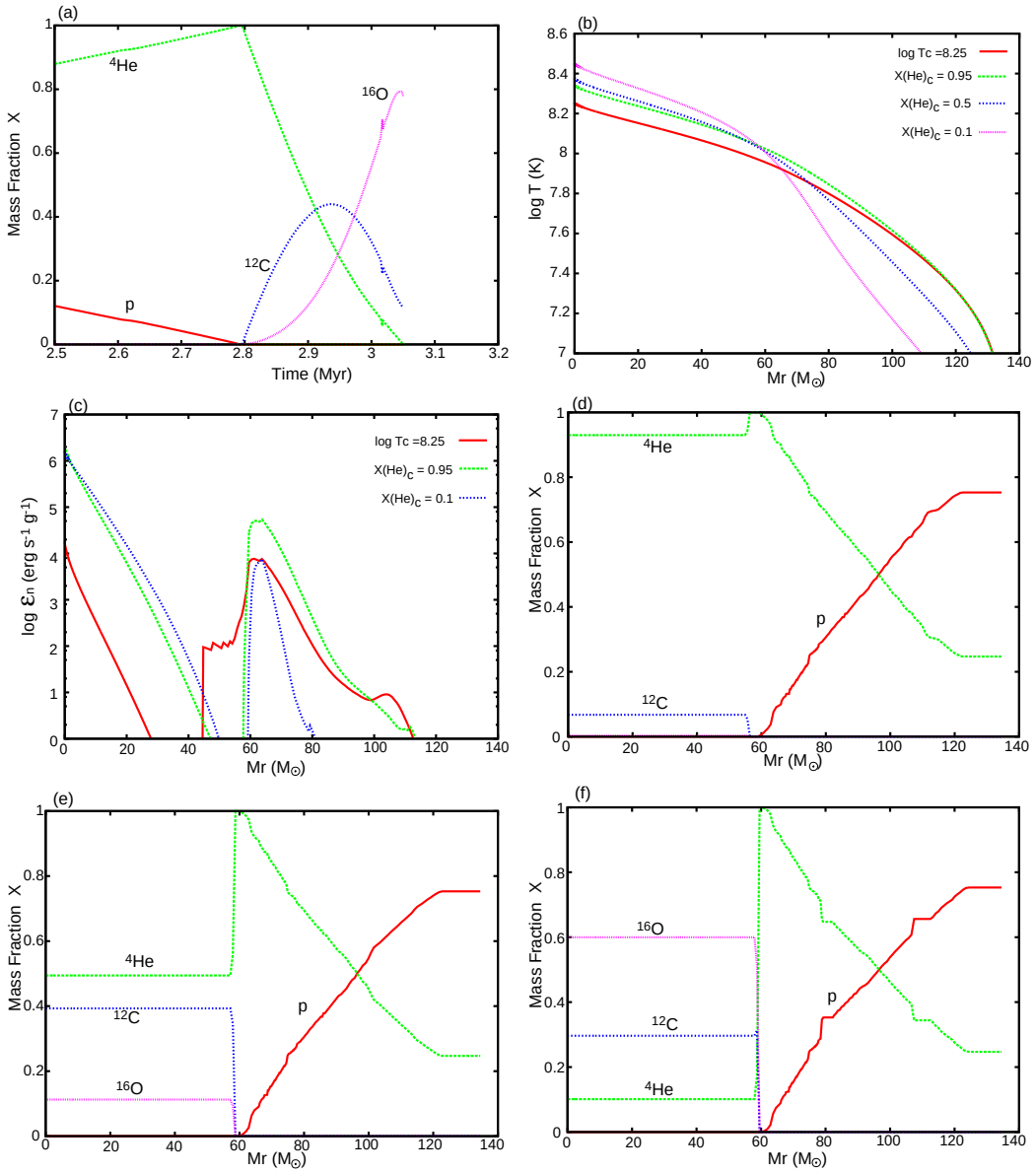

Figure 3.26 Same as Figure 3.21, but for model M-2.

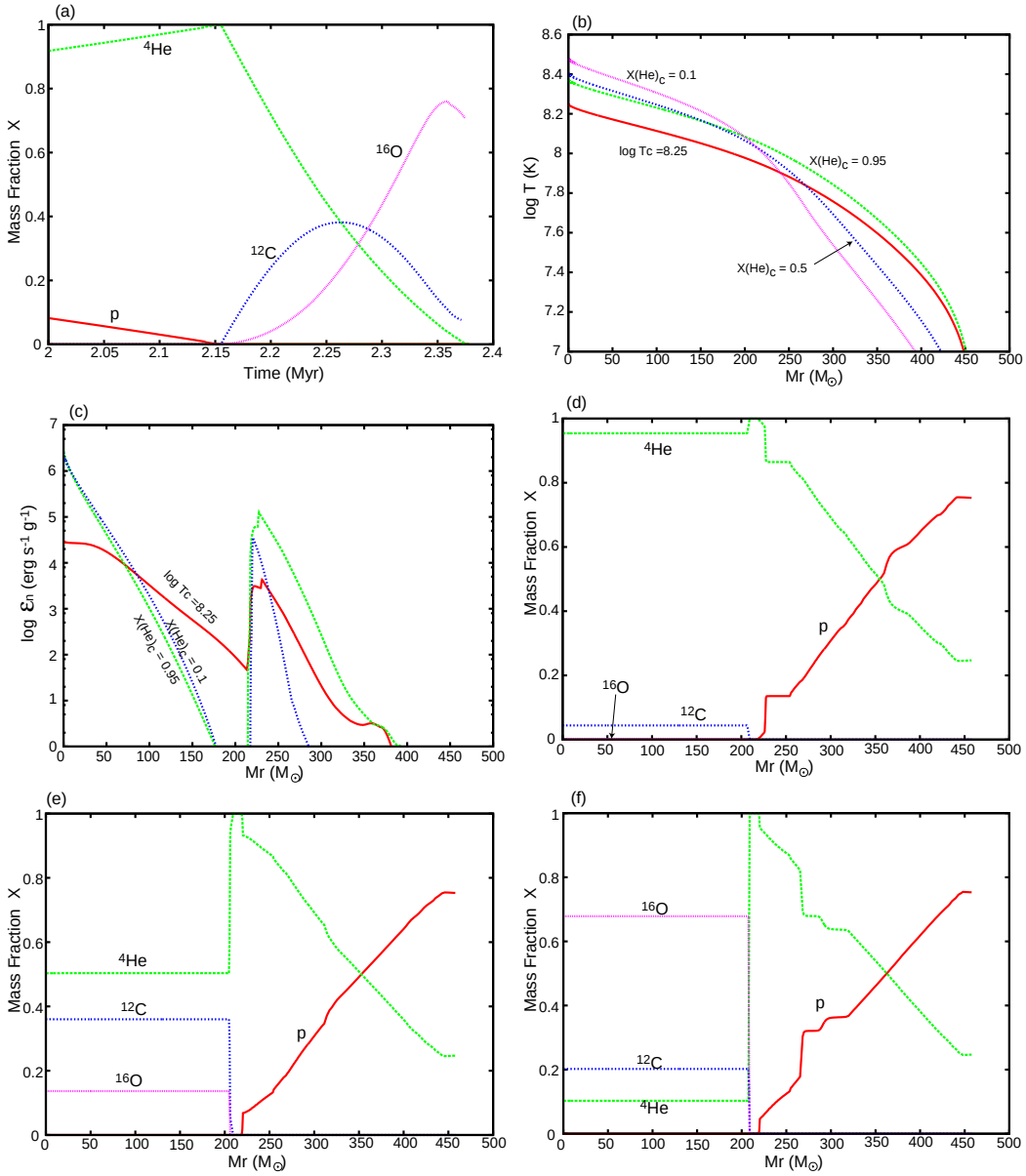

Figure 3.27 Same as Figure 3.21, but for model N-4.

Table 3.4. Final mass and CO core mass for each model.

Models	final mass $M_{\rm f}$ ($M_\odot$)	CO core mass ($M_\odot$)
C-1	85	31
C-2	180	63
C-3	460	185
Y-1	915	370
Y-2	710	320
Y-3	610	275
Y-4	385	170
Y-5	275	123
YII	40	14
M-1	321	155
M-2	135	58
M-3	57	22
N-1	85	35
N-2	180	75
N-3	275	120
N-4	460	200
N-5	700	325
N-6	920	405

^{12}C and ^{16}O are left as ashes of helium burning in the central region. ^{12}C is the main product in the core, but ^{16}O gradually becomes dominant. The CO core size (the convective core region) hardly changes through helium burning, with $\sim 40\%$ of the whole star in mass for most models. For models C-1, YII, and M-3, CO core is a little smaller than that of other models. It is a general trend that the ratio of the CO core mass to total stellar mass is larger for more massive stars.

For VMS ($M \sim 100 M_\odot$), original He core (He mass fraction is larger than 0.99 at the end of hydrogen burning) is mostly turns into CO core after helium burning (see panels (f) in each figure). As a result, pure He layer left is very thin ($\sim 10 M_\odot$ for model Y-2, for example, only 1% of the whole mass). In Table 3.4, the CO core mass for each model are summarized. For models in which mass accretion continues through helium burning ('C-series' and 'Y-series' in comparison with 'N-series'), CO core tend to be smaller ($\sim 5 - 10\%$).

3.3.3 Later burning phases

After helium exhaustion in the central region, the evolutionary time scale of the central core becomes shorter and shorter. Therefore core evolution is hardly affected by the environment of the stellar envelope, i.e., the core evolves with no relation to mass accretion. Most of our models reach the VMS mass range, and so the core evolution is qualitatively similar to that of models in Ohkubo et al. (2006).

In this subsection, we describe later burning phases (carbon, neon, oxygen, and silicon burning) in detail. Hereafter, the time scale of core evolution changes drastically. Therefore, we express each stage by central temperature instead of time in each figure.

When central helium is used up, the CO core contraction accelerates. Figure 3.28 shows time scale of central temperature increase (τ_T) in the same way as in Figure 3.20. (contraction toward helium burning). One can see that τ_T decreases drastically when temperature changes from $\log T_c = 8.6$ to 9.2. When $\log T_c = 8.6$, $\tau_T \sim 10^5$ years. It becomes $\sim 10^{-4}$ years when $\log T_c = 9.2$ for 'Y-series', model C-3 and N-4, which is in the VMS mass range. τ_T drops by as much as 9 orders of magnitude. For less massive models (models C-1, C-2, and $25M_\odot$ in Umeda & Nomoto 2002), τ_T drops a little more moderately, $\tau_T \sim 10^{-1}$ years for models C-1, YII, M-3, and $\tau_T \sim 10^0$ years for $25M_\odot$ stars. For all cases the core evolution accelerates, and that has hardly anything to do with changes in the outer envelope.

What triggers this acceleration of core evolution is that it runs out of fuel to support it. Figure 3.29 shows nuclear energy generation rate $\epsilon_{\rm n}$ per unit mass at the center for various models. Figure 3.30 shows the ratio of $\epsilon_{\rm n}$ to neutrino cooling rate ϵ_ν at the center. During helium burning, $\epsilon_{\rm n}$ is kept in the order of $10^6 {\rm erg\,s^{-1}\,g^{-1}}$. At the helium exhaustion (when $\log T_c \sim 8.6$), $\epsilon_{\rm n}$ drops dramatically and the core contracts due to neutrino cooling. Along with the core contraction, the central temperature increases and $\epsilon_{\rm n}$ eventually recovers. However, $\epsilon_{\rm n}$ becomes comparable to ϵ_ν only after $\log T_c$ exceeds 9.0. For models Y-1 - Y-4, the central region has already entered the pair instability region, and so contraction continues and $\epsilon_{\rm n}$ continues to increase beyond the line $\epsilon_{\rm n}/\epsilon_\nu = 1$. For model Y-5, the time when the central region enters the pair instability region is delayed, and so $\epsilon_{\rm n}/\epsilon_\nu$ stops to increase once it reaches near 1. However the star finally enters the pair instability region, and so $\epsilon_{\rm n}/\epsilon_\nu$ starts to increase again (for model Y-5, the star explodes as a PISN at last).

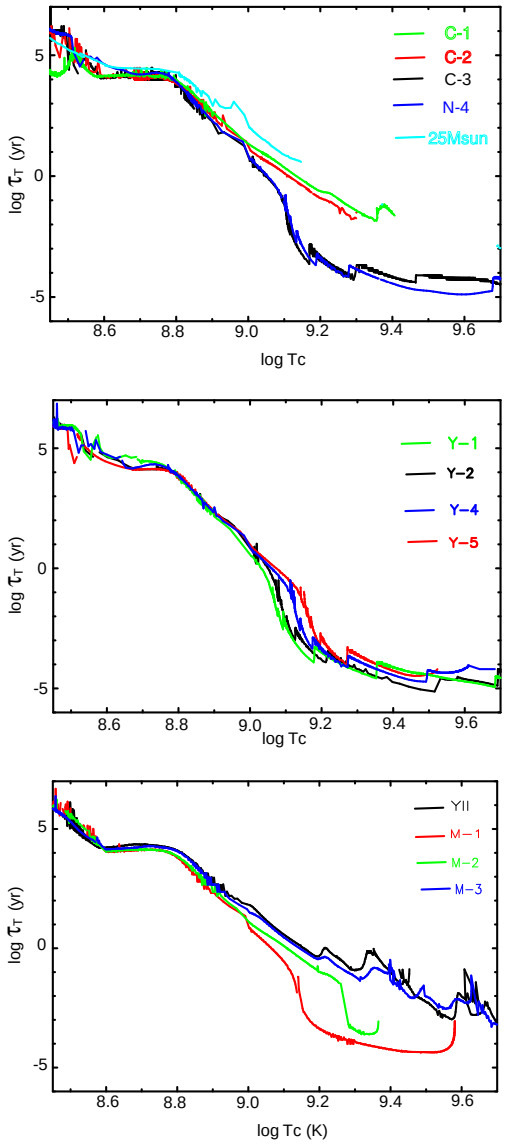

Figure 3.28 Time scale for central temperature increase as a function of central temperature logT_c after helium burning. Top panel: for 'C-series', model N-4. $25M_\odot$ star model without mass accretion is plotted for comparison. The values for later stages are not plotted for models C-1, C-2, and $25M_\odot$ star because the central temperature does not increase monotonically and figures are too crowded. Middle panel: for 'Y-series'. Bottom panel: for models YII and 'M-series'. The values for later stages are not plotted for models M-1 and M-2 because the central temperature does not increase monotonically.

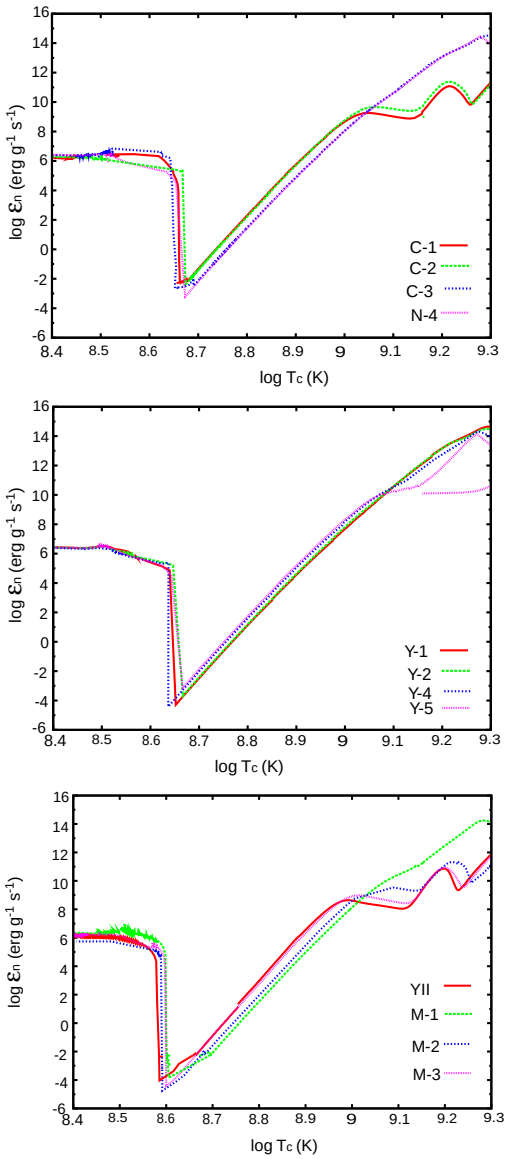

Figure 3.29 Energy generation rate per unit mass $\epsilon_{\rm n}$ at the center as a function of temperature. Top panel: for 'C-series' and model N-4. Middle panel: for 'Y-series'. Bottom panel: for models YII and 'M-series'.

There is a clear difference for lower stellar models (lower panel of Figure 3.30). Carbon starts to ignite at $\log T_c \sim 9.0$ and proceeds moderately. $\epsilon_{\rm n}$ peaks at this temperature. After that peak, $\epsilon_{\rm n}/\epsilon_\nu$ drops once and rises again to 1 at $\log T_c \sim 9.2$. This second peak corresponds to neon burning. Then $\epsilon_{\rm n}/\epsilon_\nu$ drops again and rises to 1 at $\log T_c \gtrsim 9.3$. This is oxygen burning. Contrary to the cases of VMSs, the rise and

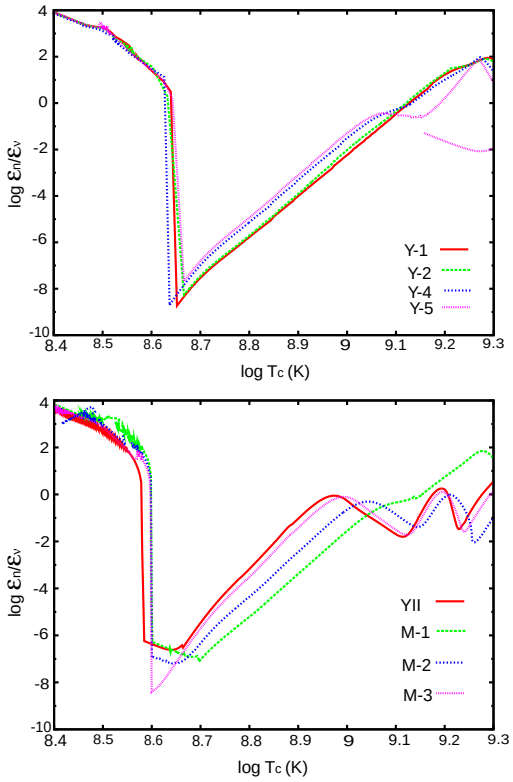

Figure 3.30 The ratio of $\epsilon_{\rm n}$ to neutrino cooling rate ϵ_ν at the center as a function of temperature. Top panel: for 'Y-series'. Bottom panel: for models YII and 'M-series'.

down tendency indicates that each burning process proceeds stably for lower mass models.

The later evolution after logT_c reaches 9.0 varies for each model. (1) Stars of CVMS mass range directly collapses due to pair instability and iron photodisintegration. (2) Lower VMS stars explode as a PISN. (3) Stars around $100M_\odot$ cause core oscillations. (4) Ordinary massive stars go through stable burning stages and finally collapse due to iron photodisintegration. We describe each case along with our models.

(1) CVMS case and (2) PISN case In Figure 3.31, snapshots of temperature (a), density (b), $\epsilon_{\rm n}$ (c), and Y_e (d), evolution of chemical composition at the center from the end of helium burning through the beginning of the core-collapse (e), and snapshots of chemical structure at four stages (f) - (i) are shown for model Y-1. Figure 3.32 is for model Y-2, Figure 3.33 for model Y-3, Figure 3.34 for model Y-4,

Figure 3.35 for model Y-5, and Figure 3.36 for model N-4, respectively. One can see from panels (a) and (b) that the inner CO core contracts and heats up separately whereas the outer He and H layers hardly changes. (one can see from panels (f) - (i) that the boundary between the contracting inner core and the outer regions corresponds to the outer edge of the CO rich layer). At the boundary the temperature and density gaps become larger and larger. As described in the previous paragraph, the inner CO core evolution accelerates rapidly, and so the outer layers cannot follow the inner core evolution. Seeing the inner part, the whole CO core evolves in the same time scale until iron core collapse occurs. For CVMS cases, the whole CO core is unstable due to pair creation.

Panels (c) shows the region where the energy is supplied by nuclear reactions. There are roughly three peaks of $\epsilon_{\rm n}$; $\epsilon_{\rm n}$ in the central region and two medium regions. In the central region, the main fuel changes from carbon to neon, magnesium , oxygen, and silicon as the core contracts and temperature rises. What is more, in the central region photodisintegration occurs and $\epsilon_{\rm n}$ can be even negative due to high temperature.

The first medium peak (the inner peak of the two medium peaks; for example, $M_r \sim 200 - 300 M_\odot$ for model Y-1) is due to the helium burning there. In this region, light α-elements (^{12}C, ^{16}O, ^{20}Ne, and ^{24}Mg) are main elements, but ^{4}He slightly remains. The temperature in this area increases along with the central temperature, and even exceeds 10^9K. Therefore the remaining helium burns and $\epsilon_{\rm n}$ increases dramatically. One can see form panels (e) -(i) that slightly remaining ^{4}He there is consumed. This peak moves outward as the remaining ^{4}He is consumed and temperature eventually rises.

The second medium peak (the outer peak of the two medium peaks; for example, $M_r \sim 380 M_\odot$ for model Y-1) is due to the hydrogen burning there. This corresponds to the region slightly out of the large gaps of temperature and density, and $\log T \sim 8.0 - 8.2$ there. This layer cannot follow the central evolution, and so temperature, density and $\epsilon_{\rm n}$ hardly change.

Panels in (d) show the Y_e structure. When $\log T$ exceeds 9, the electron capture begins and Y_e starts to deviate from 0.5. However, At these stages ($\log T \lesssim 9.6$), this change is very slight and electron emission also occurs, and so Y_e rises again for some models. Considerable electron capture begins after $\log T \gtrsim 9.7$ (and when the central region becomes dense).

Panels in (e) show the evolution of central chemical composition. One can see which element burns as fuel and which is produced as ash at each temperature. For VMS, temperature rises monotonically along with the evolution (without loop), and so $\log T_c$ can be adopted instead of time. These figures well explain the facts described above. After helium exhaustion ($\log T \lesssim 8.6$), carbon does not ignite until $\log T$ exceeds 9. This relates to the low C/O ratio and low central density of VMS. During this contraction phase, helium slightly remaining in the outer CO core supplies luminosity (the first medium peak of $\epsilon_{\rm n}$). For a $25 M_\odot$ star, carbon ignites at $\log T \lesssim 8.8$. This turning point at which carbon starts to decrease largely is different among models. For massive models (Y-1, 2, and 3), carbon starts to ignite considerably after $\log T$ exceeds 9.2, whereas for relatively less massive models (Y-4, and 5) this point shifts toward lower temperature, $\log T \sim 9.0$. Just after (or even at the same time as) carbon ignition, neon burning follows. Oxygen is the main element the latter half of central helium burning to the point, and carbon and neon ignitions even increases mass fraction of ^{16}O, and ^{24}Mg and ^{28}Si are also produced with about 10% in mass fraction (compare panels (g) and (h)). The central convective core size is small ($15-20\%$ of the CO core in mass).

For VMS, the central region is in pair instability, and it collapses. After neon exhaustion, magnesium or oxygen burning does not follow immediately. $\epsilon_{\rm n}$ turns negative and positive repeatedly. During this phase, carbon and neon burning extends outward, and in the medium region of the CO core carbon and neon are consumed.

At $\log T \sim 9.5$, magnesium and oxygen burning occurs successively, and heavier α-elements (^{28}Si, ^{32}S, ^{36}Ar, ^{40}Ca; ^{28}Si is the main product) are synthesized. When $\log T$ exceeds 9.6, silicon burning occurs, ^{56}Ni is mainly produced and the main element shifts to ^{54}Fe, a neutron rich nucleus at $\log T \sim 9.7$. At such high temperature, the electron capture occurs considerably and Y_e decreases. When $\log T$ exceeds 9.7, ^{56}Ni and ^{54}Fe are destroyed ^{4}He and proton by photodisintegration. The star enters the iron core-collapse phase to form a black hole. However, for model Y-5, the nuclear energy generation by oxygen and silicon burning exceeds gravitational binding energy, and the star turns from collapse to expansion at $\log T = 9.53$. The whole star explodes as a PISN.

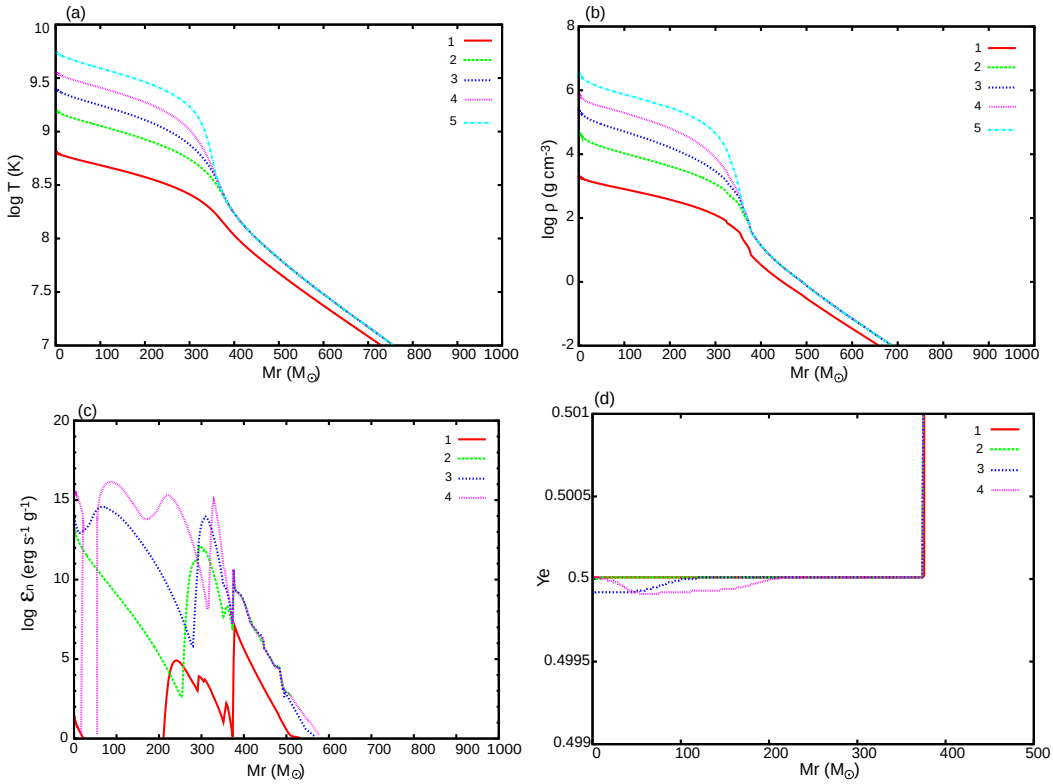

Figure 3.31 Snapshots of temperature (a), density (b), nuclear energy generation rate per unit mass (c), and Y_e (d) in later evolutionary stages after helium exhaustion for model Y-1. Five snapshots are plotted in (a) and (b), four are plotted in (c) and (d). Numbers attached to each line means the order of the evolution. 1: During contraction after helium burning ($\log T_c = 8.8$). 2: Just before carbon burning ($\log T_c = 9.2$). 3: After carbon exhaustion. 4. After oxygen exhaustion. 5: At the beginning of iron core-collapse.

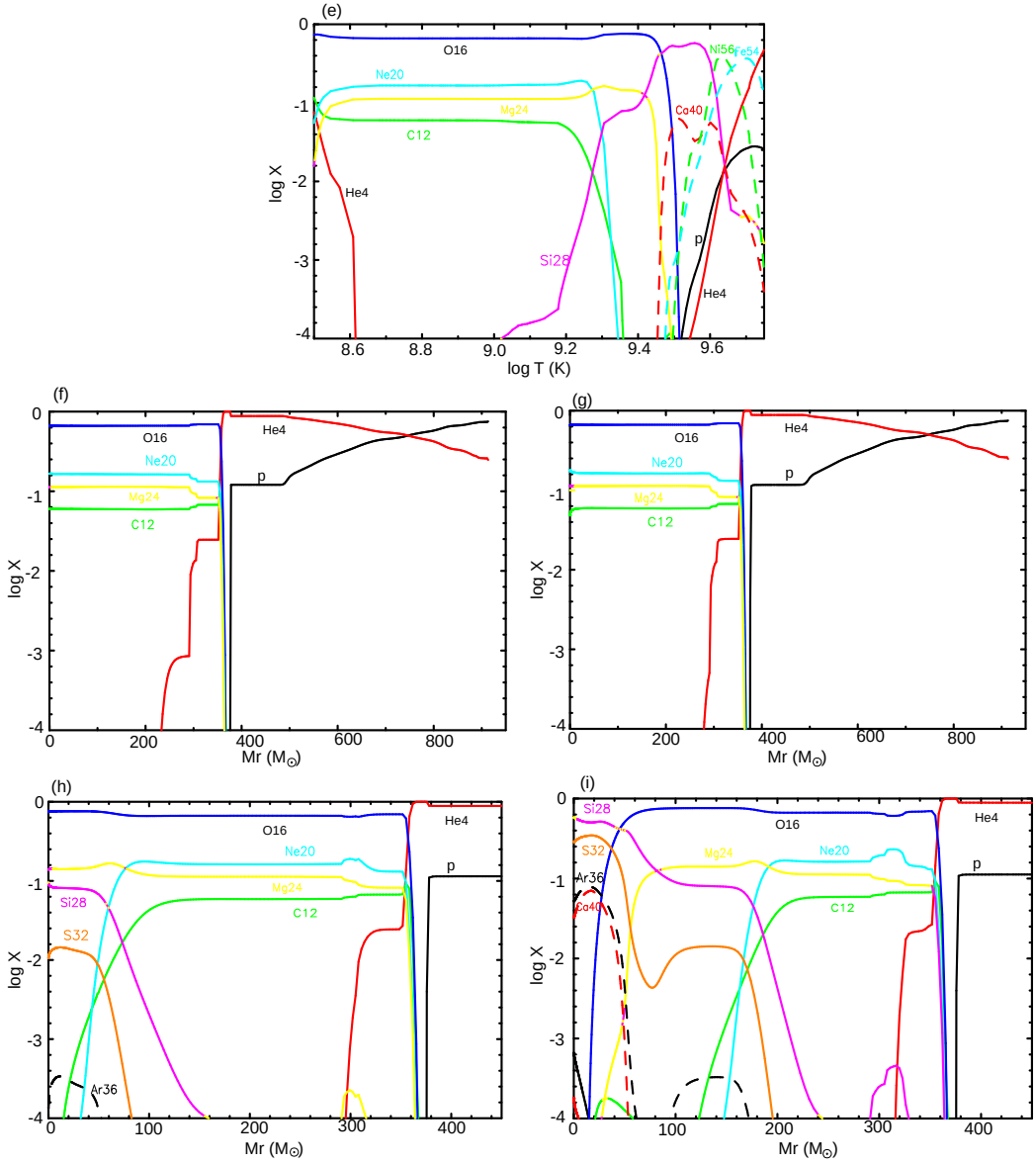

Figure 3.31 Figure 3.31 - continued. (e): Evolution of central chemical composition as a function of logT_c. (f)-(i): Snapshots of chemical composition. Composition of (f) corresponds to 1 in Figure 3.31, (g) to 2, (h) to 3, and (i) to 4, respectively. For panels (h) and (i), only the inner part (CO core) is shown.

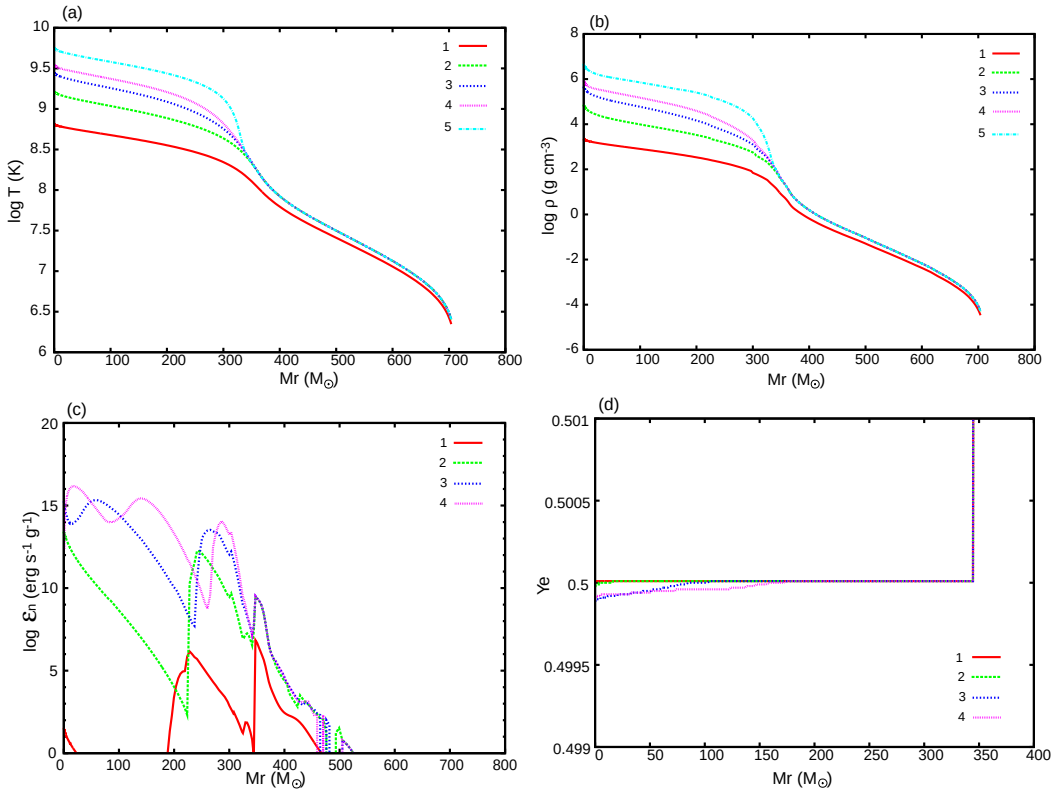

Figure 3.32 Same as Figure 3.31, but for model Y-2.

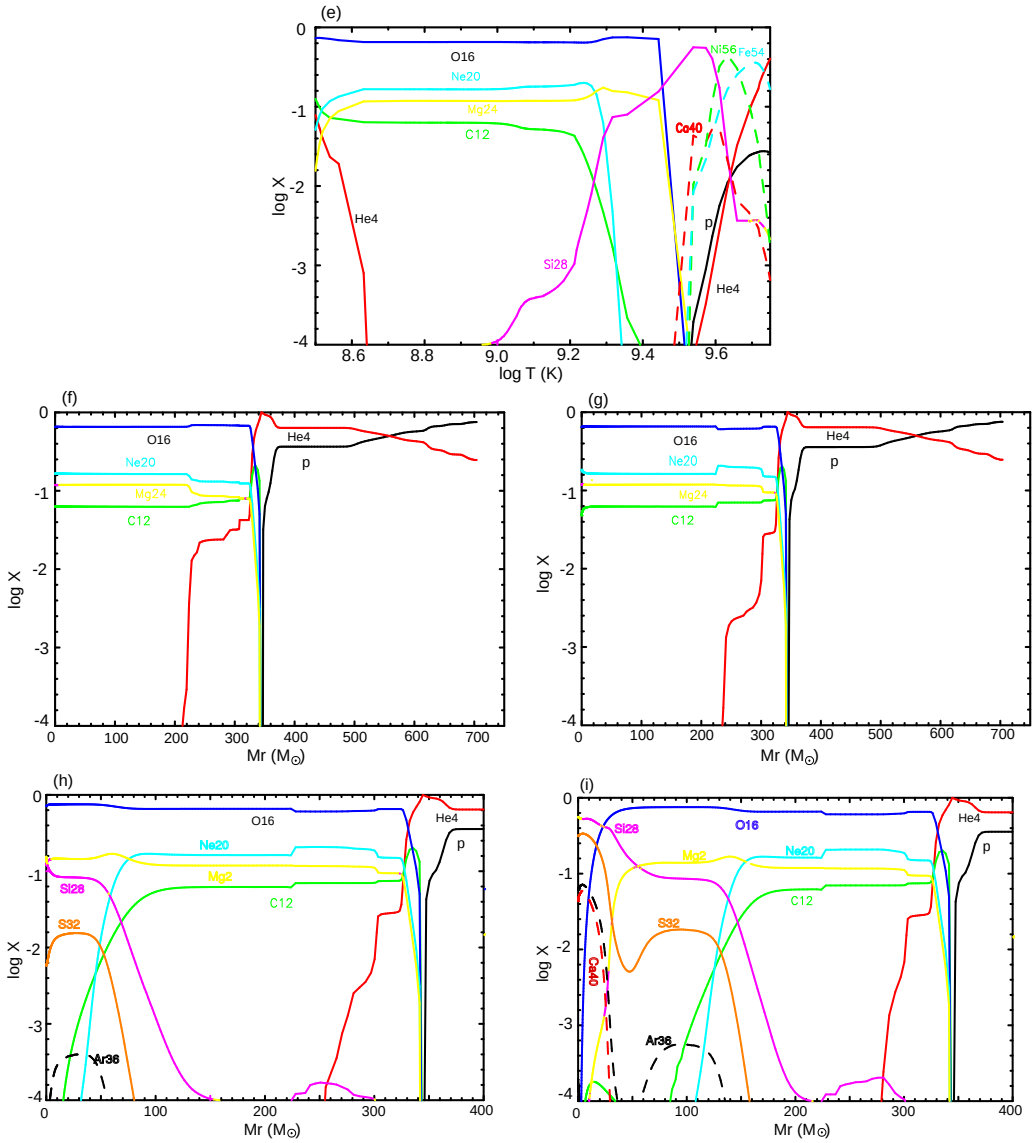

Figure 3.32 Figure 3.32 - continued.

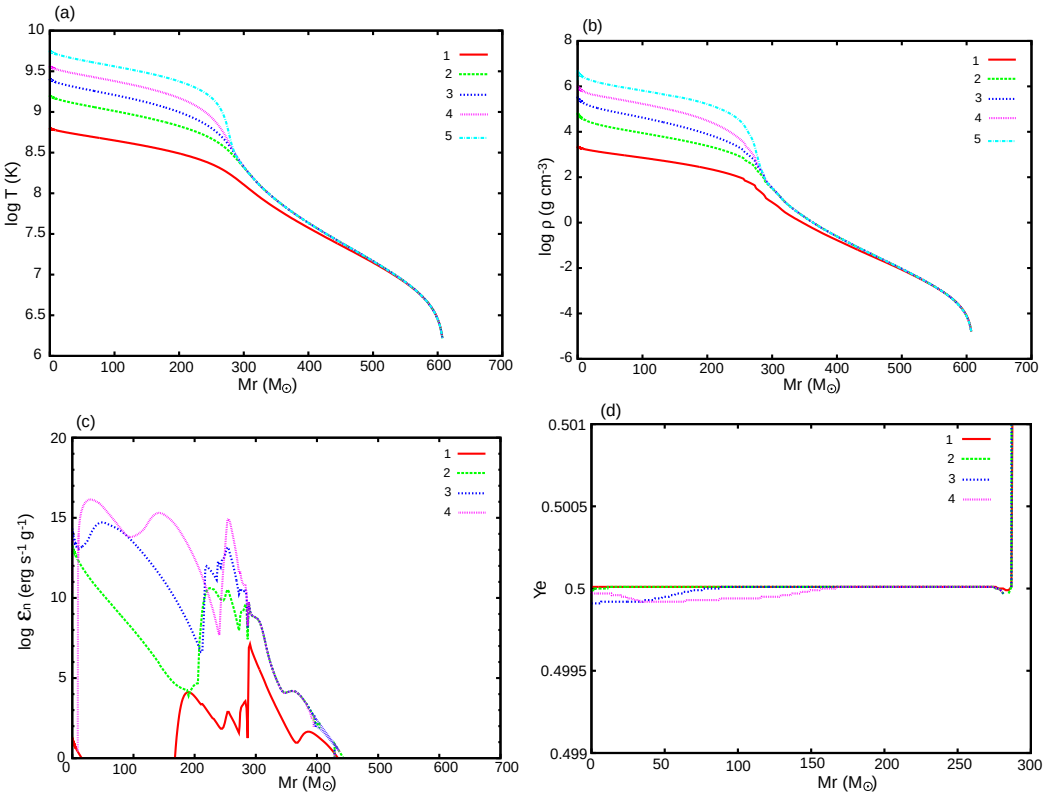

Figure 3.33 Same as Figure 3.31, but for model Y-3.

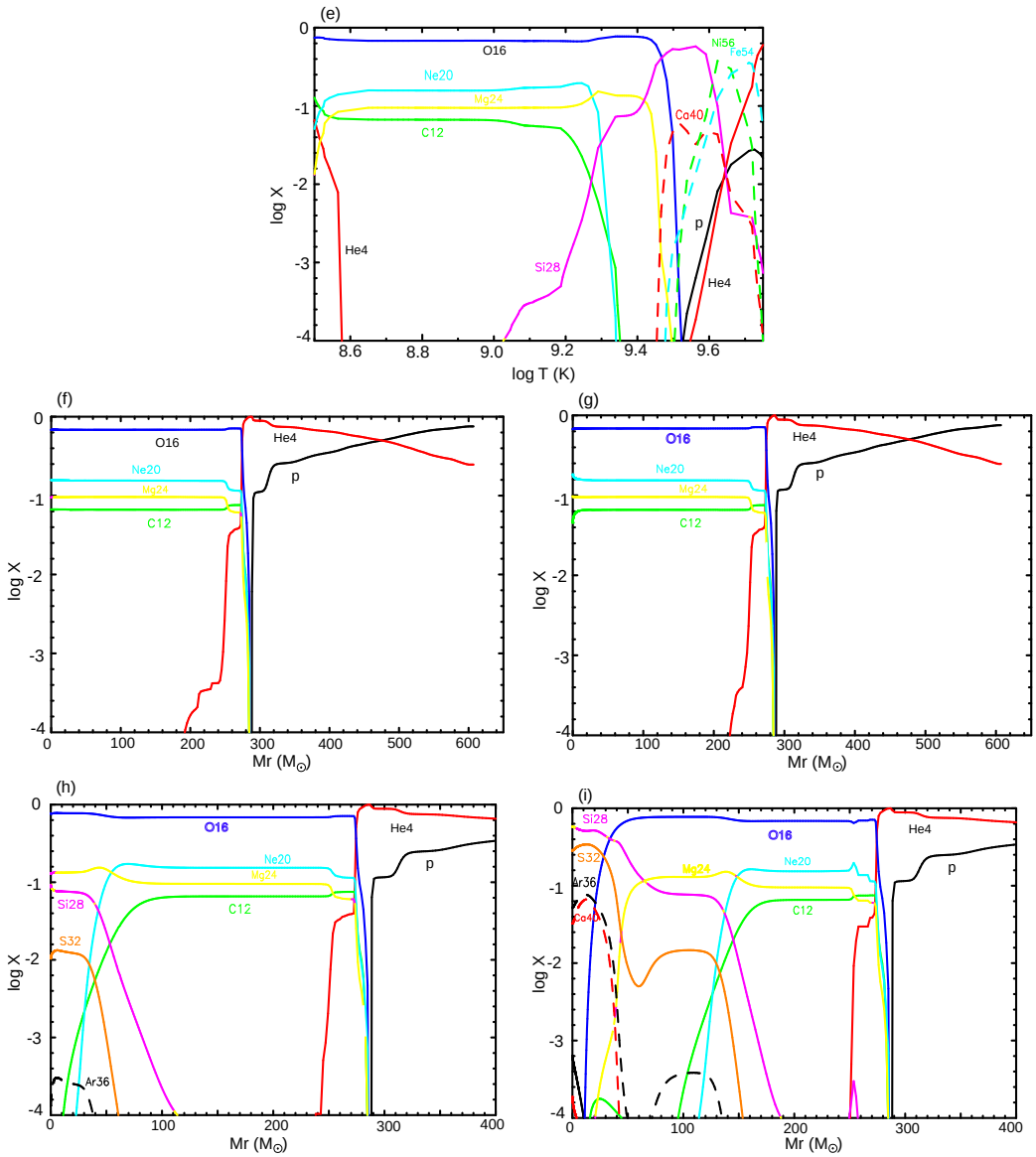

Figure 3.33 Figure 3.33 - continued.

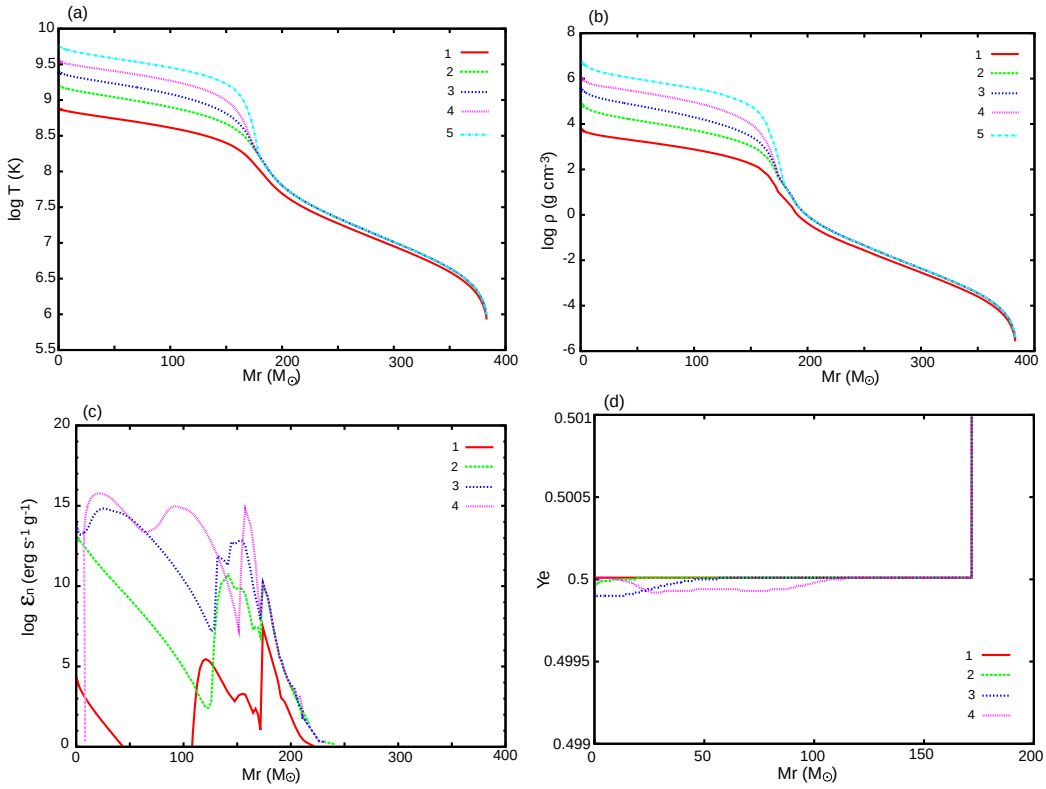

Figure 3.34 Same as Figure 3.31, but for model Y-4.

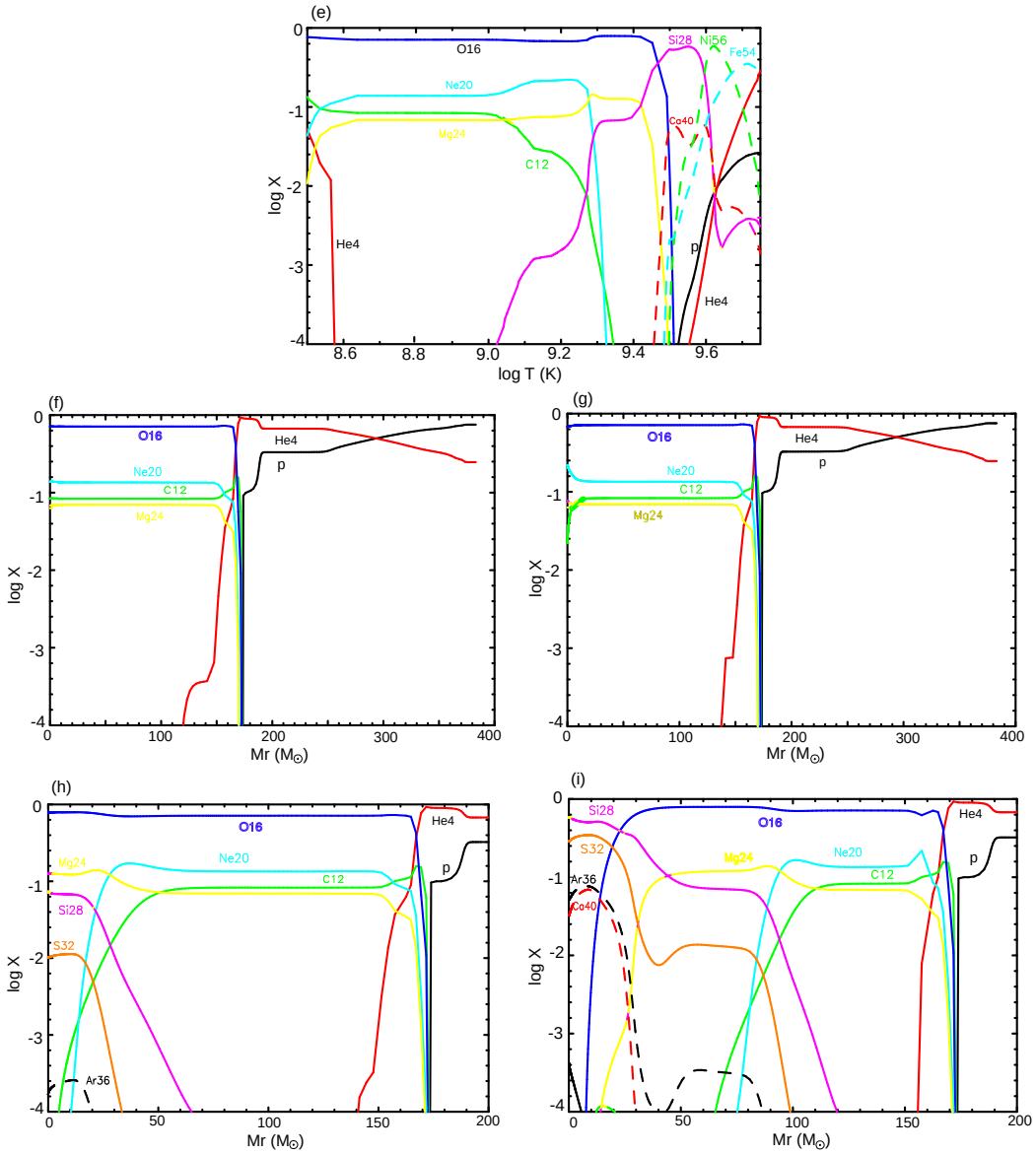

Figure 3.34 Figure 3.34 - continued.

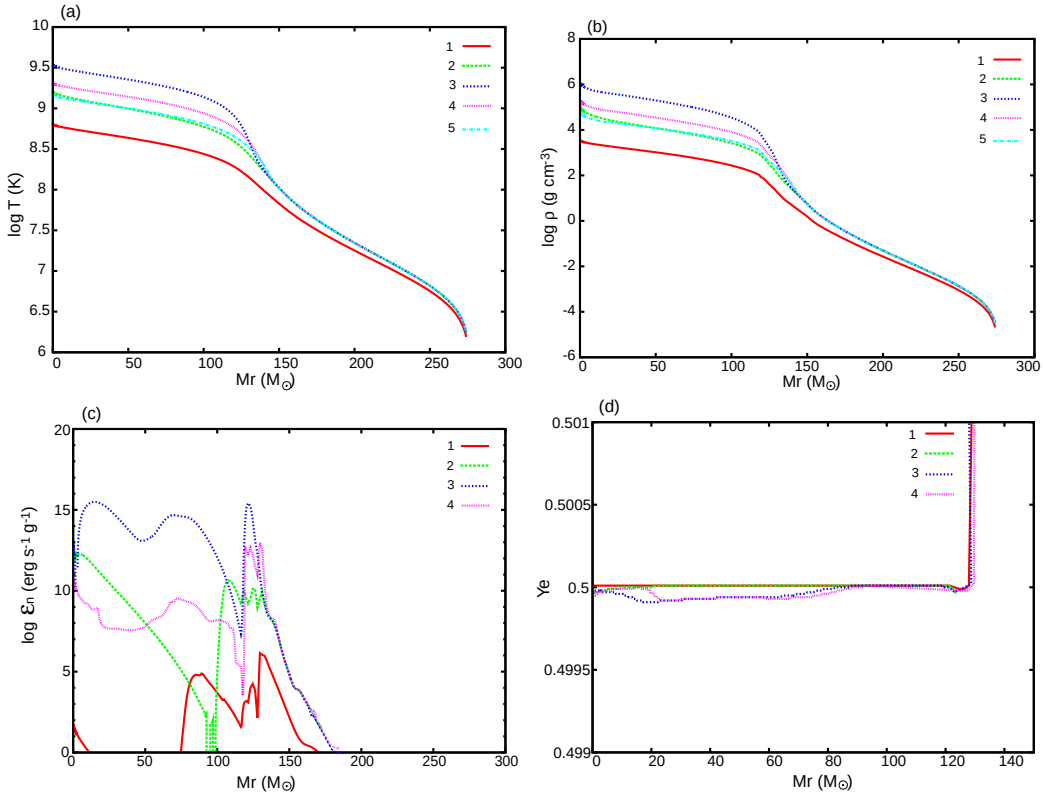

Figure 3.35 Same as Figure 3.31, but for model Y-5. The star ends up as a PSIN, so snapshots with attached number 4 and 5 show those though expansion. The line with number 4 is when $\log T_c = 9.3$, and The line with number 5 is when $\log T_c = 9.15$.

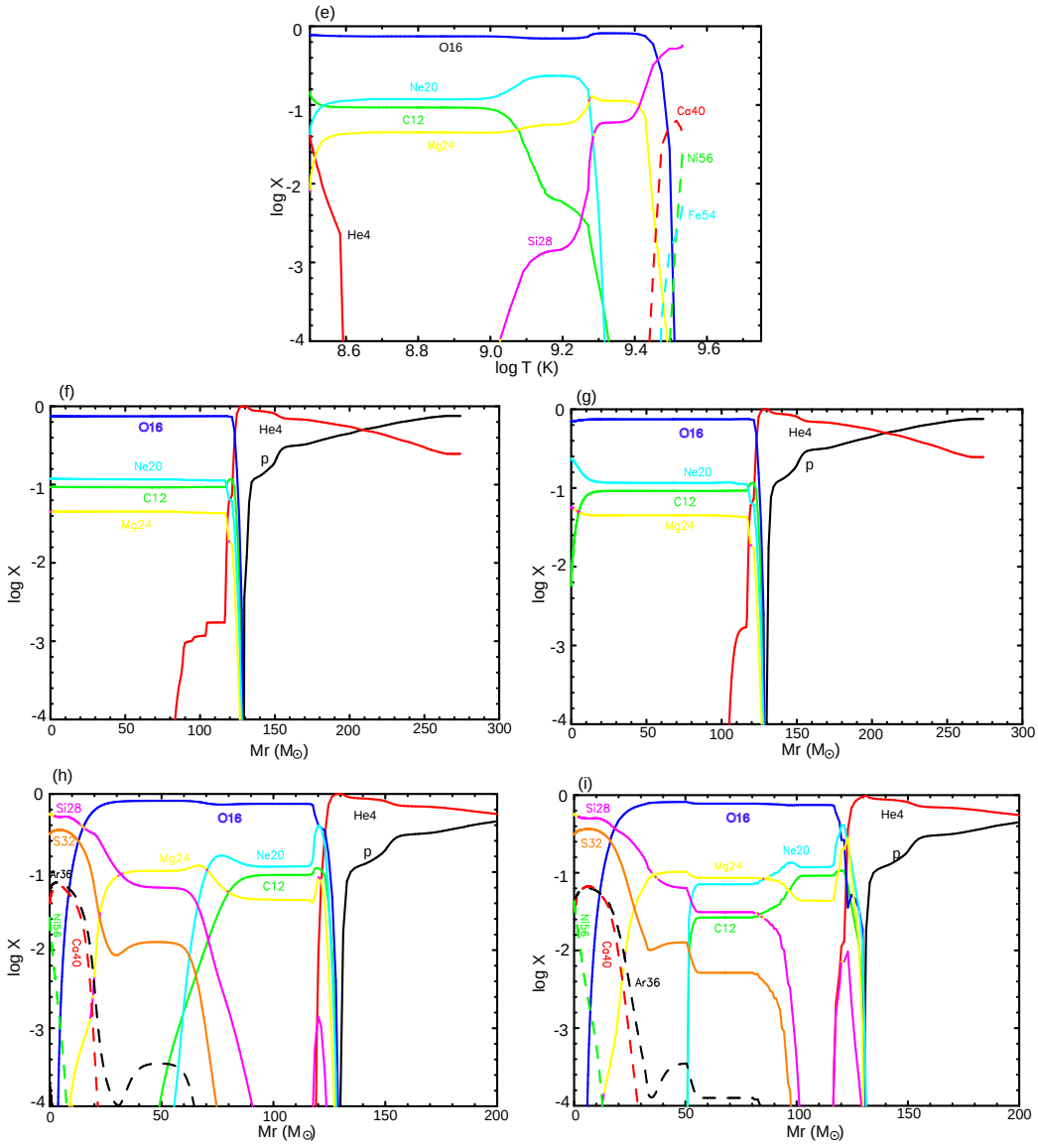

Figure 3.35 Figure 3.35 - continued. The star ends up as a PSIN, so temperature turns to decrease at $\log T_c = 9.53$. Therefore, panel (d) is the chemical composition at $\log T_c = 9.53$, and panel (e) is that at $\log T_c = 9.15$ after expansion.

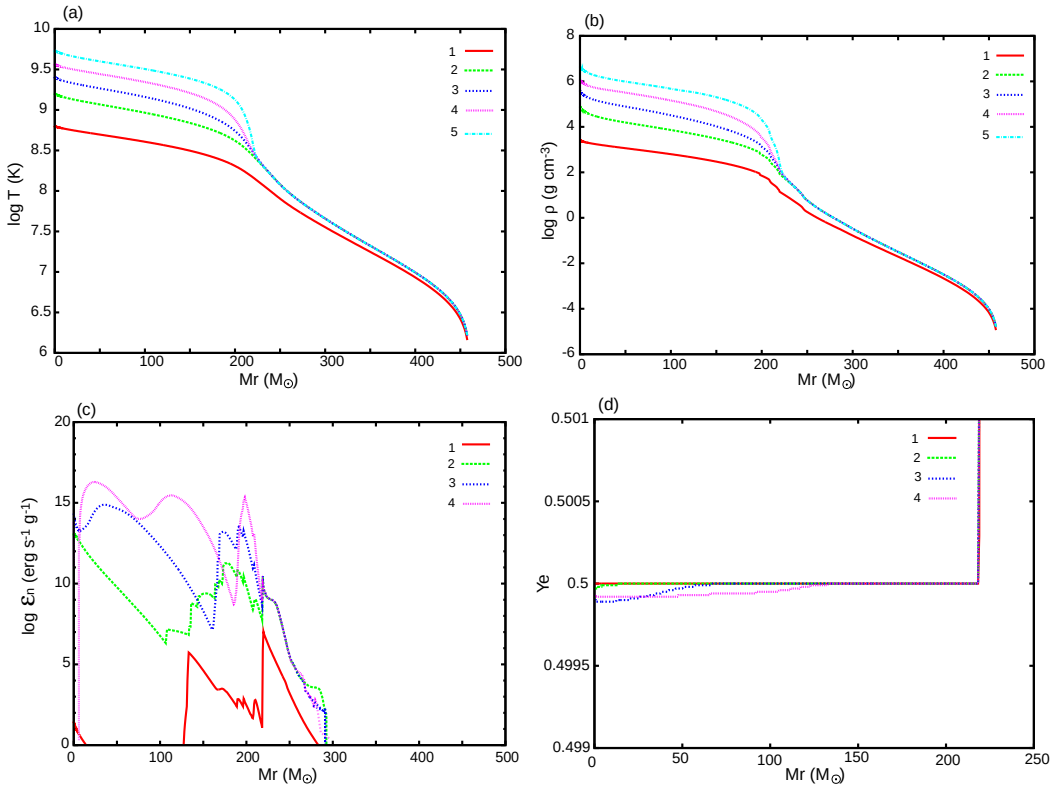

Figure 3.36 Same as Figure 3.31, but for model N-4.

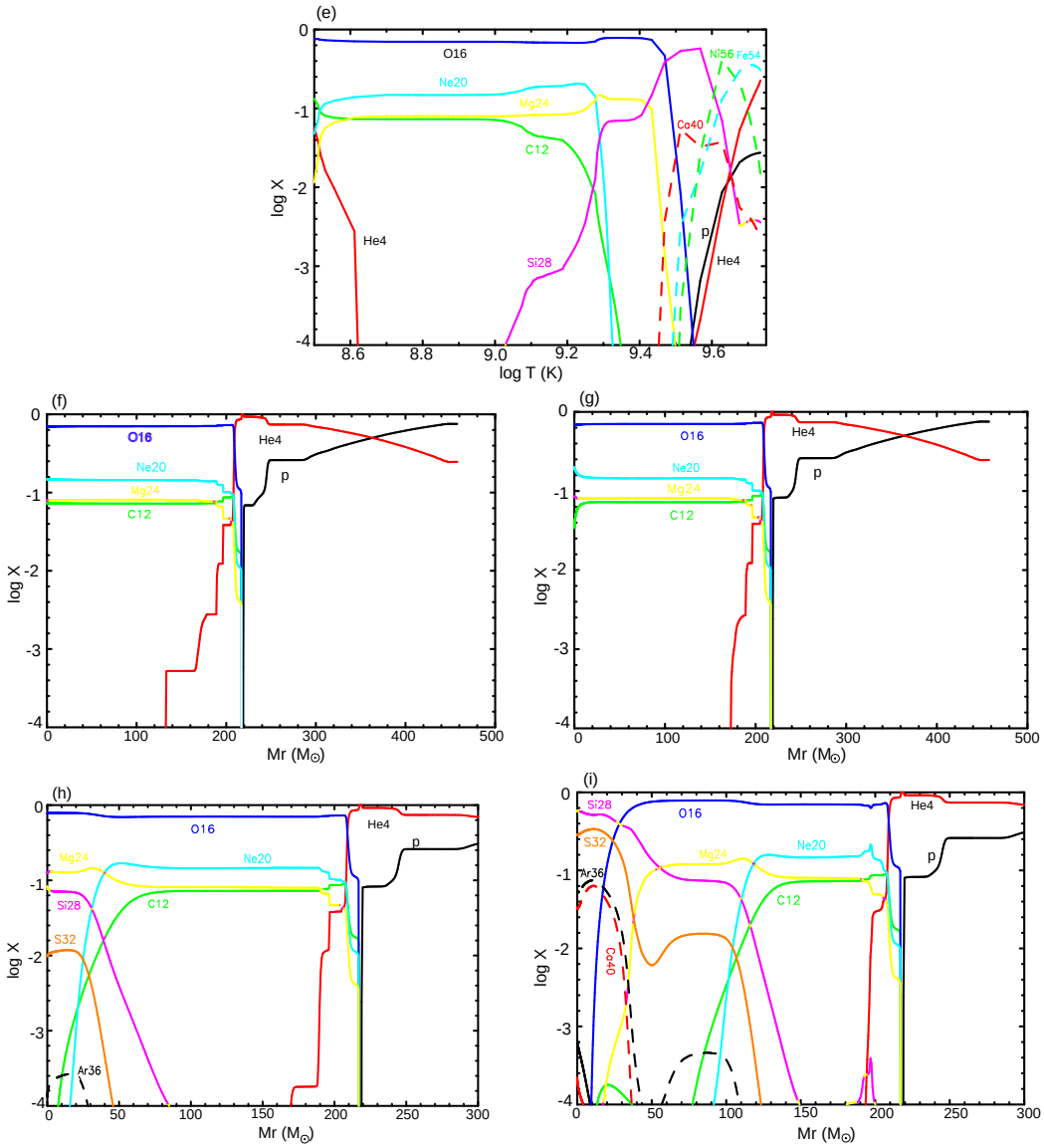

Figure 3.36 Figure 3.36 - continued.

(3) Core oscillation star case Stars with a little less massive than PISN mass range induce CO core oscillation during oxygen and silicon burning. In this research, model M-2 corresponds. The star finally collapses to form a black hole, but the oscillation prolong the evolution timescale of these burning stages. Here we describe several features characteristics of this phenomenon.

Figure 3.37 (a)-(e) show the evolution of the center for model M-2. The final mass of this star is $135M_{\odot}$ and CO core mass is $\sim 60M_{\odot}$. It does not explode as a PISN, but core oscillates six times and finally collapses. The oscillation is gradually amplified and the central temperature lowers from $\log T_c \sim 9.4 - 9.7$ to $\sim 8.8 - 9.1$ (panel (a)). The evolution timescale becomes longer when the core expands. This makes a clear contrast between the central temperature and the evolution timescale length in panel (a). When the core shrinks (near the peak in the central temperature, it evolves fast (in the order of $10^3 - 10^4$s). When the core expands (near the bottom in the central temperature, it evolves slowly ($0.01 - 100$ yr). The driving force of such oscillations is nuclear burning, mainly oxygen and silicon burning. $\epsilon_{\rm n}$ becomes very high when the temperature is near the peak (panel (b)). One can see what is burning at the center by comparing panels (b) and (c). Carbon and Neon burn at the first peak. One can see from panel (c) that ^{12}C and ^{20}Ne abundances drop drastically at the first peak. Oxygen is mainly burning at the second, third, and fourth peaks. Silicon is mainly burning at the fifth and sixth peaks. At the fourth, fifth, and sixth peaks $\epsilon_{\rm n}$ sometimes becomes negative due to disintegration.

One notable point in panel (d) is that the central Y_e drops largely around the fifth bottom. This is due to the decay of ^{56}Ni. At the fifth peak, ^{28}Si burns and ^{56}Ni is produced in large quantities. It takes 0.5 year for the expanding core to shrink again, and so this period is enough for ^{56}Ni to decay to ^{56}Fe. One can see form panel (c) that dominant nucleus shift from ^{56}Ni to ^{56}Fe at the fifth bottom. The large drop in Y_e after the sixth bottom is due to electron capture. After the sixth bottom, the iron core can not produce enough energy to expand, and it collapses.

Figure 3.37 (e) and (f) show snapshots of temperature and density as a function of M_r, respectively. These snapshots are at the fifth peak, fifth bottom, and sixth peak. One can see that the whole CO core oscillates together. This is because the evolutionary timescale is long.

Figure 3.37 (g) and (h) show snapshots of $\epsilon_{\rm n}$ as a function of M_r at each peak. 1st through 4th peaks are plotted in panel (g), and 4th through 6th peak are in panel

(h). The attached element is the place where this fuel is burning. Figure 3.37 (i) through (o) is chemical composition inner than CO core at several points. One can see where and what fuel are burning. For example, (1) Oxygen is mainly burning at the center at the second peak. In fact, Comparing panel (j) (chemical composition at first bottom) and panel (k) (at second bottom), oxygen decreases at the center. This indicates that oxygen has burned between the first and second bottom, i.e., during the first peak. (2) At the fifth peak, silicon is burning at the center and oxygen is burning around $M_r \sim 7-8M_\odot$. Actually Comparing panel (m) (chemical composition at fourth bottom) and panel (n) (at fifth bottom), silicon decreases at the center and oxygen decreases around $M_r \sim 7 - 8M_\odot$.

One can see that each burning region moves outward from panel (g) and (h). Oxygen burns most at center at the center at the second peak, but $M_r \sim 2M_\odot$ at the third peak, $M_r \sim 4M_\odot$ at the fourth peak, $M_r \sim 7 - 8M_\odot$ at the fifth peak, and $M_r \sim 13 - 15M_\odot$ at the sixth peak. Silicon burning region behaves similarly. Especially at the fourth peak, oxygen shell burning rather than center is the main driving force for core expansion. Along with oxygen and silicon burning, carbon and neon shell burning proceed around $M_r \sim 15 - 40M_\odot$. One can see that ^{12}C and ^{20}Ne decrease gradually from panels (i) through (o) in this region. In panel (o) (at sixth bottom), the oscillation time is so long that there is sufficient time for convection to mix materials in $M_r \sim 18 - 55M_\odot$ completely. Therefore, the chemical composition in this area are uniform.

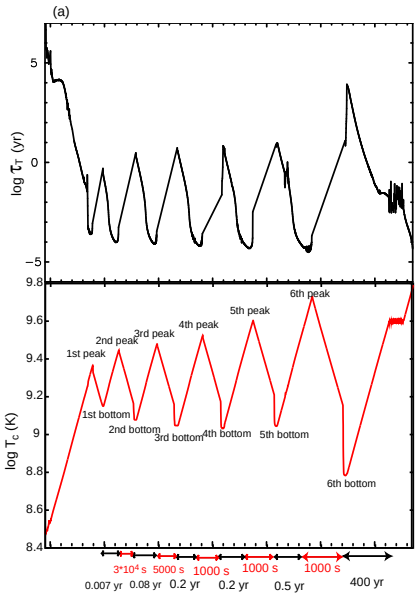

Figure 3.37 (a) Evolutionary timescale of the central temperature $\tau_T = T/\dot{T}$ (upper panel) along with the central temperature evolution (lower panel) for model M-2.

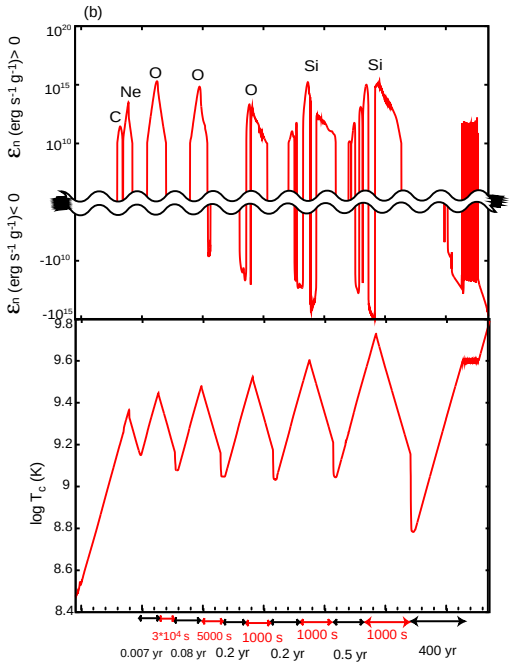

Figure 3.37 Figure 3.37 - continued. (b) Evolution of nuclear energy generation rate ϵ_n at the center (upper panel) along with the central temperature evolution (lower panel). ϵ_n is potted in log scale distinguishing the sign. Small energy generation or absorption ($\mid \epsilon_n \mid < 10^5$) is omitted. The element attached to each peak in upper panel means what is mainly burning and the main source of energy generation.

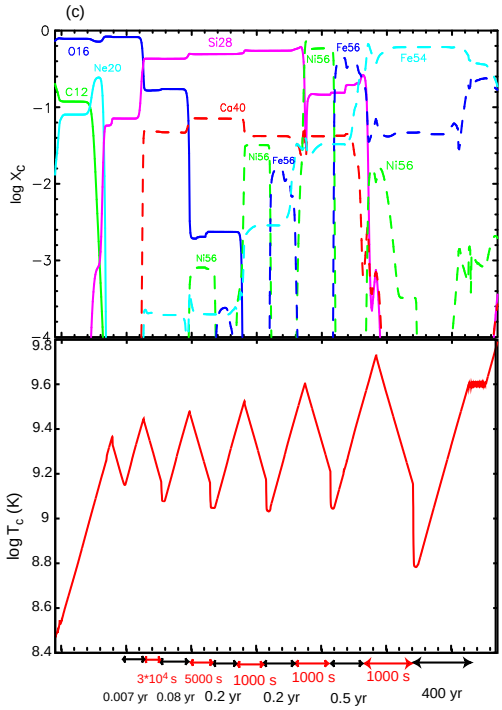

Figure 3.37 Figure 3.37 - continued. (c) Evolution of chemical composition at the center (upper panel) along with the central temperature evolution (lower panel).

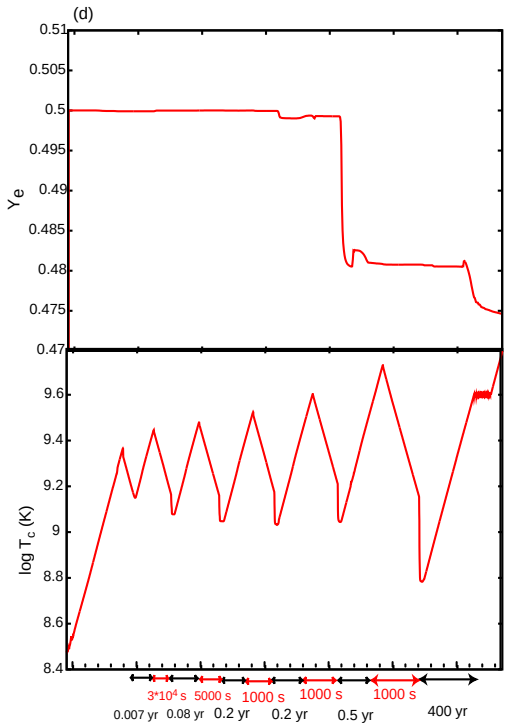

Figure 3.37 Figure 3.37 - continued. (d) Evolution of central Y_e (upper panel) along with the central temperature evolution (lower panel).

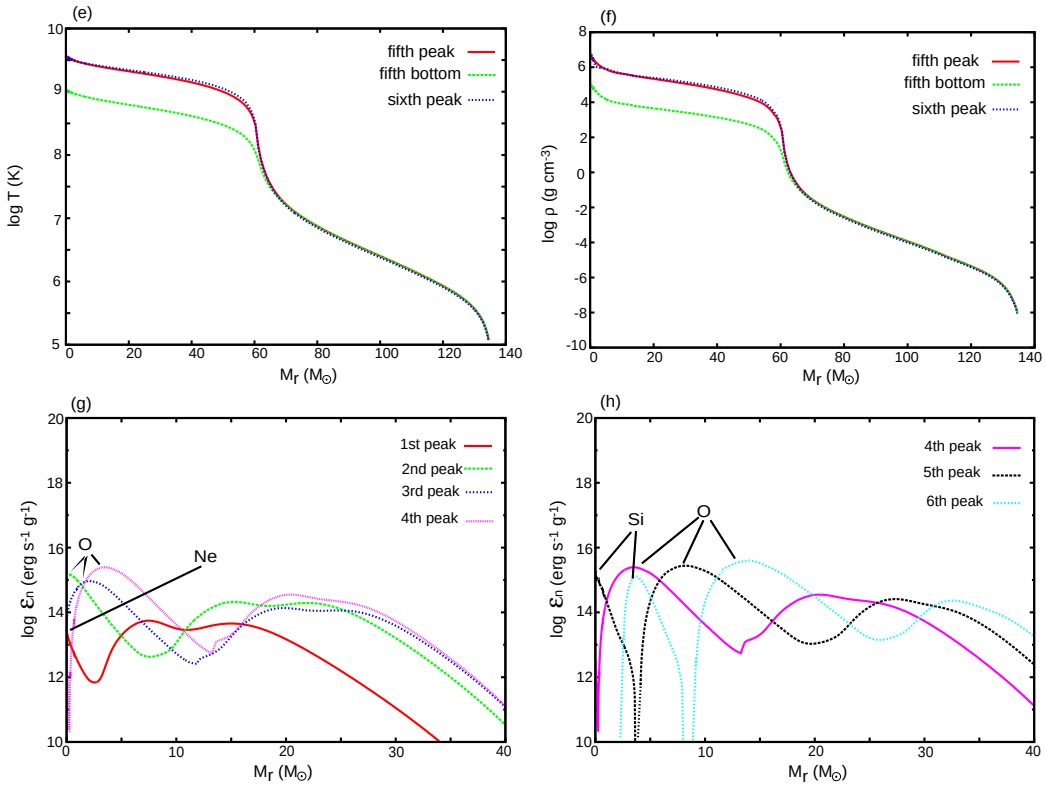

Figure 3.37 Figure 3.37 - continued. Snapshots of Snapshots of temperature (e), and density (f) at the fifth peak, fifth bottom, sixth peak in the central temperature. (g) and (h): Snapshots of nuclear energy generation rate per unit mass. Plots in panel (g) are when the first, second, third, and fourth peak in the central temperature. Plots in panel (h) are when the fourth, fifth, and sixth peak in the central temperature.

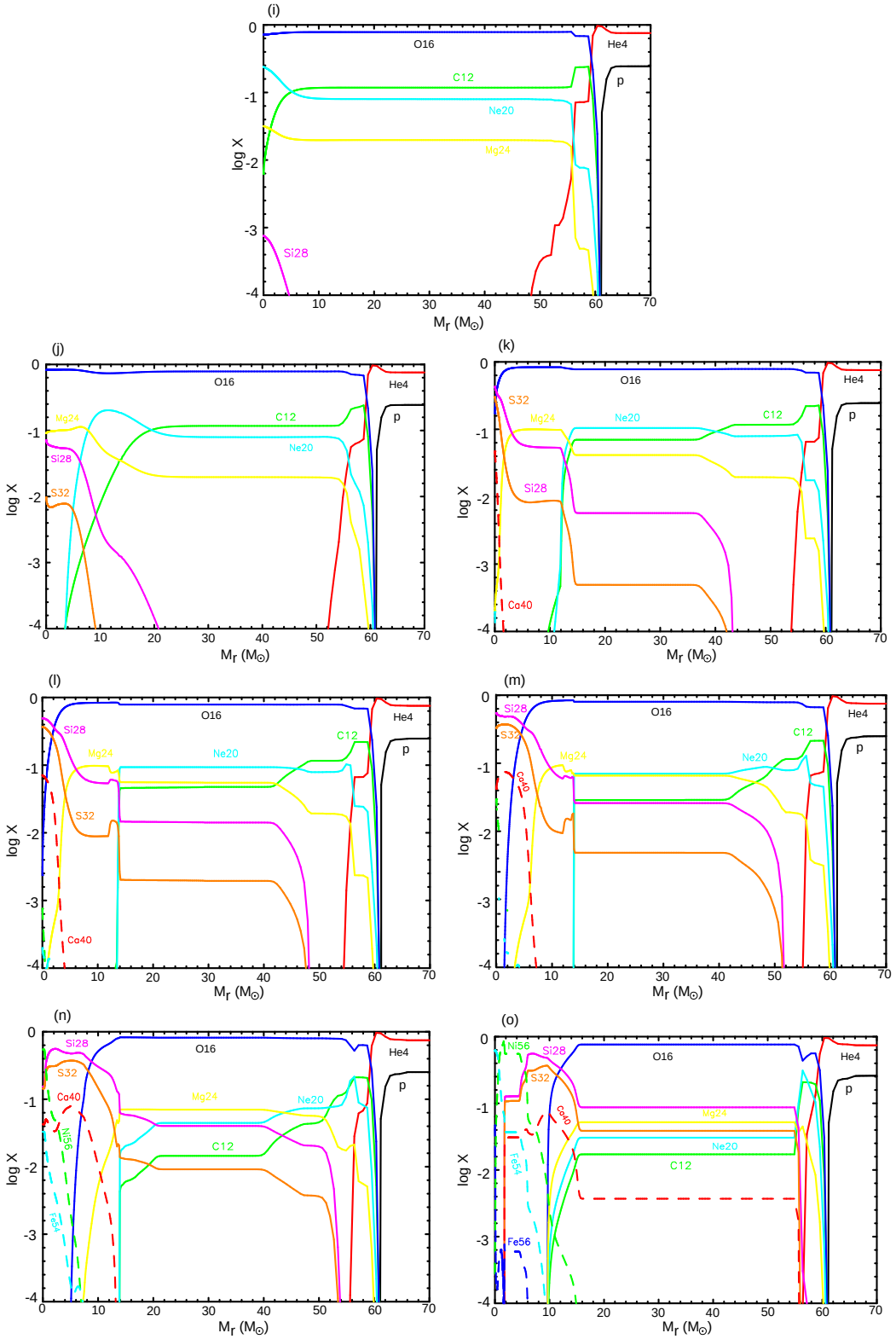

Figure 3.37 Figure 3.37 - continued. Snapshots of chemical composition when (i) logT_c reaches 9.1 for the first time (before core oscillation), (j) the first bottom in the central temperature, (k) the second bottom, (l) the third bottom, (m) the fourth bottom, (n) the fifth bottom, and (o) the sixth bottom.

Core oscillation star case — other models We perform two other models to investigate the characteristics in core oscillation: $85M_{\odot}$ (model N-1), and $115M_{\odot}$ (model N'-1 hereafter). These stars are less massive than model M-2, and so there are some quantative difference. Less massive stars undergo core oscillation more times with smaller amplitude, shorter period. (panel (a) in Figure 3.38 and Figure 3.39). For model N-1 the CO core oscillates dozens of times, and for model N'-1 the core does one dozen times. Oscillation occurs mainly at silicon burning stage (only two of dozens of times at oxygen burning) for model N-1, whereas oscillation occurs many times at both oxygen and silicon burning for model N'-1 (panels (b) and (c)). At silicon burning stage, burning (silicon burns and iron group elements such as ^{56}Ni and ^{54}Fe are produced) and photodisintegration (iron group elements are destroyed and go back to ^{28}Si) occur alternatively. Y_e decreases gradually through oscillations (panel (d)). This is mainly due to electron capture process of ^{56}Ni to ^{56}Fe. Panels (e) - (h) show snapshots of chemical structure at four stages. Similarly to model M-2, main energy source is shell oxygen and silicon burnings during later oscillations.

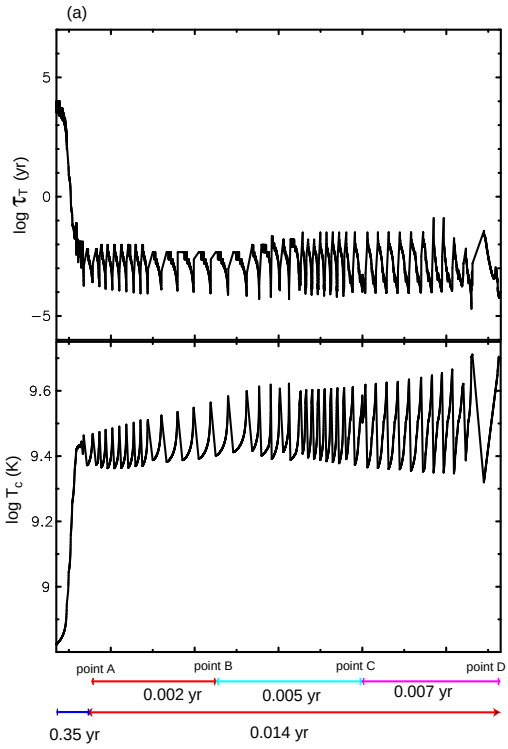

Figure 3.38 (a) Evolutionary timescale of the central temperature $\tau_T = T/\dot{T}$ (upper panel) along with the central temperature evolution (lower panel) for model N-1.

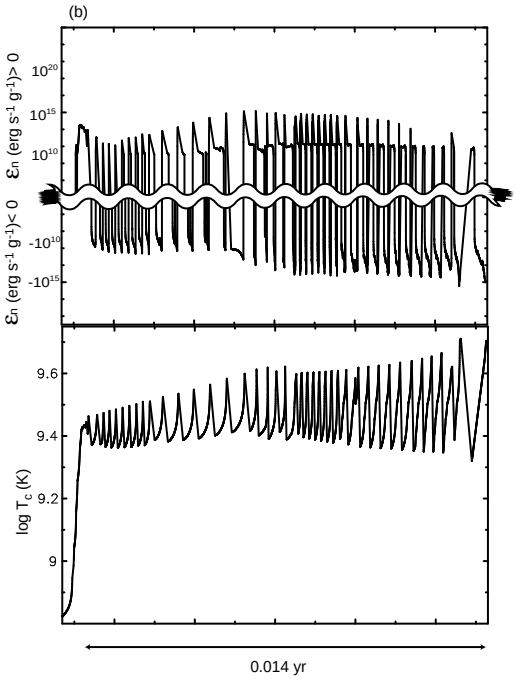

Figure 3.38 Figure 3.38 - continued. (b) Evolution of nuclear energy generation rate $\epsilon_{\rm n}$ at the center (upper panel) along with the central temperature evolution (lower panel). $\epsilon_{\rm n}$ is potted in log scale distinguishing the sign. Small energy generation or absorption ($\mid \epsilon_{\rm n} \mid < 10^5$) is omitted. The element attached to each peak in upper panel means what is mainly burning and the main source of energy generation.

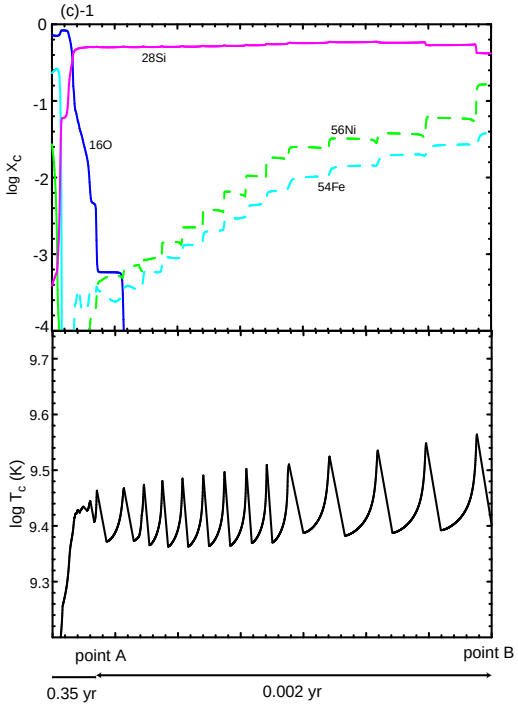

Figure 3.38 Figure 3.38 - continued. (c)-1 Evolution of chemical composition at the center (upper panel) along with the central temperature evolution (lower panel). The period 0.002 yr from point A through point B in panel (a) are shown.

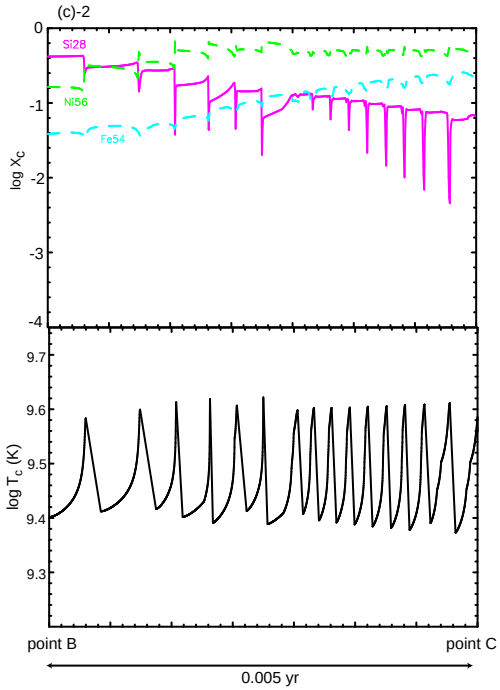

Figure 3.38 Figure 3.38 - continued. (c)-2 Evolution of chemical composition at the center (upper panel) along with the central temperature evolution (lower panel). The period 0.005 yr from point B through point C in panel (a) are shown.

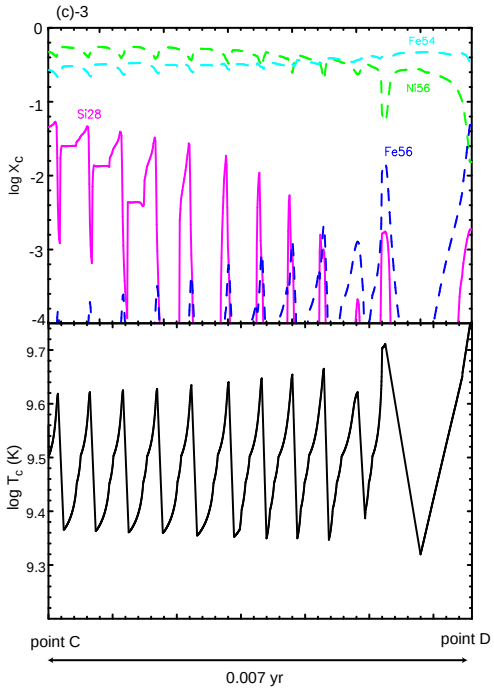

Figure 3.38 Figure 3.38 - continued. (c)-3 Evolution of chemical composition at the center (upper panel) along with the central temperature evolution (lower panel). The period 0.007 yr from point C through point D in panel (a) are shown.

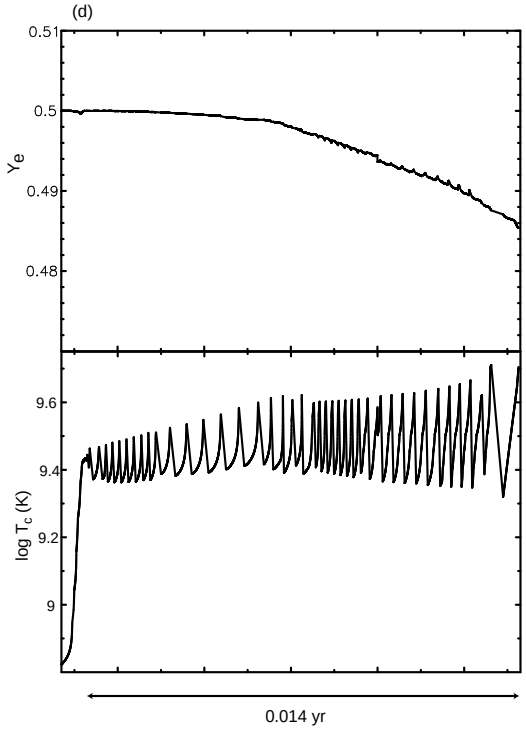

Figure 3.38 Figure 3.38 - continued. (d) Evolution of central Y_e (upper panel) along with the central temperature evolution (lower panel).

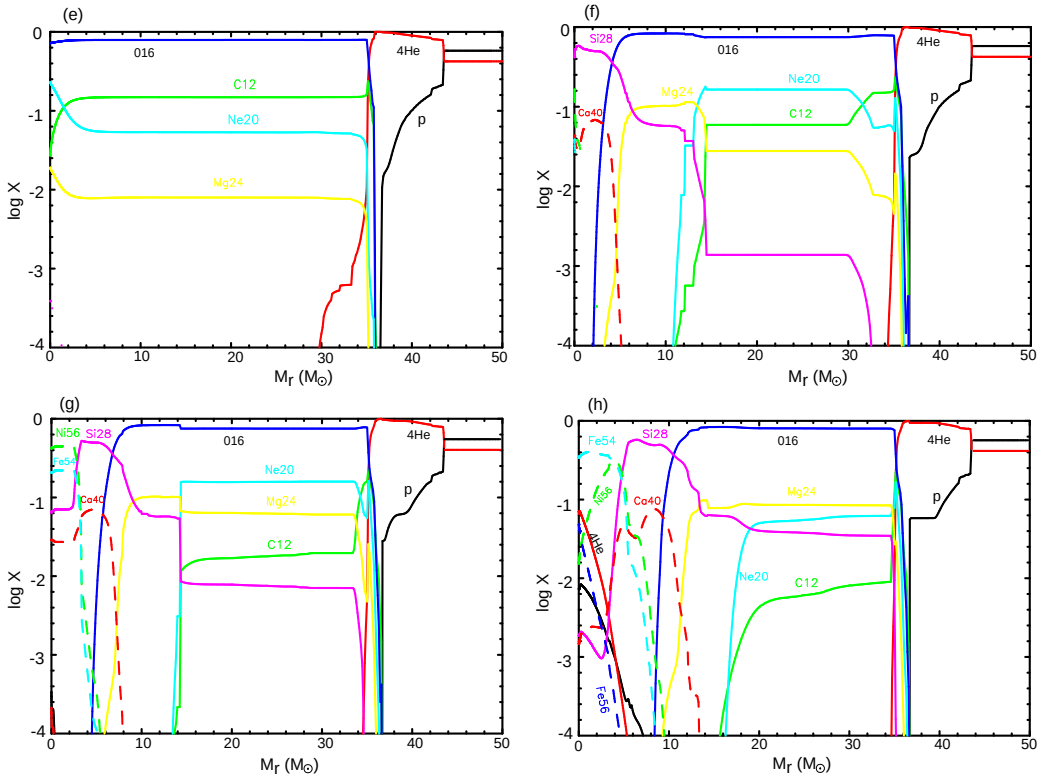

Figure 3.38 Figure 3.38 - continued. Snapshots of chemical composition at (e) point A ($\log T_c = 9.05$, $\log \rho_c = 4.9$), (f) point B ($\log T_c = 9.40$, $\log \rho_c = 6.4$), (g) point C ($\log T_c = 9.58$, $\log \rho_c = 6.6$), and (h) point D ($\log T_c = 9.77$, $\log \rho_c = 7.5$).

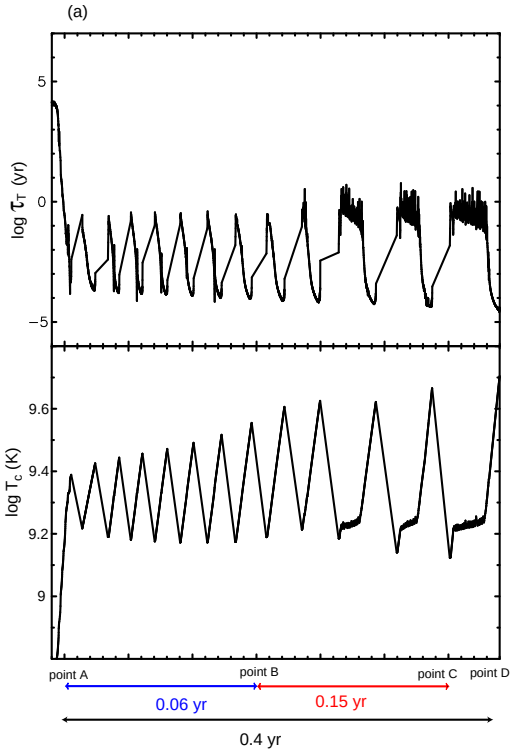

Figure 3.39 (a) Evolutionary timescale of the central temperature $\tau_T = T/\dot{T}$ (upper panel) along with the central temperature evolution (lower panel) for model N'-1.

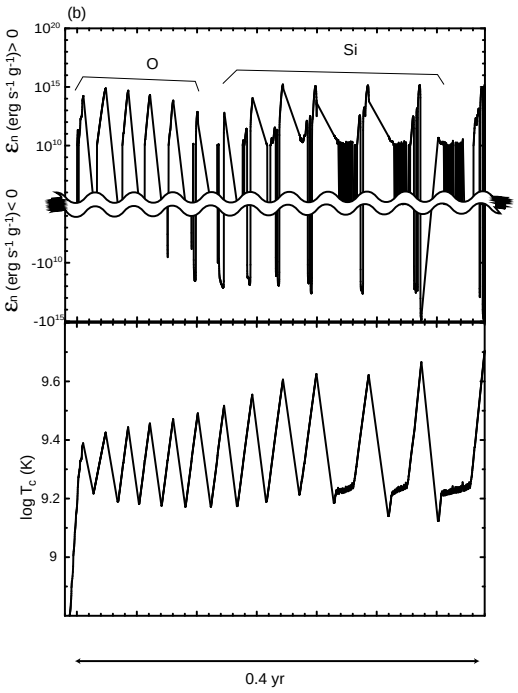

Figure 3.39 Figure 3.39 - continued. (b) Evolution of nuclear energy generation rate ϵ_n at the center (upper panel) along with the central temperature evolution (lower panel). ϵ_n is potted in log scale distinguishing the sign. Small energy generation or absorption ($\mid \epsilon_n \mid < 10^5$) is omitted. The element attached to each peak in upper panel means what is mainly burning and the main source of energy generation.

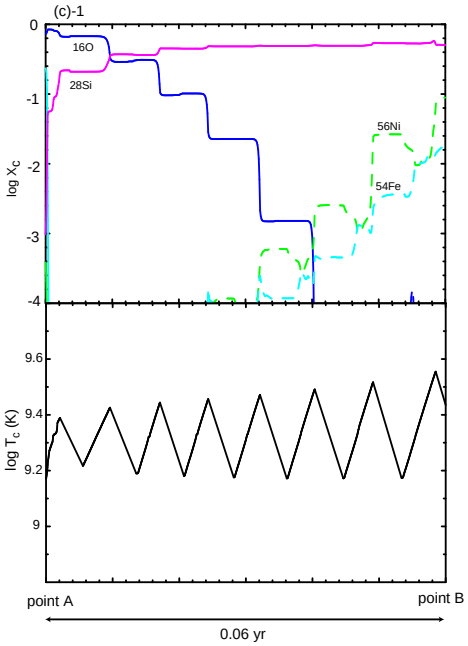

Figure 3.39 Figure 3.39 - continued. (c)-1 Evolution of chemical composition at the center (upper panel) along with the central temperature evolution (lower panel). The period 0.06 yr from point A through point B in panel (a) are shown.

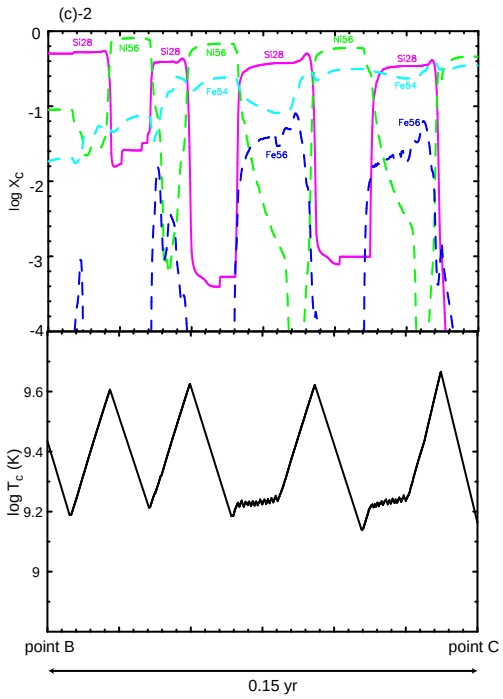

Figure 3.39 Figure 3.39 - continued. (c)-2 Evolution of chemical composition at the center (upper panel) along with the central temperature evolution (lower panel). The period 0.15 yr from point B through point C in panel (a) are shown.

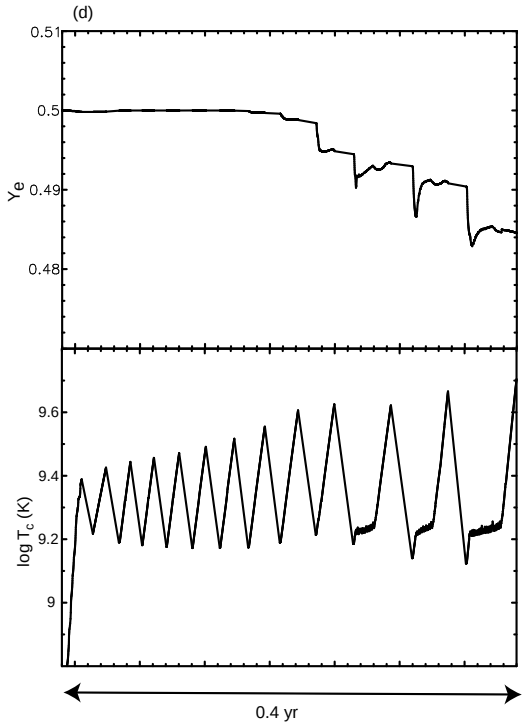

Figure 3.39 Figure 3.39 - continued. (d) Evolution of central Y_e (upper panel) along with the central temperature evolution (lower panel).

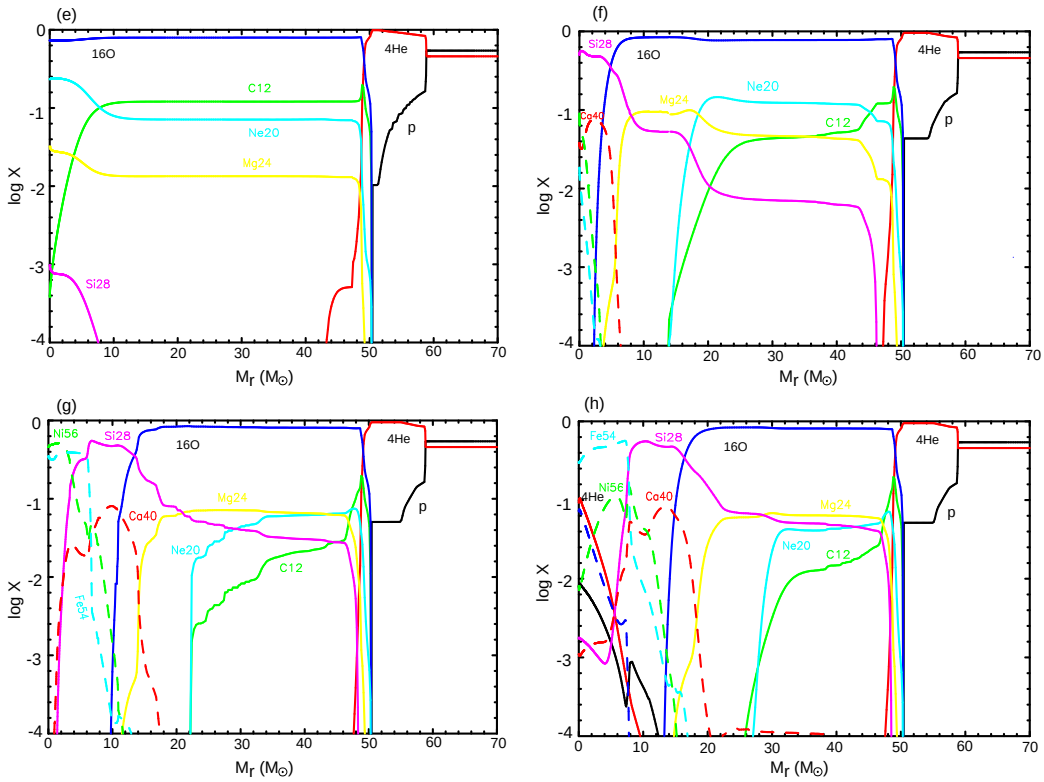

Figure 3.39 Figure 3.39 - continued. Snapshots of chemical composition at (e) point A ($\log T_c = 9.17$, $\log \rho_c = 5.3$), (f) point B ($\log T_c = 9.43$, $\log \rho_c = 6.4$), (g) point C ($\log T_c = 9.15$, $\log \rho_c = 5.3$), and (h) point D ($\log T_c = 9.75$, $\log \rho_c = 7.3$).

(4) Ordinary massive star case Models YII ($40M_\odot$) and M-3 ($57M_\odot$) is in ordinary massive star range ($10M_\odot \lesssim M \lesssim 60M_\odot$). The two models we performed in this research belong to the upper class of this mass range. The central temperature rises monotonically whereas lower stars such as $25M_\odot$ draws loops in the $\rho - T$ plane (see Figure 3.5). The monotonous evolution in central temperature is same as the case for VMSs, but each burning (carbon, neon, oxygen, and silicon burnings) occurs stably. This makes some features such as evolutionary timescale, core size different from those for VMS case.

Figure 3.40 and Figure 3.41 show snapshots and evolution after central He exhaustion. The formats in these panels are same as for CVMS figures. We describe evolutionary features for these two models comparing with CVMS cases. Seeing panels (a) and (b), one can notice that very central part ($M_r \lesssim 5M_\odot$) tends to evolve (i.e. rising in temperature and density) more rapidly than outer CO core region ($5-15M_\odot$ for model YII, and $5-30M_\odot$ for model M-3, respectively). This tendency becomes apparent during Si burning (line 4 in panels (a) and (b)) and the beginning of iron photodisintegration (line 5). This central part corresponds to Si core. As described above, the whole CO core evolves in the same timescale for CVMSs cases. This reflects the difference whether evolution proceeds stably or unstably. For ordinary massive stars cases, evolution proceeds stably and evolutionary timescale gradually shortens as temperature rises. Therefore, the Si core evolves more rapidly than the outer CO layer.

Panel (c) shows energy generation rate per unit mass due to nuclear reactions. The peak values are $10^{12} - 10^{14}\mathrm{erg\,s^{-1}\,g^{-1}}$ for O and Si burning. These values are much less than for CVMSs cases, more than $10^{15}\mathrm{erg\,s^{-1}\,g^{-1}}$. This also reflects the fact that each burning occurs stably.

Panel (d) shows Y_e snapshots. Y_e changes greatly than CVMSs cases. Density is higher for the same temperature (i.e. entropy is lower) for ordinary massive stars cases, and so electron capture or emission occurs more easily.

Panel (e) shows evolution of central chemical composition as a function of the central temperature, and (f) - (i) show snapshots of chemical composition as a function of mass coordinate. C burning starts (C decreases drastically in panel (e)) at $\log T_c \sim 9.0$, Ne burning at $\log T_c \sim 9.2$, O burning at $\log T_c \sim 9.35$, and Si burning at $\log T_c \sim 9.6$. These burning proceeds stably (ϵ_{n} and ϵ_ν balances; see Figure 3.30). The Si core is smaller to the whole mass, compared with CVMS cases. This relates to the

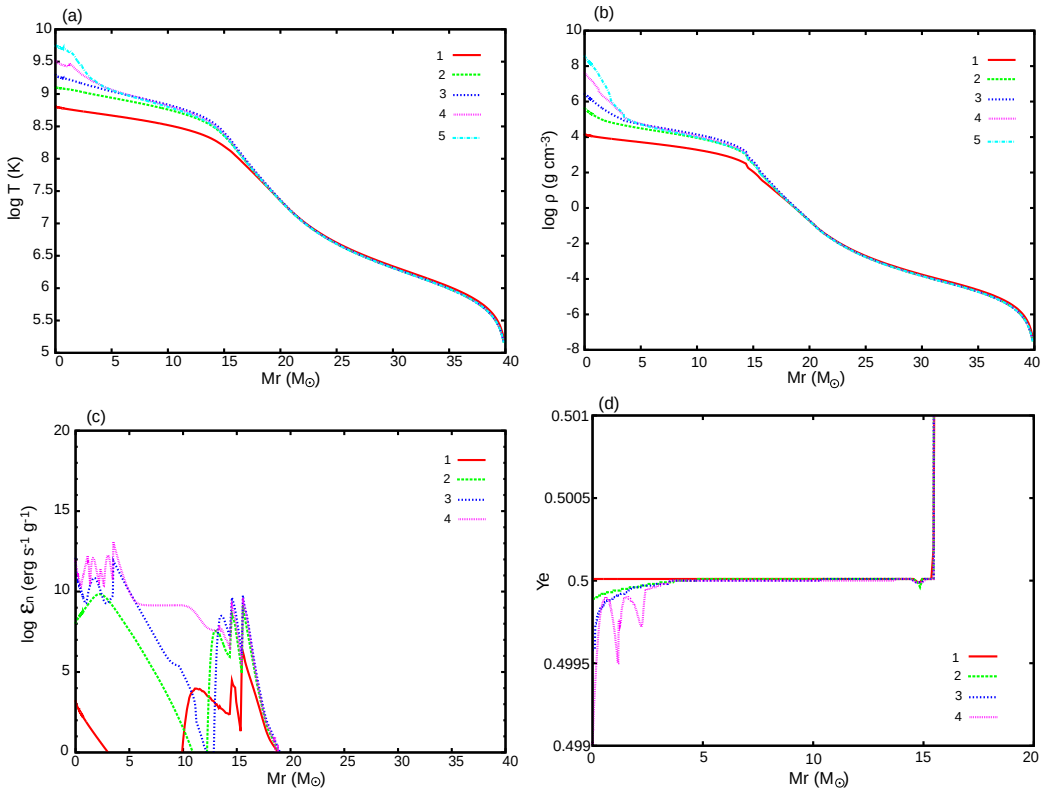

Figure 3.40 Same as Figure 3.31, but for model YII. The line with number 1 is when $\log T_c = 8.8$, The line with number 2 is when $\log T_c = 9.1$, The line with number 3 is when $\log T_c = 9.3$, The line with number 4 is when $\log T_c = 9.5$, and The line with number 5 is when $\log T_c = 9.75$.

evolutionary timescale discussed above (temperature and density increase).

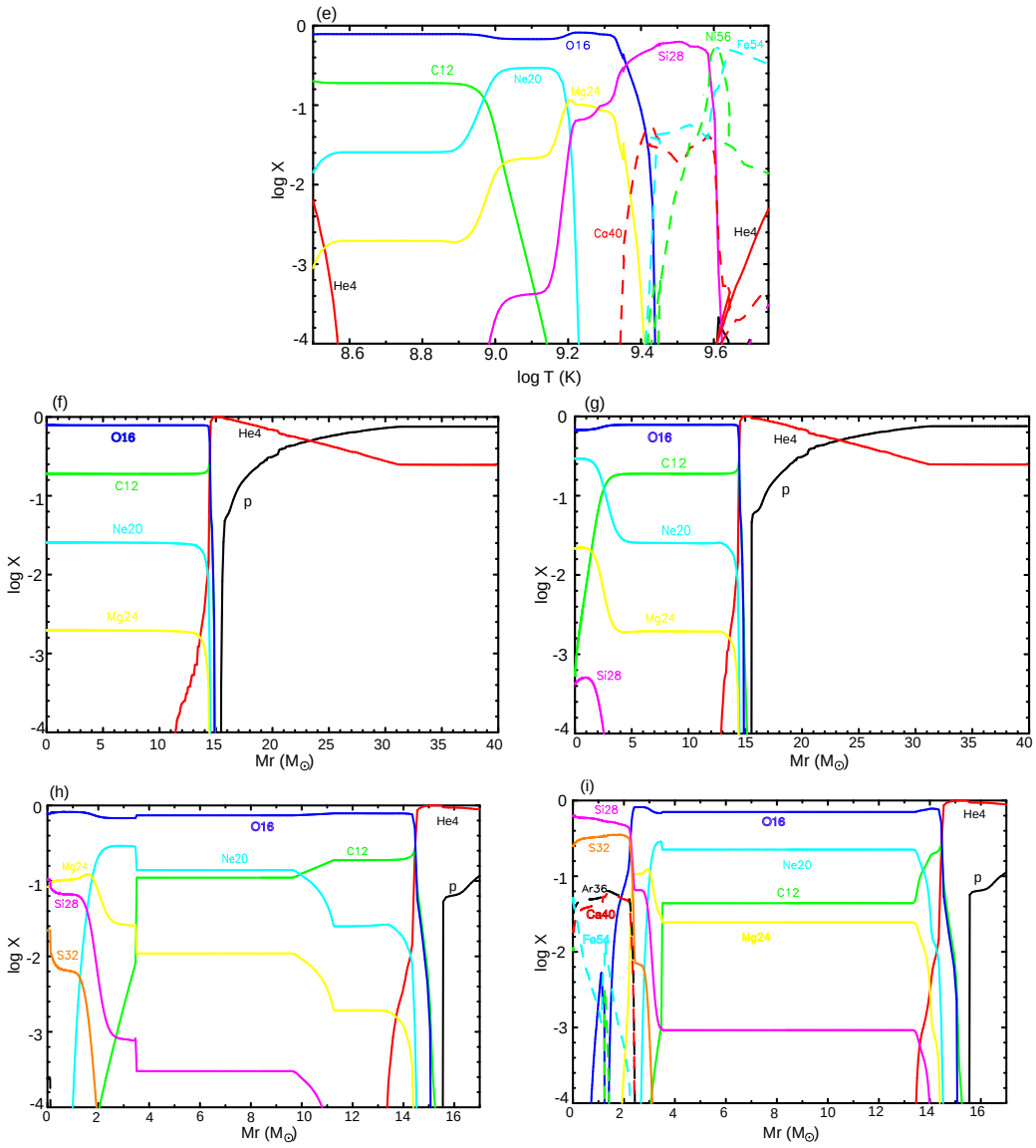

Figure 3.40 Figure 3.40 - continued. (e): Evolution of central chemical composition as a function of logT_c. (f)-(i): Snapshots of chemical composition. Composition of (f) corresponds to 1 in Figure 3.40, (g) to 2, (h) to 3, and (i) to 4, respectively. For panels (h) and (i), only the inner part (CO core) is shown.

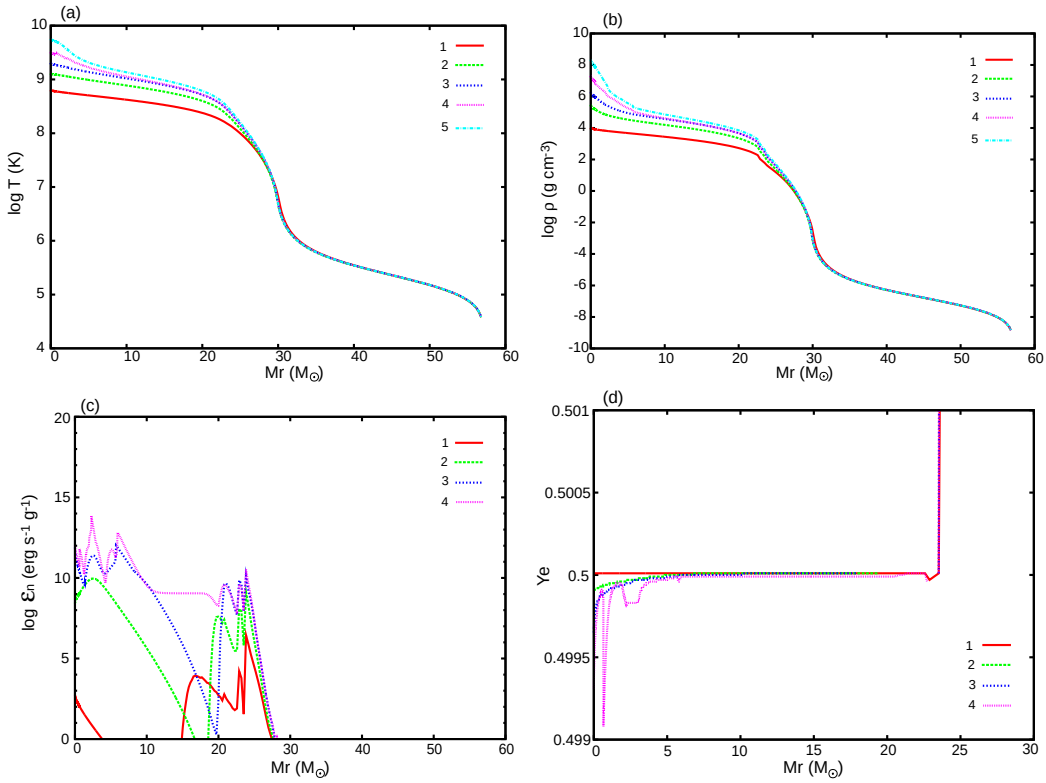

Figure 3.41 Same as Figure 3.40, but for model M-3.

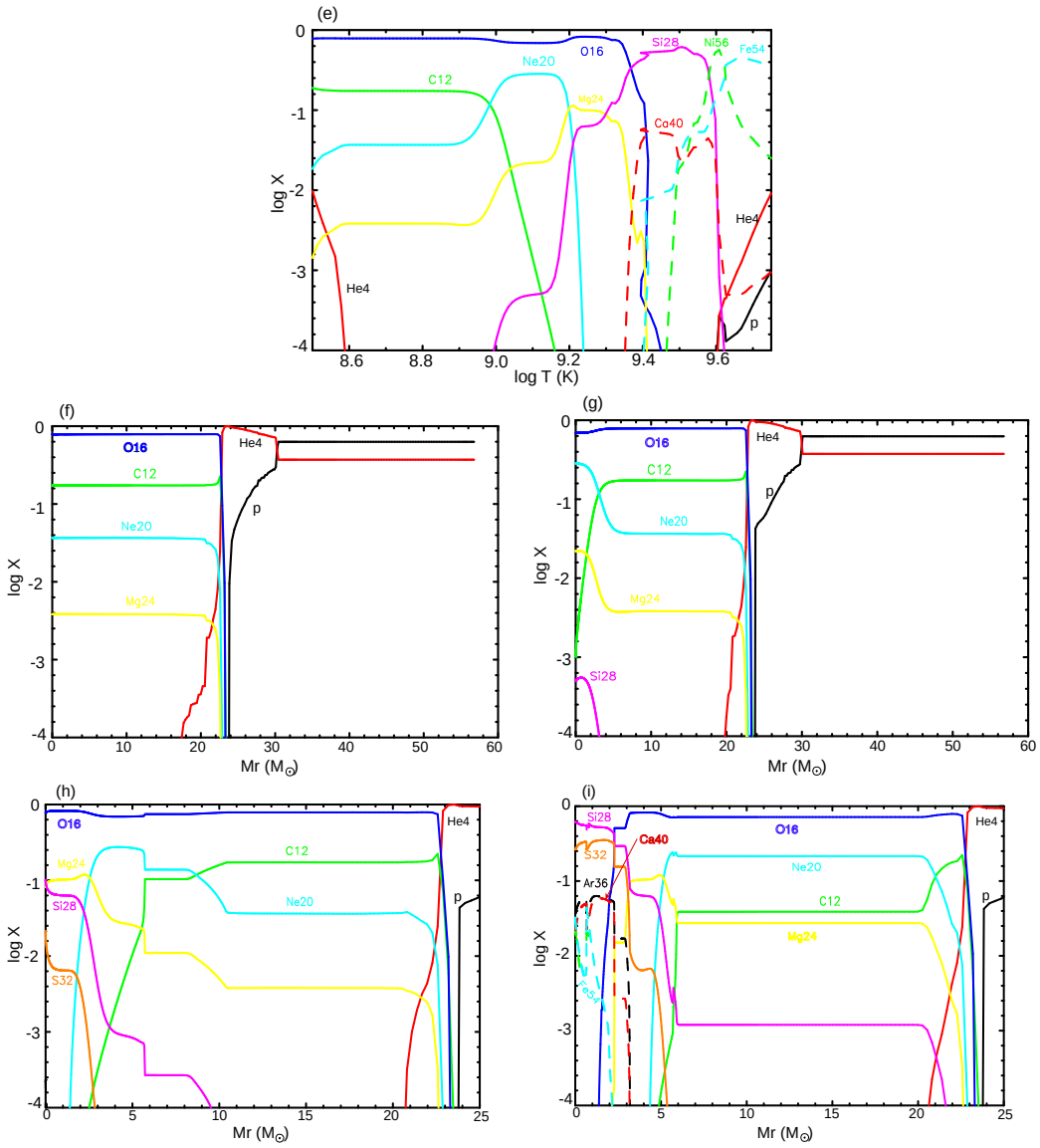

Figure 3.41 Figure 3.41 - continued.

3.4 Iron core collapse

For models Y-5, C-2, N-2, and N-3, the star ends its life as a PISN. For other models, the central iron core collapses to form a black hole. Whether a star explodes as a PISN or causes iron core collapse is decisively important for galactic chemical evolution , i.e., the origin of elements. This is because the mass ratio of each element ejected by a PISN cannot reproduce the abundance patterns of extremely metal-poor (EMP) stars, intergalactic medium (IGM), or intracluster matter (ICM) (Umeda & Nomoto 2002; Heger & Woosley 2002; Chieffi & Limongi 2002).

We calculate core collapse of a core beyond $\log T_c = 9.75$, with the beginning of core collapse by iron photodisintegration for four models Y-1, and Y-2, M-2, and M-3. Calculations are continued until the central density exceeds 9.0.

$M \gtrsim 300 M_\odot$ cases: Figure 3.42 shows snapshots and chemical composition at four stages for model Y-1. Stage 4 is the end point of the collapse calculation for model Y-1 ($\log T_c = 10.3$ and $\log \rho_c = 10.0$). Figure 3.43 is for model Y-2 at three stages. Stage 3 is the end point of the collapse calculation for model Y-2 ($\log T_c = 10.3$ and $\log \rho_c = 9.5$). One can see from the panels (a), (b), and (c) that for both models, the whole CO core collapses homologously ($\mid v \mid \propto r$: see panel (d)) from stage 1 to 2 ($\log T_c = 9.8$ to $\log T_c = 10.0$). However, from stage 2 to 3 (or stage 3 to 4 for Y-1), the inner part of the core collapses and the outer CO rich region can no longer follow the rapid central collapse. This means that the homologously collapsing region shrinks inward as the collapse proceeds, and thus the outer part is left to behave as free fall.

One notable point for the changes during core collapse is that silicon and oxygen burning proceeds outward rapidly. Panels (e) - (h) in Figure 3.42 for model Y-1 and (e) - (g) in Figure 3.43 for model Y-2 show snapshots of chemical structure (onion-like structure). If we define the outer edge of the iron core as the point where the mass fraction of ^{56}Ni exceeds that of ^{28}Si, and the outer edge of the silicon layer as the point where the mass fraction of ^{28}Si exceeds that of ^{16}O, the iron core extends from 120 to $200 M_\odot$ from stage 1 to 4 for model Y-1, and 100 to $180 M_\odot$ for model Y-2. This is because these regions can follow the central core collapse during these stages, as described above. Panels (i) means that the outer regions just follow the evolutionary track of density and temperature which the central region takes (overlapping of each line). For model Y-1, from stage 1 to 4, at the point where $M_r = 200 M_\odot$, $\log T$ rises from 9.5 ('B1' in panel (i) of Figure 3.42) to 9.6 ('B4'). What is more, this

point passes through the pair instability region as the central region once did. This temperature rise and instability are enough for oxygen to be converted into silicon there. Comparing panels (g) and (h), there are almost no changes (the outer edge of the iron core and the silicon layer hardly move). This is because these regions can no longer follow the rapid central collapse. The time it takes from stage 1 to 3 is ~ 30 seconds, whereas the time it takes for $\log T_c$ to rise from 9.4 to 9.6 during which the central oxygen is converted into silicon is ~ 50 seconds (see panel (e) in Figure 3.31). The two time scales are of the same order of magnitude. The same trend appears for model Y-2 (Figure 3.43). At the point where $M_r = 200 M_\odot$, $\log T$ rises from 9.45 ('B1' in panel (i) of Figure 3.43) to 9.55 ('B3'), and thus oxygen burns into silicon.

$M \lesssim 140 M_\odot$ cases: The core collapse of stars with $M \lesssim 140 M_\odot$ makes a clear contrast compared with CVMS ($M \gtrsim 300 M_\odot$) cases; iron core size, homologously collapsing area, etc. Figure 3.44 and Figure 3.45 depict the core collapse of model M-2 ($135 M_\odot$) and model M-3 ($57 M_\odot$), respectively. For these two models, temperature and density gradients are steep in the iron and silicon layer (panels (a) - (c)). In CVMS cases the gradient are gentler in these layers. From panel (d), one can see that homologously collapsing region hardly changes during the calculation. For $M \lesssim 140 M_\odot$ cases, homologously collapsing region is limited only iron core at the very beginning of iron photodisintegration. Therefore, neither silicon nor oxygen layer can follow the central iron core collapse.

Panels (e) - (g) in Figure 3.44 and Figure 3.45 show snapshots of chemical composition. The size of iron core or silicon layer hardly moves outward. This relates to the fact described the previous paragraph that homologously collapsing region is limited in iron core only. We conclude from the discussion above that the large size of the iron core of VMS ($\sim 20 - 25\%$ of the total stellar mass), much larger than $M \lesssim 140 M_\odot$ stars (~ 10 %), is realized during the core collapse. Therefore, if one intends to execute calculations for phenomena such as explosion and nucleosynthesis (setting the initial chemical composition for the nucleosynthesis), one has to carry out calculations least until $\log \rho_c$ reaches 9. For CVMS cases, the timescale of iron photodisintegration to collapse and that of silicon and oxygen shell burnings are same. It reflects the fact that the place where shell burnings occur is in pair instability region and collapses rapidly, so shell burnings occur explosively. On the other hand, for $M \lesssim 140 M_\odot$ star cases, collapsing timescale is much shorter than shell burning timescale. This is because shell burnings occur stably for such lower mass stars.

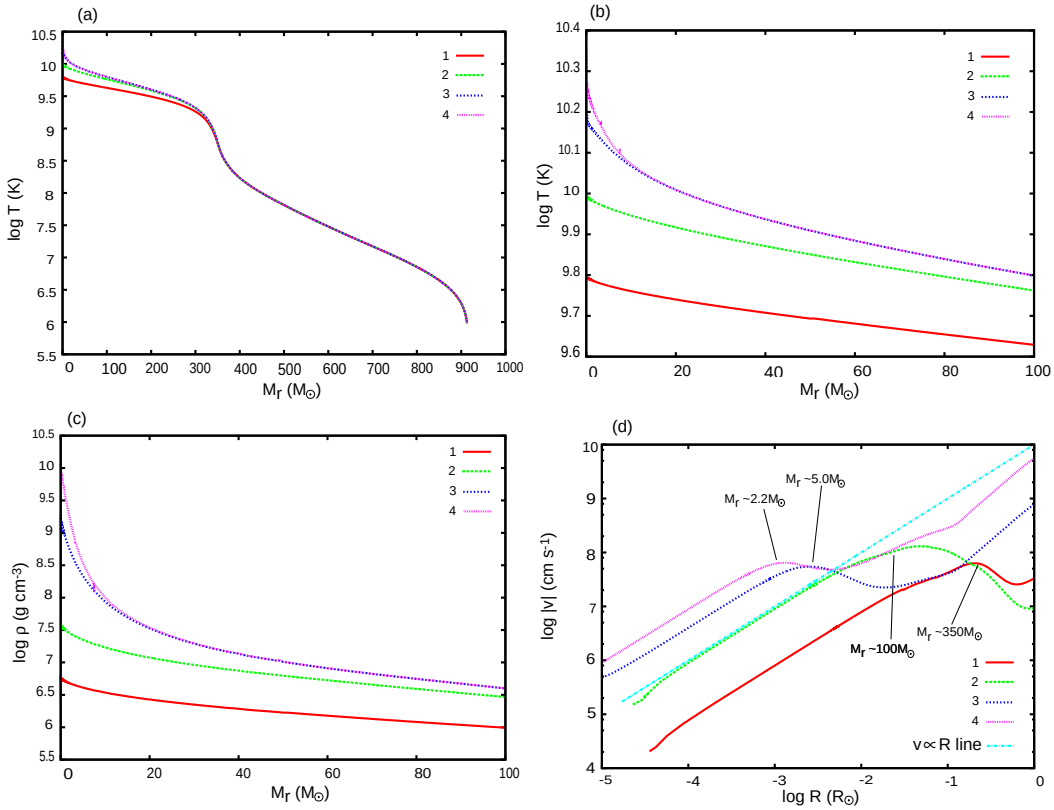

Figure 3.42 Snapshots of temperature structure (a), temperature structure in the central region (b), density structure in the central region(c), velosity-radius relation (d) at four stages. The attached number with each line refers to the stage when $\log T_c = 9.8$ and $\log \rho_c = 6.7$(stage 1), $\log T_c = 10.0$ and $\log \rho_c = 7.5$(stage 2), $\log T_c = 10.1$ and $\log \rho_c = 9.2$(stage 3), and $\log T_c = 10.3$ and $\log \rho_c = 10.0$(stage 4). Attached mass coordinate M_r in panel (d) indicates the outer edge of homologously collapsing region.

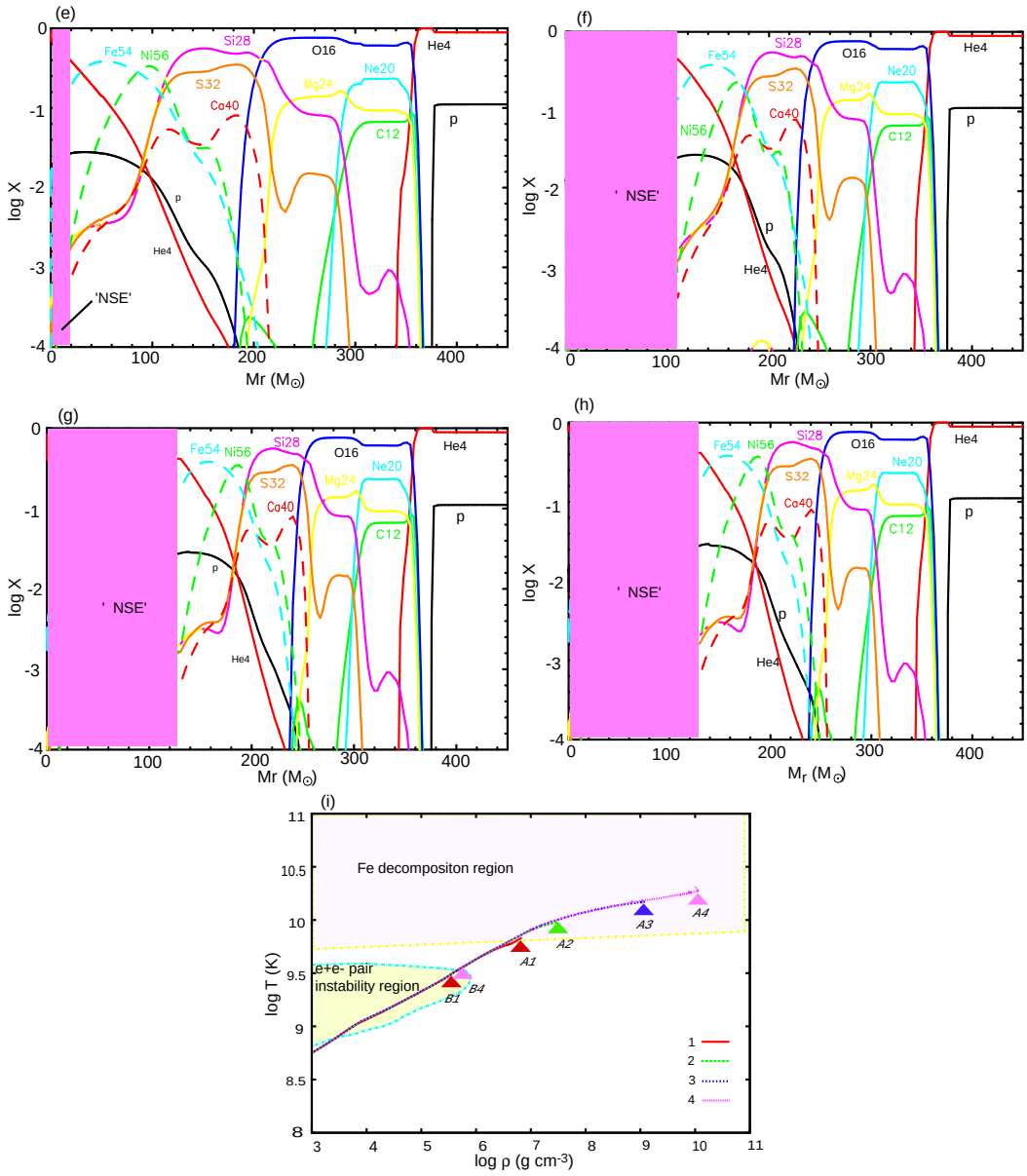

Figure 3.42 Figure 3.42 - continued. (e) -(h): Snapshots of chemical composition at stage 1 (e), stage 2 (f), stage 3 (g), and stage 4 (h). (i): snapshots of temperature-density relations at four stages. Point 'A1' shows temperature and density at the center at stage 1, 'A2' at stage 2, 'A3' at stage 3, 'A4' at stage 4, respectively. 'B1' is those at the mass coordinate $M_r = 200 M_\odot$ at stage 1, 'B4' is those at stage 4.

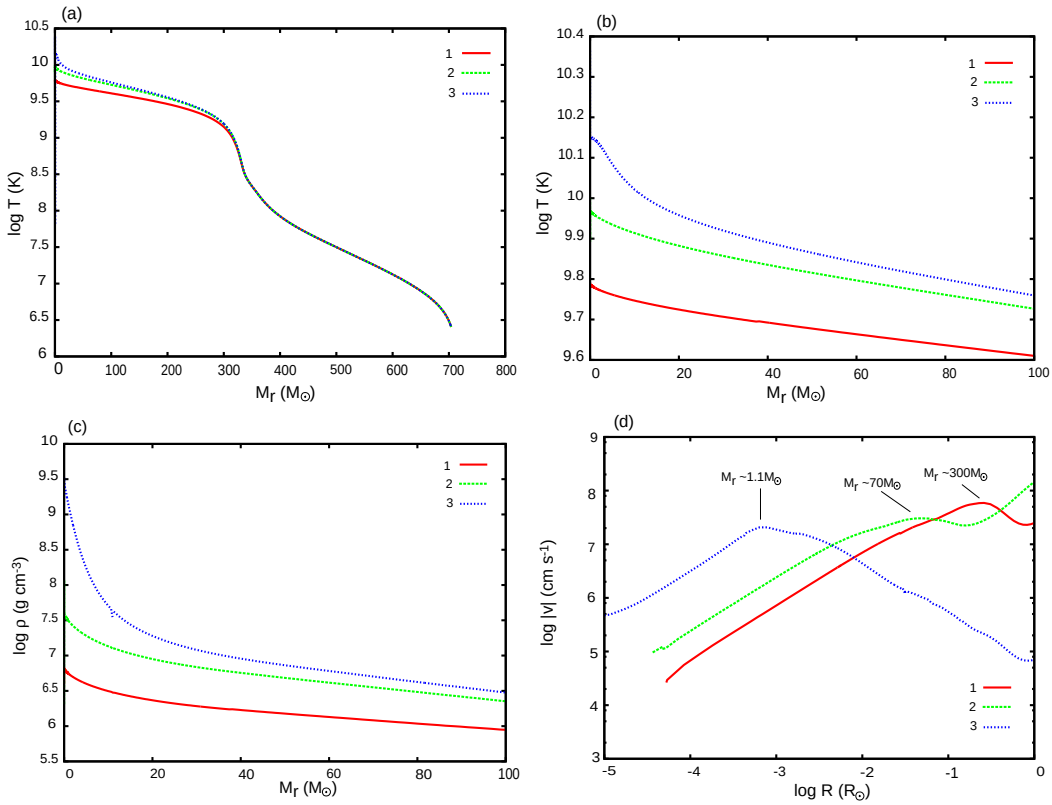

Figure 3.43 Same as Figure 3.42, but for model Y-2. Three stages are shown. Stage 1 is when $\log T_c = 9.8$ and $\log \rho_c = 6.5$, stage 2 when $\log T_c = 10.0$ and $\log \rho_c = 7.5$, stage 3 when $\log T_c = 10.3$ and $\log \rho_c = 9.5$.

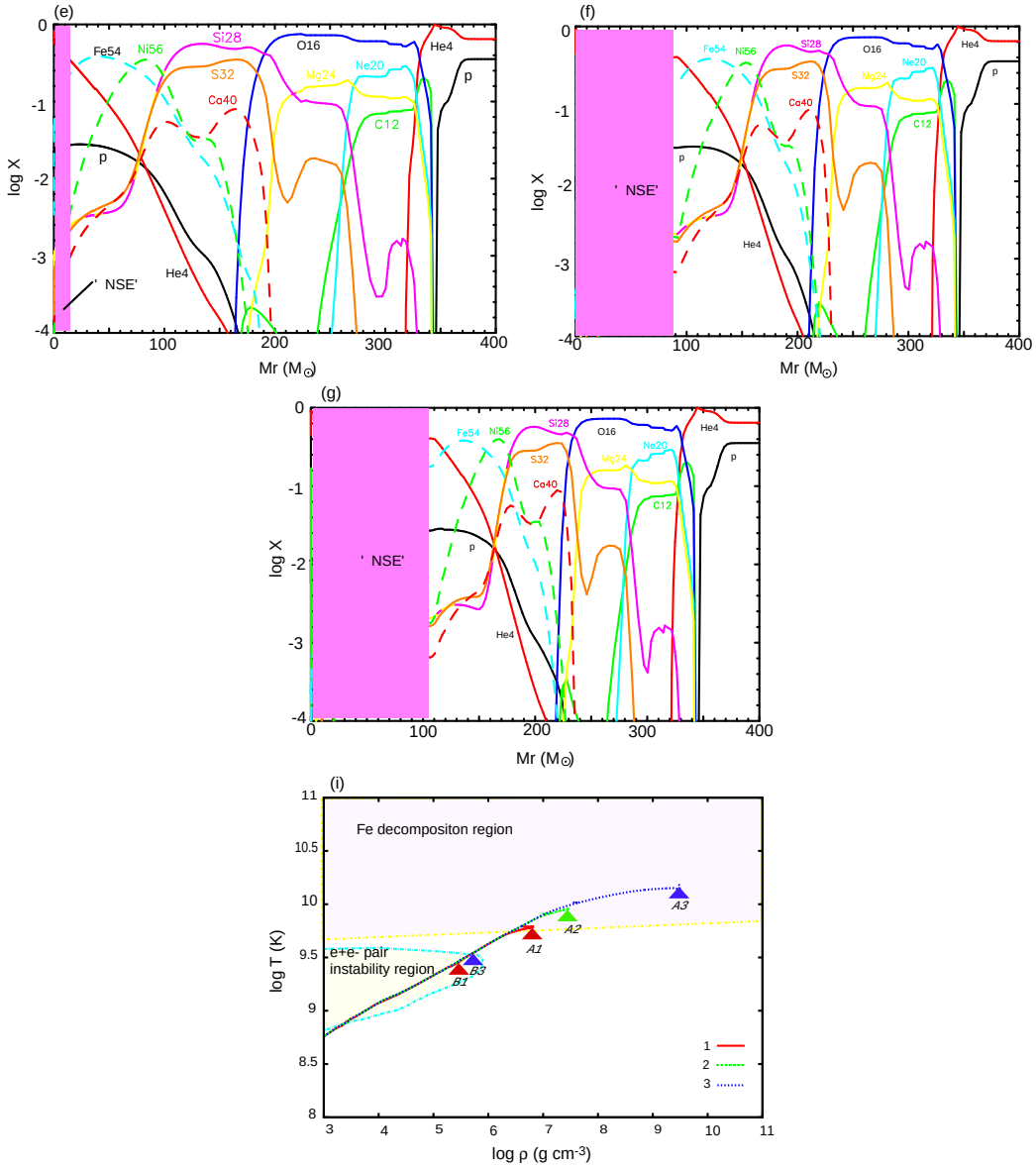

Figure 3.43 Figure 3.43 - continued. (e) - (g): Snapshots of chemical composition at stage 1 (e), stage 2 (f), and stage 3 (g). (i): snapshots of temperature-density relations at three stages. The characters 'A1', 'A2', 'A3', 'B1', and 'B3' have the same meaning as for model Y-1.

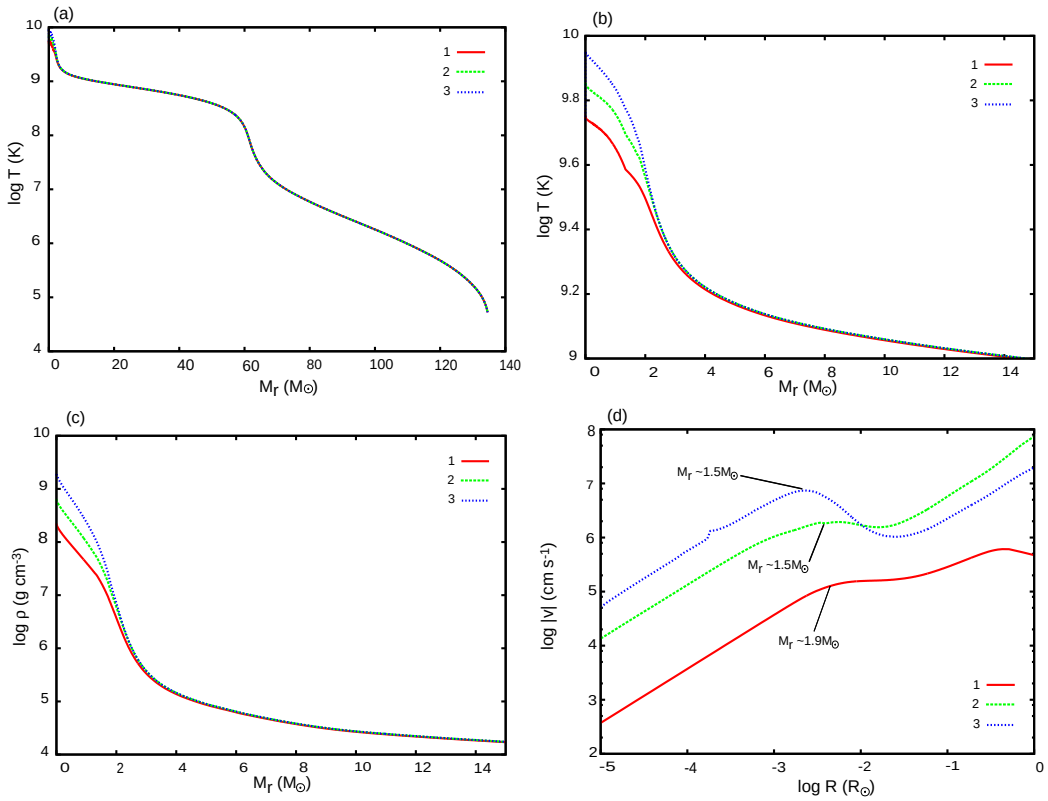

Figure 3.44 Same as Figure 3.43, but for model M-2. Stage 1 is when $\log T_c = 9.75$ and $\log \rho_c = 8.3$, stage 2 when $\log T_c = 9.85$ and $\log \rho_c = 8.8$, stage 3 when $\log T_c = 9.95$ and $\log \rho_c = 9.3$.

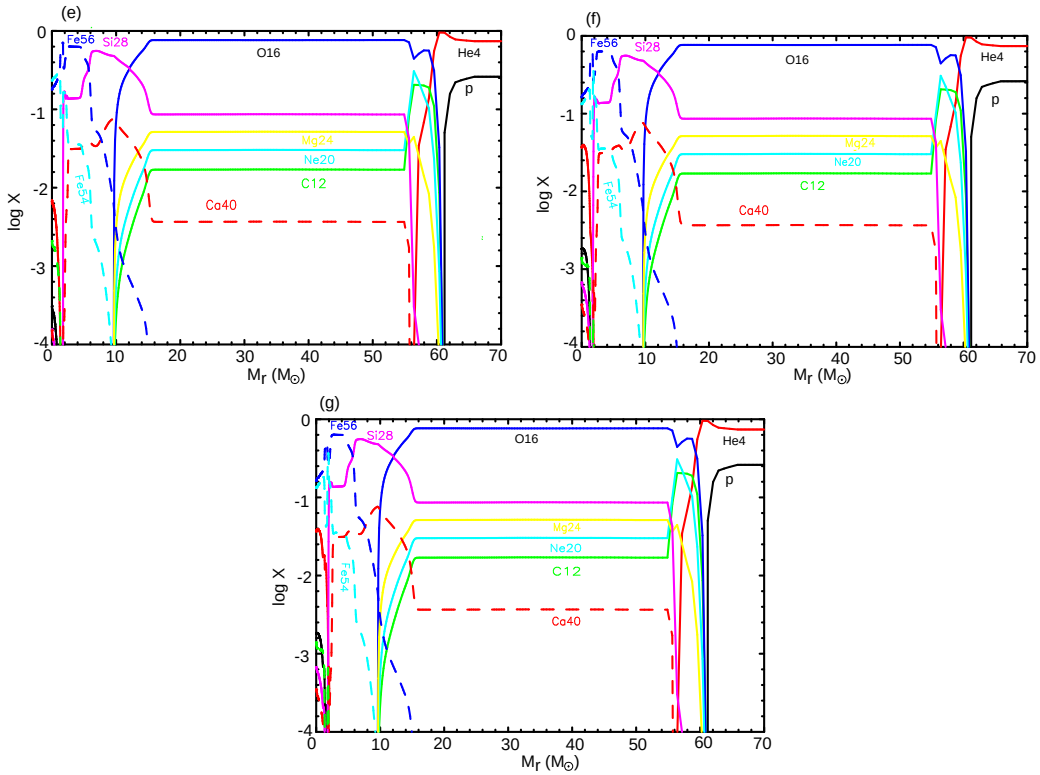

Figure 3.44 Figure 3.44 - continued. (e) - (g): Snapshots of chemical composition at stage 1 (e), stage 2 (f), and stage 3 (g).

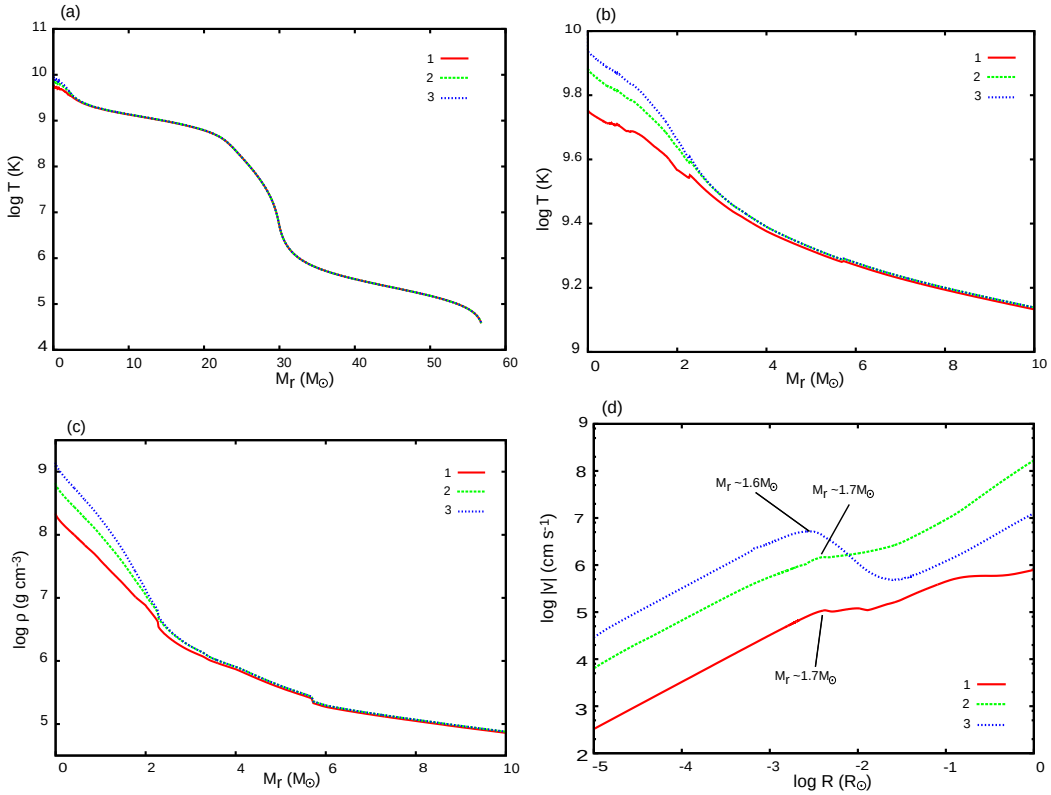

Figure 3.45 Same as Figure 3.43, but for model M-3. Stage 1 is when $\log T_c = 9.75$ and $\log \rho_c = 8.3$, stage 2 when $\log T_c = 9.85$ and $\log \rho_c = 8.7$, stage 3 when $\log T_c = 9.94$ and $\log \rho_c = 9.1$.

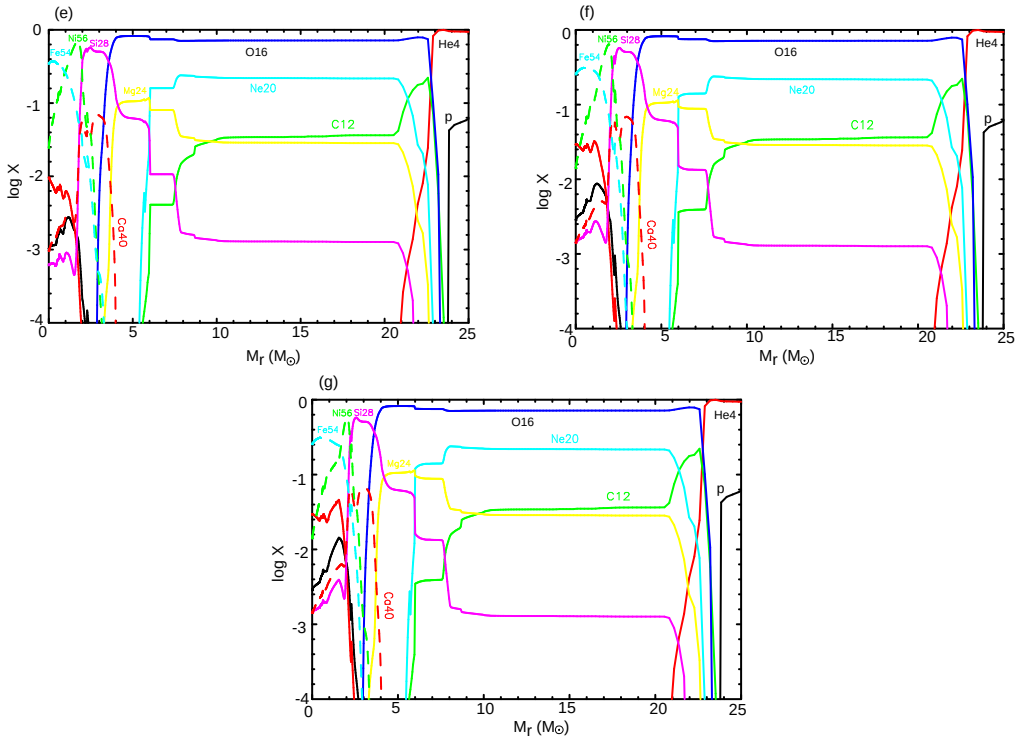

Figure 3.45 Figure 3.45 - continued. (e) - (g): Snapshots of chemical composition at stage 1 (e), stage 2 (f), and stage 3 (g).

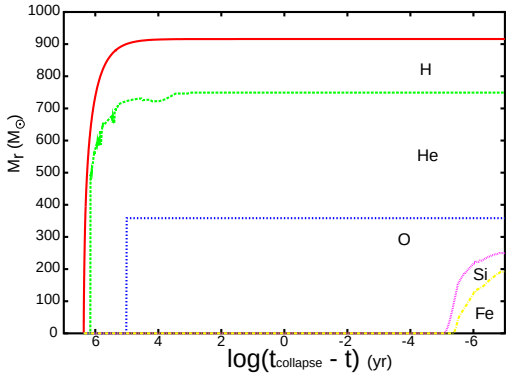

Figure 3.46 A stellar structure diagram for model Y-1. This diagram shows the evolution of each layer and convective regions as a function of time left until the core collapse. Each layer corresponds to the area where the element indicated is the main one in mass fraction.

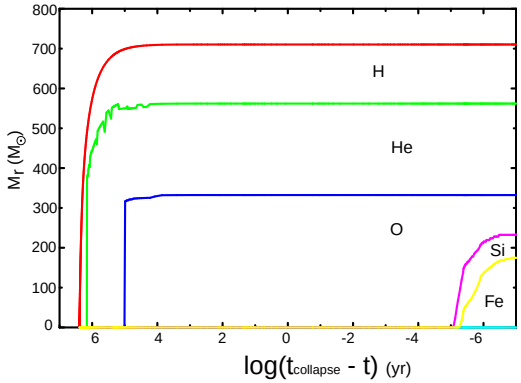

Figure 3.47 Same as Figure 3.46, but for model Y-2.

In summary, we show stellar structure evolution diagram for models Y-1, Y-2, M-2, and M-3 in Figures 3.46 through 3.49. For each model CO core is formed at $t_{\rm collapse} - t \sim 5$.

For CVMS ($M \gtrsim 300 M_\odot$) models (here models Y-1 and Y-2), When carbon is ignited, the central region enters the pair instability region and the evolution (nuclear burning) time scale is very short. During collapse ($t_{\rm collapse} - t \lesssim -6.0$), silicon and iron layers grow in mass as describe in the previous paragraph.

For $M \gtrsim 140 M_\odot$ models (here models M-2 and M-3), silicon and iron layers hardly grow during collapse ($t_{\rm collapse} - t \lesssim -6.0$) because shell burning occurs stably, i.e., the nuclear shell burning timescale is much longer than the collapse timescale.

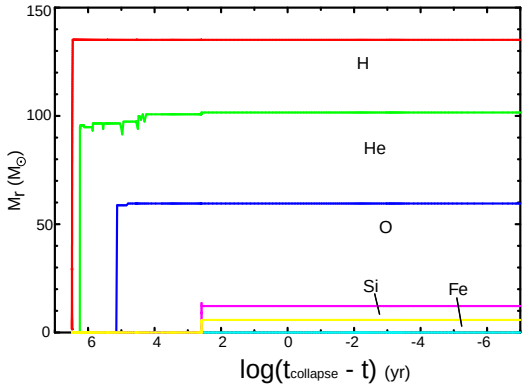

Figure 3.48 Same as Figure 3.46, but for model M-2.

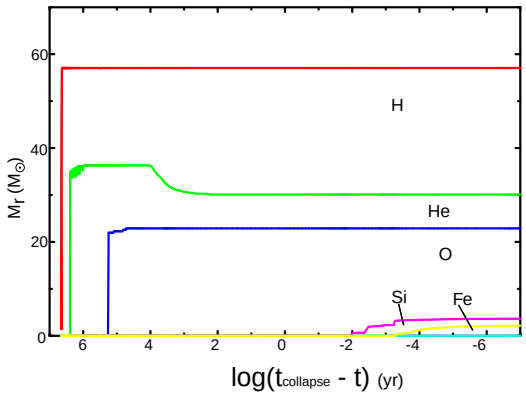

Figure 3.49 Same as Figure 3.46, but for model M-3.

CHAPTER 4
DISCUSSION

The evolution of PopIII VMSs has been studied extensively (e.g., Bond et al. 1984; Heger et al. 2001, 2003; Ohkubo et al. 2006). If such stars explode at the end of their life, a large amount of heavy elements are distributed into space. It can significantly contribute to galactic chemical evolution.

Then the ratios of ejected mass of each element can be directly compared with the observational abundance patterns of extremely metal-poor (EMP) stars in Galactic halo, intergalactic medium (IGM), and intracluster matter (ICM). For each mass range, explosion and nucleosynthesis calculations of Pop III star have been carried out; see e.g., Iwamoto et al. (2007), Tominaga, Umeda, & Nomoto (2007), Limongi & Chieffi (2003), Heger & Woosley (2008) for ordinary massive stars ($20 - 40 M_{\odot}$), Umeda & Nomoto (2002) and Heger & Woosley (2002) for PISN and Ohkubo et al. (2006) for CVMS.

In Ohkubo et al. (2006) we calculated evolution, nucleosynthesis, explosion and collapse of Pop III core-collapse very massive stars with mass $M \sim 300 M_{\odot} - 1000 M_{\odot}$. The calculations were started at the beginning of main sequence and the stellar mass was held constant through the lifetime (no accretion and no mass loss). In this thesis, we extended the earlier work by starting the evolution from a protostar and allowing mass accretion all through its life. In both cases the final mass obtainable is found to be similar, $M \sim 300 M_{\odot}$ – $1000 M_{\odot}$, but in this work physics is treated more realistically.

The proto-stellar evolution roughly follows the results of Yoshida et al. (2006). The star settles into the main-sequence after the central temperature T_c exceeds 10^8 K, when CNO cycle is operative with $X(\mathrm{CNO}) \sim 10^{-9}$. The stellar mass at this stage is $M \sim 10 - 100 M_{\odot}$.

Previous proto-stellar calculations ended at the onset of hydrogen burning on the main-sequence. Our results show that with mass accretion the stellar mass continues to grow after the protostar phase through the main sequence and beyond.

Assuming that radiative feedback is not significant in a majority of cases, we have confirmed the conclusion of Paper I that there is a realistic possibility for the existence of CVMSs as Pop III stars in the early universe. In Ohkubo et al. (2006), we argued that these CVMSs contribute significantly to the metal enrichment of the

early universe, while preventing the overabundance, before ending their life quickly before ordinary core-collapse supernovae and hypernovae became dominant. Also we found that the abundance of ejected heavy metals in this CVMS scenario agrees well with the observed chemical abundance data from the early universe, in contrast to poor agreement of the abundance patterns of PISNe. This is because the mass ratio of each element ejected by PISNs cannot reproduce the abundance patterns of extremely metal-poor (EMP) stars, intergalactic medium (IGM), or intracluster matter (ICM) (Umeda & Nomoto 2002; Heger & Woosley 2002; Chieffi & Limongi 2002). On the other hand, ejected mass ratios of each element from ordinary massive stars are consistent with especially EMP stars (Iwamoto et al. 2007, Tominaga, Umeda, & Nomoto (2007)). If the majority of the first generation (Pop III.1) are CVMSs, they form a IMBH, not explode as a PISN. And then, the second generation (Pop III.2) stars which form under the influence of radiation from Pop III.1 stars are less massive than $M \lesssim 100 M_{\odot}$. This scenario may explain why PISN signatures are not observed in the abundance patterns.

The presence of CVMS in the early universe, if confirmed, has important implications for progenitors of IMBHs. Stellar mass black holes ($\sim 10 M_{\odot}$) are formed as the central compact remnants of ordinary massive (25 - $140 M_{\odot}$) stars at the end of their evolution. Supermassive black holes (SMBHs) ($\sim 10^5$ - $10^9 M_{\odot}$) are now known to exist in the center of almost all galaxies (e.g., Kormendy & Richstone 1995; Bender 2005), but their formation processes are largely unknown. IMBHs might seed the SMBH formation. There is an interesting indication that some IMBHs have been, indeed, found (Barth et al. 2005). Matsumoto et al. (2001) reported possible identification of a $\gtrsim 700 M_{\odot}$ black hole in M82, by using *Chandra* data. Other possible detections have also been reported as ultra-luminous X-ray sources (ULXs) (Colbert & Mushotzky 1999; Makishima et al. 2000) and an object in the Galactic center (Hansen & Milosavljevic 2004). Especially, the most recent evidence from Suzaku X-ray Satellite mission is convincing (Makishima 2008).

Let us return to formation of SMBHs. There are several scenarios (e.g., Rees 2002, 2003). SMBHs may be formed directly from supermassive halos of dark matter (e.g., Marchant & Shapiro 1980; Bromm & Loeb 2003; Begelman et al. 2006). Madau and Rees (2001) first suggested that mini halos with heavy black holes with mass $\sim 150 M_{\odot}$ at redshift ~ 20 will merge with each other successively to eventually form SMBHs. Ebisuzaki et al. (2001) suggested a scenario where IMBHs grow to become a SMBH

by merging and swallowing of many of these objects. Detectability of gravitational waves radiated by IMBH binaries by observatories such as LISA and LIGO has been studied (Sesana et al. 2007; Micic et al. 2007; Tanaka & Haiman 2008; Plowman et al. 2008). If CVMSs actually existed, they could be considered as natural progenitors of IMBHs. Recently, the role of IMBHs caught much attention in the context of the formation of super-massive black holes (SMBHs). One of the viable scenarios for SMBH formation is a merger tree model in which seed black holes of a few hundred solarmasses formed early (e.g., at $z \sim 20$) are assumed to have merged and grown to become SMBHs (e.g., Madau and Rees 2001; Volonteri et al. 2003). In this model, the small seed black holes generally go through IMBH stages at some intermediate epochs, i.e., between $z \sim 20$ and 0. It has been suggested that these IMBHs at high redshifts can be detected by *Laser Interferometer Space Antenna* (Sesana et al. 2007; Micic et al. 2007; Tanaka & Haiman 2008; Plowman et al. 2008). Our results offer a natural scenario for the formation of seed black holes responsible for the merger tree model.

Our present work uses a result from a three-dimensional cosmological simulation by Yoshida et al. (2006) which follows the evolution of dense gas clumps formed at the centers of rather low mass ($\sim 10^{5-6} M_\odot$) dark matter (DM) halos at redshifts $z \simeq 20$. Volonteri et al. (2003) have shown that the merger tree scenario starting with black hole seeds of $\simeq 150 M_\odot$ at redshift of 20 is consistent with the present day SMBH population (estimated from observed quasar luminosity and mass functions, etc). However, any relevant model also must be consistent with the presence of SMBHs massive enough (a few $\times 10^9 M_\odot$) to power the bright high redshift quasars recently discovered by the Sloan Digital Sky Survey (see, e.g, a recent review by Fan 2006). Various models have been proposed to explain these high redshift powerful massive SMBHs (e.g., Volonteri & Rees 2006; Begelman et al. 2006; Li et al. 2007, 2008). In some of these models, the seed black holes have to be formed in hotter (virial temperature $T_{\rm vir} \geq 10^4$ K) and more massive ($> 10^8 M_\odot$) DM halos, and the BHs grow by supercritical accretion, in order to become massive enough by $z \simeq 6$. Tanaka & Haiman (2008) further extended these earlier studies and examined successful scenarios which can be constrained by both high redshift and local SMBH populations. In some of these models (e.g., Volonteri & Rees 2006; Tanaka & Haiman 2008) the seed black holes are of the order of $100 M_\odot$ formed from collapse of Pop III VMSs, while in some others the seeds are SMBHs of the order of $10^5 M_\odot$ which

are formed directly from DM halos (e.g., Volonteri & Rees 2006; Tanaka & Haiman 2008). Tanaka & Haiman (2008) conclude that the models with seed black holes from both models can be successful (to be consistent with both $z = 6$ and local quasar populations), but LISA observations can distinguish them by gravitational wave detections from binary black holes. The environment where the seed black holes are formed (with much more massive and hotter DM halos) is quite different from that of conventional star formation models such as those of Yoshida et al. (2006). Therefore, one possible interesting extension of our current work will be to adopt supercritical accretion in the environment of these more massive hotter DM halos.

Tanaka & Haiman (2008) show that in a successful scenario for $z = 6$ quasar formation, if the seed black holes are $100 M_{\odot}$ which were formed from Pop III stars, then these holes must be formed rather early, with $z > 30$. From Figure 3 of Tanaka & Haiman (2008) we see that this constraint will be appreciably eased if the seed black holes are larger instead, such as IMBHs of $500 M_{\odot}$ from our CVMSs. The maximum mass for seed black holes to be formed from CVMSs may still become larger if the environment of hot, massive DM hales (of $T_{\rm vir} \geq 10^4$ K) is adopted in our future calculations.

We focus our attention to a model of VMS formation by accretion. Although a different model for the formation of VMSs has been presented by Ebisuzaki et al. (2001), Portegies Zwart et al. (1999), Portegies Zwart et al. (2004a), and Portegies Zwart (2004b), where VMSs are formed by merging of less massive stars in the environment of very dense star clusters, we do not consider such a scenario here because star cluster formation appears less likely in the early universe.

CHAPTER 5
CONCLUSIONS

In this thesis, we calculate the evolution of population III (Pop III) stars whose masses grow from the initial masses of $\sim 1 M_\odot$ by accreting the surrounding gases. My calculations cover all evolutionary stages from the pre-main sequence, via various nuclear burning stages, through the final core collapse or pair-creation instability phases. We calculate models with various mass accretion rates: (1) constant accretion rates throughout the evolution, (2) stellar mass dependent accretion rates which are derived from cosmological simulations of early structure formation (Pop III.1 stars) based on the low mass dark matter halos at redshifts $z \sim 20$, (3) mass dependent accretion rates which are affected by radiative feedback, (4) mass dependent accretion rates for zero-metallicity but second generation (Pop III.2) stars which are affected by radiation from the first generation (Pop III.1) stars. The evolutions of massive stars without mass accretion are also calculated and compared with the results of mass accreting models.

This thesis focuses mainly on the following two points: (I) the influences of mass accretion on the final fate, and (II) the later evolution stages after central helium burning of Pop III massive stars. We unveil these aspects and summarize my findings as follows.

(I) Final stellar masses, and the final fates

We find that unless the accretion rate is significantly reduced by feedback effects, the final stellar mass $M_{\rm f}$ can be even as large as $M_{\rm f} \gtrsim 300 M_\odot$. Such a massive star undergoes core collapse and would form an intermediate mass black hole (IMBH). Compared with the non accreting models whose masses are almost equal to the final masses of $M_{\rm f}$, the mass accreting stars have the following features. (i) The stellar lifetime is longer because the stellar mass is smaller during hydrogen burning. (ii)The CO core masses are smaller because M is smaller and still increasing during helium burning. (iii) However, these differences are too small to significantly change the final fates of stars as a function of $M_{\rm f}$. Therefore, we expect that the pair instability supernovae (PISNe) mass range hardly changes.

The final mass of Pop III.1 stars can be very large ($M \gtrsim 300 M_\odot$), beyond the PISNe mass range. Such massive stars form IMBHs, which may be the seeds for merger tree to supermassive black holes. On the other hand, Pop III.2 stars are less

massive ($M \lesssim 40-60M_{\odot}$), being in the mass range of ordinary iron core-collapse stars. Such stars explode and eject heavy elements to contribute to chemical enrichment of the early universe. The stars in this mass range are favorable candidates for elemental origin of extremely metal-poor stars in the Galactic halo. We can explain why the signature of PISNe are not seen with the scenario that Pop III.1 stars are very massive, i.e., $M \gtrsim 300M_{\odot}$ and Pop III.2 stars are less massive, i.e., $M \lesssim 40-60M_{\odot}$, although there is some uncertainty in radiative feedback.

(II) Later evolutionary stages after helium burning

There are many previous works in Pop III stellar evolution for each mass range. However, most of such calculations have been carried out only through the stage before the end of central helium burning, and only few calculations have been performed until late stages of oxygen, silicon burning, and pre-core-collapse. The detailed study of the characteristics of such late stages of evolution for stars with $M \gtrsim 300M_{\odot}$ and $M \sim 100M_{\odot}$ is also one of the purpose of this thesis.

For very-massive stars, carbon does not ignite until the central temperature exceeds 10^9 K. During core collapse, the silicon layer and iron core grow in mass considerably, and then the final size of the iron core is much larger than for ordinary massive stars due to the explosive oxygen and silicon shell burnings. On the other hand, less massive stars ($M \lesssim 140M_{\odot}$), oxygen and silicon shell burnings occurs stably and the burning time scale is much longer than collapse time scale. As a result, the iron core and the silicon layer are small to the whole mass.

For stars in the mass range $80M_{\odot} \lesssim M \lesssim 140M_{\odot}$ the CO core oscillates during oxygen and silicon burnings. The amplitude is larger and oscillation period is longer for more massive models. This phenomenon is typical for this mass range, and occurs even if metallicity is not zero. Such stars are considered as origin of very bright supernovae.

(III) Prospects

The possibility of our scenario that the majority of Pop III.1 stars are CVMSs ($M \gtrsim 300M_{\odot}$) and the majority of Pop III.2 stars is ordinary massive stars ($M \lesssim 40M_{\odot}$) is attractive because it explains the chemical evolution of the early universe in that PISN mass range ($140M_{\odot} \leq M \leq 300M_{\odot}$) can be avoided. Moreover, the range of large mass found gives the attractive possibility that these CVMSs are indeed progenitors of IMBHs. Although the presence of IMBHs has not been firmly established, there are various recent observational indications. If many of IMBHs indeed existed in the

early universe, even if they are rare today, it will provide valuable insights to the formation of SMBHs and ultimately galaxy formation and evolution. We expect that future detection of neutrinos and gravitational wave emitted from collapsing CVMSs exemplify the existence of CVMSs as First Stars.

APPENDIX A
NUMERICAL METHODS AND PHYSICAL OVERVIEW OF STELLAR EVOLUTION

A.1 Basic equations of stellar structure

Inner region The code solves these equations above for each element and gives abundances along stellar evolution. The equations 2.6 - 2.9 and 2.13 contain $4 + I$ unknown variables, i.e., $r, P, T, l, X_1, ..., X_I$. The number of equations is also $4 + I$, the number of unknown variables and that of equations are same.

Outer envelope In outer envelope, the luminosity l is assumed to be constant and equal to the stellar total luminosity L. In our code, pressure in logscale log$p$ is adopt as the independent variable, and the three unknown variables are T, r, m (l is assumed to be L)

$$\frac{d\log T}{d\log p} = \begin{cases} \nabla_{\rm rad}(\nabla_{\rm rad} \leq \nabla_{\rm ad}) : \text{radiative} \\ \nabla_{\rm con} = (\frac{\log T}{\log p})_{\rm con} : \text{convective} \end{cases} \tag{A.1}$$

$$\frac{d\log r}{d\log p} = -\frac{rp}{Gm\rho} \tag{A.2}$$

$$\frac{d\log m}{d\log p} = -\frac{4\pi r^4 p}{Gm^2}. \tag{A.3}$$

A.2 Boundary conditions

The four basic equations 2.6 - 2.9 can be solved as a boundary condition problem. Integrations are performed both from the center and the surface and the two solutions are fitted at an intermediate point (fitting point $m_{\rm F}$). In this method one needs four boundary conditions and four parameters.

Central region Two of the four boundary conditions are imposed at the center, i.e., $m = 0$. These conditions are written that the radius and the luminocity must

vanish at the center:

$$r = 0, \quad l = 0 \qquad \text{at} \qquad m = 0. \tag{A.4}$$

The pressure and the temperature at the center are not trivialy known, so one have to parametrize these two values:

$$T = T_c, \quad P = P_c \qquad \text{at} \qquad m = 0. \tag{A.5}$$

With these values, solutions are obtained by outward integrations.

Surface region The rest two boundary conditons are set at the surface, i.e., $m = M$ (M is the stellar mass). It is usually defined as the stellar surface where the optical depth $\tau = 2/3$. It is called 'photosphere', and at this point

$$P = \frac{2GM}{3R^2\kappa} \tag{A.6}$$

where $\bar{\kappa}$ is the mean opacity, averaged over the stellar atmosphere. The temperature at the surface is related to the stellar luminocity $l(M) = L$. This temperature is called 'effective temperature' $T_{\rm eff}$ and defined by

$$L = 4\pi R^2 \sigma T_{\rm eff}^4. \tag{A.7}$$

$\sigma = ac/4$ is the Stefan-Boltzmann constant. L is a parameter to be chosen togather with the stellar radius $r(M) = R$. With these values, solutions are obtained by inward integrations.

A.3 The henyey method

There exists a well known method to solve equations 2.6 - 2.9 numerically called 'the henyey method' (Henyey et al. 1964). With this method one renealize the equations and save the computational time by subdividing a matrix. In this subsection we summarize how to solve the equations by the henyey method. More details are described in Kippenhahn et al. (1967) and references therein.

We express pressure P, temperature T, and radius r with log scale in our code.

We replace the four basic differential equations 2.6 - 2.9 of discretized values in the following forms

$$\log p^j - \log p^{j-1} = -\triangle x^j \sqrt{V^j V^{j-1}} \tag{A.8}$$

$$\log T^j - \log T^{j-1} = 0.5(\log p^j - \log p^{j-1})(\nabla^j + \nabla^{j-1}) \tag{A.9}$$

$$\log r^j - \log r^{j-1} = \triangle x^j \sqrt{W^j W^{j-1}} \tag{A.10}$$

$$l_r^j - l_r^{j-1} = (q^j - q^{j-1})(\sqrt{\epsilon_n^j \epsilon_n^{j-1}} - \sqrt{\epsilon_\nu^j \epsilon_\nu^{j-1}} + \frac{\epsilon_g^j + \epsilon_g^{j-1}}{2}) \tag{A.11}$$

$$j = 3, ..., N$$

where

$$\triangle x^j = \log q^j - \log q^{j-1}, \quad , V^j = \frac{Gm^2}{4\pi r^4 p}, \quad , W^j = \frac{1}{4\pi r^3 \rho} \tag{A.12}$$

Hereafter we rewrite $y_1 = \log p$, $y_2 = \log T$, $y_3 = \log r$, and $y_4 = l_r$ for simple expression.

For the most inner mesh ($j = 1$), we use the two boundary conditions at the center. Because we express radius r in log scale, we take the most inner mesh very close to the center, not the center itself. We set the inner boundary conditions

$$y_4^1 = 0 (l_r^1 = 0), \quad W^2 = \frac{1}{3}(\frac{2\rho^1}{5\rho^2} + \frac{3}{5}) \tag{A.13}$$

where W^2 is derived from the relation that the gas density near the center is inversely proportional to the square of the radius. We adopt this condition insted of $r = 0$. So for $j = 1$

$$y_1^2 - y_1^1 = -\triangle x^1 \sqrt{V^2 V^1} \tag{A.14}$$

$$y_2^2 - y_2^1 = 0.5(y_1^2 - y_1^1)(\nabla^2 + \nabla^1) \tag{A.15}$$

$$\frac{1}{3} = W^2 / \{0.4(\rho^1/\rho^2) + 0.6\} \tag{A.16}$$

$$y_4^2 - 0 = (q^2 - q^1)(\sqrt{\epsilon_n^2 \epsilon_n^1} - \sqrt{\epsilon_\nu^2 \epsilon_\nu^1} + \frac{\epsilon_g^2 + \epsilon_g^1}{2}) \tag{A.17}$$

We gather all terms in the left hand side.

$$B_1 = y_1^2 - y_1^1 + \triangle x^1\sqrt{V^2V^1} = 0 \tag{A.18}$$

$$B_2 = y_2^2 - y_2^1 - 0.5(y_1^2 - y_1^1)(\nabla^2 + \nabla^1) = 0 \tag{A.19}$$

$$B_3 = \frac{1}{3} - W^2/\{0.4(\rho^1/\rho^2) + 0.6\} = 0 \tag{A.20}$$

$$B_4 = y_4^2 - 0 - (q^2 - q^1)(\sqrt{\epsilon_n^2\epsilon_n^1} - \sqrt{\epsilon_\nu^2\epsilon_\nu^1} + \frac{\epsilon_g^2 + \epsilon_g^1}{2}) = 0 \tag{A.21}$$

$$A_1^j = y_1^j - y_1^{j-1} + \triangle x^j\sqrt{V^jV^{j-1}} = 0 \tag{A.22}$$

$$A_2^j = y_2^j - y_2^{j-1} - 0.5(y_1 j - y_1 j - 1)(\nabla^j + \nabla^{j-1}) = 0 \tag{A.23}$$

$$A_3^j = y_3^j - y_3^{j-1} - \triangle x^j\sqrt{W^jW^{j-1}} = 0 \tag{A.24}$$

$$A_4^j = y_4^j - y_4^{j-1}$$

$$-(q^j - q^{j-1})(\sqrt{\epsilon_n^j\epsilon_n^{j-1}} - \sqrt{\epsilon_\nu^j\epsilon_\nu^{j-1}} + \frac{\epsilon_g^j + \epsilon_g^{j-1}}{2}) = 0 \tag{A.25}$$

$j = 3, ..., N$

The two boundary conditions at the fitting point $m = m_{\mathrm{F}}$ are

$$C_i = 0 \qquad i = 1, 2. \tag{A.26}$$

The number of equations and that of unknown variables ${y_i}^j$ are same $(4N - 2)$.

Linealization

The solution ${y_i}^j$ are found from linealized algebraic equations by repeating corrections. First we estimate roughly values as the solution of equations A.21 - A.26:

$$ {y_i}^j = ({y_i}^j)_k. \tag{A.27}$$

The index k means the k-th solution obtained by repeating correction k times. The values $({y_i}^j)_k$ do not fulfill the equations A.21 - A.26:

$$ {A_i}^j(k) \neq 0, \qquad i = 1, ..., 4, \quad j = 3, ..., N$$

$$B_i(k) \neq 0, \qquad i = 1, ..., 4,$$

$$C_i(k) \neq 0, \qquad i = 1, 2. \tag{A.28}$$

Therefore we have to find new values nearer to the right ones. We write the values with the index $k+1$:

$$({y_i}^j)_{k+1} = ({y_i}^j)_k + \delta {y_i}^j \tag{A.29}$$

where $\delta {y_i}^j$ are the difference from the right solution. Substituded into the equations A.18 - A.26, $({y_i}^j)_{k+1}$ produce the changes the left hand sides in these equations: ${A_i}^j(k+1) = {A_i}^j(k) + \delta {A_i}^j$ etc. The new values are required to fulfill the equations A.18 - A.26:

$$\begin{aligned} {A_i}^j(k) + \delta {A_i}^j = 0, \qquad & i = 1, ..., 4 \quad j = 3, ..., N \\ B_i(k) + \delta B_i = 0, \qquad & i = 1, ..., 4 \\ C_i(k) + \delta C_i = 0, \qquad & i = 1, 2. \end{aligned} \tag{A.30}$$

For example, $\delta {A_i}^j$ is written as:

$$\delta A_i^j = \sum_{l=1}^{4} \frac{\partial A_i^j}{\partial y_l^j} \delta y_l^j + \sum_{l=1}^{4} \frac{\partial A_i^j}{\partial y_l^{j-1}} \delta y_l^{j-1} + O((\delta y)^2). \tag{A.31}$$

For small δy_i^j, we can neglect the term $O((\delta y)^2)$ and leave only the linear terms and rewrite the equations A.30:

$$\begin{aligned} \sum_{l=1}^{2} \frac{\partial B_i}{\partial y_l^1} \delta y_l^1 + \sum_{l=1}^{4} \frac{\partial B_i}{\partial y_l^2} \delta y_l^2 &= -B_i \qquad i = 1, ..., 4 \\ \sum_{l=1}^{4} \frac{\partial A_i^j}{\partial y_l^j} \delta y_l^j + \sum_{l=1}^{4} \frac{\partial A_i^j}{\partial y_l^{j-1}} \delta y_l^{j-1} &= -{A_i}^j(k) \qquad i = 1, ..., 4, \quad j = 3, ..., N \\ \sum_{l=1}^{4} \frac{\partial C_i}{\partial y_l^N} \delta y_l^N &= -{C_i}^j(k) \qquad i = 1, 2. \end{aligned} \tag{A.32}$$

These series of equations can be written in matrix form as

$$\boldsymbol{H}\begin{pmatrix} \delta y_1^1 \\ \delta y_2^1 \\ \delta y_1^2 \\ \delta y_2^2 \\ \delta y_3^2 \\ \delta y_4^2 \\ \cdot \\ \cdot \\ \cdot \\ \delta y_1^N \\ \delta y_2^N \\ \delta y_3^N \\ \delta y_4^N \end{pmatrix} = - \begin{pmatrix} \boldsymbol{B} \\ \boldsymbol{A^3} \\ \cdot \\ \cdot \\ \cdot \\ \boldsymbol{A^N} \\ \boldsymbol{C} \end{pmatrix}. \tag{A.33}$$

Here we unite four variables, $A_1^j, A_2^j, A_3^j, A_4^j$ as $\boldsymbol{A^j}$, B_1, B_2, B_3, B_4 as $\boldsymbol{B}$, and C_1, C_2 as $\boldsymbol{C}$, respectively. The $4N \times 4N$ matrix H is what we call the Henyey matrix

$$\begin{pmatrix} \boldsymbol{E_1} & \boldsymbol{E_2} & & & & & 0 \\ & \boldsymbol{G_3} & \boldsymbol{H_3} & & & & \\ & & \boldsymbol{G_4} & \boldsymbol{H_4} & & & \\ & & \cdots & \cdots & & & \\ & & & & \cdots & \cdots & \\ & & & & & \boldsymbol{G_N} & \boldsymbol{H_N} \\ 0 & & & & & & \boldsymbol{F} \end{pmatrix} \tag{A.34}$$

where

$$\boldsymbol{E_1} = \begin{pmatrix} \frac{\partial B_1}{\partial y_1^1} & \frac{\partial B_1}{\partial y_2^1} \\ \frac{\partial B_2}{\partial y_1^1} & \frac{\partial B_2}{\partial y_2^1} \\ \frac{\partial B_3}{\partial y_1^1} & \frac{\partial B_3}{\partial y_2^1} \\ \frac{\partial B_4}{\partial y_1^1} & \frac{\partial B_4}{\partial y_2^1} \end{pmatrix} \tag{A.35}$$

$$\boldsymbol{E_2} = \begin{pmatrix} \frac{\partial B_1}{\partial y_1^2} & \frac{\partial B_1}{\partial y_2^2} & \frac{\partial B_1}{\partial y_3^2} & \frac{\partial B_1}{\partial y_4^2} \\ \frac{\partial B_2}{\partial y_1^2} & \frac{\partial B_2}{\partial y_2^2} & \frac{\partial B_2}{\partial y_3^2} & \frac{\partial B_2}{\partial y_4^2} \\ \frac{\partial B_3}{\partial y_1^2} & \frac{\partial B_3}{\partial y_2^2} & \frac{\partial B_3}{\partial y_3^2} & \frac{\partial B_3}{\partial y_4^2} \\ \frac{\partial B_4}{\partial y_1^2} & \frac{\partial B_4}{\partial y_2^2} & \frac{\partial B_4}{\partial y_3^2} & \frac{\partial B_4}{\partial y_4^2} \end{pmatrix} \tag{A.36}$$

$$\boldsymbol{G_j} = \begin{pmatrix} \frac{\partial A_1^{j-1}}{\partial y_1^{j-1}} & \frac{\partial A_1^{j-1}}{\partial y_2^{j-1}} & \frac{\partial A_1^{j-1}}{\partial y_3^{j-1}} & \frac{\partial A_1^{j-1}}{\partial y_4^{j-1}} \\ \frac{\partial A_2^{j-1}}{\partial y_1^{j-1}} & \frac{\partial A_2^{j-1}}{\partial y_2^{j-1}} & \frac{\partial A_2^{j-1}}{\partial y_3^{j-1}} & \frac{\partial A_2^{j-1}}{\partial y_4^{j-1}} \\ \frac{\partial A_3^{j-1}}{\partial y_1^{j-1}} & \frac{\partial A_3^{j-1}}{\partial y_2^{j-1}} & \frac{\partial A_3^{j-1}}{\partial y_3^{j-1}} & \frac{\partial A_3^{j-1}}{\partial y_4^{j-1}} \\ \frac{\partial A_4^{j-1}}{\partial y_1^{j-1}} & \frac{\partial A_4^{j-1}}{\partial y_2^{j-1}} & \frac{\partial A_4^{j-1}}{\partial y_3^{j-1}} & \frac{\partial A_4^{j-1}}{\partial y_4^{j-1}} \end{pmatrix} \qquad j = 3, ..., N \tag{A.37}$$

$$\boldsymbol{H_j} = \begin{pmatrix} \frac{\partial A_1^{j-1}}{\partial y_1^j} & \frac{\partial A_1^{j-1}}{\partial y_2^j} & \frac{\partial A_1^{j-1}}{\partial y_3^j} & \frac{\partial A_1^{j-1}}{\partial y_4^j} \\ \frac{\partial A_2^{j-1}}{\partial y_1^j} & \frac{\partial A_2^{j-1}}{\partial y_2^j} & \frac{\partial A_2^{j-1}}{\partial y_3^j} & \frac{\partial A_2^{j-1}}{\partial y_4^j} \\ \frac{\partial A_3^{j-1}}{\partial y_1^j} & \frac{\partial A_3^{j-1}}{\partial y_2^j} & \frac{\partial A_3^{j-1}}{\partial y_3^j} & \frac{\partial A_3^{j-1}}{\partial y_4^j} \\ \frac{\partial A_4^{j-1}}{\partial y_1^j} & \frac{\partial A_4^{j-1}}{\partial y_2^j} & \frac{\partial A_4^{j-1}}{\partial y_3^j} & \frac{\partial A_4^{j-1}}{\partial y_4^j} \end{pmatrix}$$

$$j = 3, ..., N \tag{A.38}$$

$$\boldsymbol{F} = \begin{pmatrix} \frac{\partial C_1}{\partial y_1^N} & \frac{\partial C_1}{\partial y_2^N} & \frac{\partial C_1}{\partial y_3^N} & \frac{\partial C_1}{\partial y_4^N} \\ \frac{\partial C_2}{\partial y_1^N} & \frac{\partial C_2}{\partial y_2^N} & \frac{\partial C_2}{\partial y_3^N} & \frac{\partial C_2}{\partial y_4^N} \end{pmatrix}. \tag{A.39}$$

Dividing the matrix into blocks

The Henyey matrix H has non-zero elements only overlapping areas along the diagonal. We can make use of this characteristics of this structure and divide the $4N-2$ equations into N sets.

For the first set we pick up the four equations for $j = 1$ (first 4 lines of the Henyey matrix), i.e., $\boldsymbol{E_1}$ and $\boldsymbol{E_2}$:

$$(\boldsymbol{P_1}) \begin{pmatrix} \delta y_1^1 \\ \delta y_2^1 \\ \delta y_1^2 \\ \delta y_2^2 \end{pmatrix} + (\boldsymbol{Q_1}) \begin{pmatrix} \delta y_3^2 \\ \delta y_3^4 \\ \delta y_1^3 \\ \delta y_2^3 \end{pmatrix} = \quad - \quad (\boldsymbol{B}) \tag{A.40}$$

where

$$\boldsymbol{P_1} = \begin{pmatrix} \frac{\partial B_1}{\partial y_1^1} & \frac{\partial B_1}{\partial y_2^1} & \frac{\partial B_1}{\partial y_1^2} & \frac{\partial B_1}{\partial y_2^2} \\ \frac{\partial B_2}{\partial y_1^1} & \frac{\partial B_2}{\partial y_2^1} & \frac{\partial B_2}{\partial y_1^2} & \frac{\partial B_2}{\partial y_2^2} \\ \frac{\partial B_3}{\partial y_1^1} & \frac{\partial B_3}{\partial y_2^1} & \frac{\partial B_3}{\partial y_1^2} & \frac{\partial B_3}{\partial y_2^2} \\ \frac{\partial B_4}{\partial y_1^1} & \frac{\partial B_4}{\partial y_2^1} & \frac{\partial B_4}{\partial y_1^2} & \frac{\partial B_4}{\partial y_2^2} \end{pmatrix} \tag{A.41}$$

$$\boldsymbol{Q_1} = \begin{pmatrix} \frac{\partial B_1}{\partial y_3^2} & \frac{\partial B_1}{\partial y_4^2} & 0 & 0 \\ \frac{\partial B_2}{\partial y_3^2} & \frac{\partial B_2}{\partial y_4^2} & 0 & 0 \\ \frac{\partial B_3}{\partial y_3^2} & \frac{\partial B_3}{\partial y_4^2} & 0 & 0 \\ \frac{\partial B_4}{\partial y_3^2} & \frac{\partial B_4}{\partial y_4^2} & 0 & 0 \end{pmatrix}. \tag{A.42}$$

Here we define

$$\boldsymbol{\eta^1} = \begin{pmatrix} \delta y_1^1 \\ \delta y_2^1 \\ \delta y_1^2 \\ \delta y_2^2 \end{pmatrix}, \quad \boldsymbol{\eta^2} = \begin{pmatrix} \delta y_3^2 \\ \delta y_4^2 \\ \delta y_1^3 \\ \delta y_2^3 \end{pmatrix}. \tag{A.43}$$

Equation A.40 can be written as

$$\boldsymbol{\eta^1} + \boldsymbol{\Gamma_1}\boldsymbol{\eta^2} + \boldsymbol{\gamma_1} = 0. \tag{A.44}$$

where

$$\begin{aligned} \boldsymbol{\Gamma_1} &= \boldsymbol{P_1}^{-1}\boldsymbol{Q_1} \\ \boldsymbol{\gamma_1} &= \boldsymbol{P_1}^{-1}\boldsymbol{B}. \end{aligned} \tag{A.45}$$

For $3 \leq j \leq N$ we pick up $\boldsymbol{G_1}$ and $\boldsymbol{H_1}$

$$\boldsymbol{R_j}\boldsymbol{\eta^{j-1}} + \boldsymbol{P_j}\boldsymbol{\eta^j} + \boldsymbol{Q_j}\boldsymbol{\eta^{j+1}} = -\boldsymbol{A^j} \tag{A.46}$$

where

$$\boldsymbol{R_j} = \begin{pmatrix} 0 & 0 & \frac{\partial A_1^j}{\partial y_1^{j-1}} & \frac{\partial A_1^j}{\partial y_2^{j-1}} \\ 0 & 0 & \frac{\partial A_2^j}{\partial y_1^{j-1}} & \frac{\partial A_2^j}{\partial y_2^{j-1}} \\ 0 & 0 & \frac{\partial A_3^j}{\partial y_1^{j-1}} & \frac{\partial A_3^j}{\partial y_2^{j-1}} \\ 0 & 0 & \frac{\partial A_4^j}{\partial y_1^{j-1}} & \frac{\partial A_4^j}{\partial y_2^{j-1}} \end{pmatrix} \tag{A.47}$$

$$\boldsymbol{P_j} = \begin{pmatrix} \frac{\partial A_1^j}{\partial y_3^{j-1}} & \frac{\partial A_1^j}{\partial y_4^{j-1}} & \frac{\partial A_1^j}{\partial y_1^j} & \frac{\partial A_1^j}{\partial y_2^j} \\ \frac{\partial A_2^j}{\partial y_3^{j-1}} & \frac{\partial A_2^j}{\partial y_4^{j-1}} & \frac{\partial A_2^j}{\partial y_1^j} & \frac{\partial A_2^j}{\partial y_2^j} \\ \frac{\partial A_3^j}{\partial y_3^{j-1}} & \frac{\partial A_3^j}{\partial y_4^{j-1}} & \frac{\partial A_3^j}{\partial y_1^j} & \frac{\partial A_3^j}{\partial y_2^j} \\ \frac{\partial A_4^j}{\partial y_3^{j-1}} & \frac{\partial A_4^j}{\partial y_4^{j-1}} & \frac{\partial A_4^j}{\partial y_1^j} & \frac{\partial A_4^j}{\partial y_2^j} \end{pmatrix} \tag{A.48}$$

$$\boldsymbol{Q_j} = \begin{pmatrix} \frac{\partial A_1^j}{\partial y_3^j} & \frac{\partial A_1^j}{\partial y_4^j} & 0 & 0 \\ \frac{\partial A_2^j}{\partial y_3^j} & \frac{\partial A_2^j}{\partial y_4^j} & 0 & 0 \\ \frac{\partial A_3^j}{\partial y_3^j} & \frac{\partial A_3^j}{\partial y_4^j} & 0 & 0 \\ \frac{\partial A_4^j}{\partial y_3^j} & \frac{\partial A_4^j}{\partial y_4^j} & 0 & 0 \end{pmatrix}. \tag{A.49}$$

(A.50)

and

$$\boldsymbol{\eta^j} = \begin{pmatrix} \delta y_3^{j-1} \\ \delta y_4^{j-1} \\ \delta y_1^j \\ \delta y_2^j \end{pmatrix}, \quad j = 3, ..., N \tag{A.51}$$

$\boldsymbol{\eta^2}$ is defined in equation A.43.

If there is a relation

$$\boldsymbol{\eta^{j-1}} + \boldsymbol{\Gamma_{j-1}\eta^j} + \boldsymbol{\gamma_{j-1}} = 0, \quad j \geq 3 \tag{A.52}$$

then we obtain

$$\boldsymbol{\eta^j} + (\boldsymbol{P^j} - \boldsymbol{R^j\Gamma_{j-1}})^{-1}(\boldsymbol{Q^j\eta^{j+1}} - \boldsymbol{R^j\eta^{j-1}} + \boldsymbol{A^j}) = 0 \tag{A.53}$$

by substituting equation A.52 into equation A.46 if we define

$$\begin{aligned} \boldsymbol{\Gamma_j} &= (\boldsymbol{P^j} - \boldsymbol{R^j\Gamma_{j-1}})^{-1}\boldsymbol{Q^j} \\ \boldsymbol{\gamma_j} &= (\boldsymbol{P^j} - \boldsymbol{R^j\Gamma_{j-1}})^{-1}(-\boldsymbol{R^j\eta^{j-1}} + \boldsymbol{A^j}) \end{aligned} \tag{A.54}$$

and replace index j of $j-1$ equation A.46 is reproduced. Equation A.54 means we can obtaion Γ_j and γ_j if we know Γ_{j-1} and γ_{j-1} $(3 \leq j \leq N)$. We already know Γ_1 and γ_1 by equation A.45, so Γ_j and γ_j can obtained one after another.

For $j = N+1$ $(m = m_F)$, we pick up the last two lines of the Henyey matrix

$$\boldsymbol{F} \begin{pmatrix} \delta y_1^N \\ \delta y_2^N \\ \delta y_3^N \\ \delta y_4^N \end{pmatrix} = -\boldsymbol{C}. \tag{A.55}$$

With this, δy_1^N and δy_2^N are expressed as a function of δy_3^N and δy_4^N. Here δy_3^N and δy_4^N are determined by fitting condition between inner and outer (envelope) solutions. Equation A.53 means that $\boldsymbol{\eta^j}$ can be obtained if we find $\boldsymbol{\eta^{j+1}}$. We can write equation A.52 for $j = N$

$$\boldsymbol{\eta^{N-1}} + \boldsymbol{\Gamma_{N-1}\eta^N} + \boldsymbol{\gamma_{N-1}} = 0. \tag{A.56}$$

Therefore we can obtain $\boldsymbol{\eta^{N-1}}$, $\boldsymbol{\eta^{N-2}}$, ..., $\boldsymbol{\eta^1}$ one after another.

A.4 Fitting of the two integrations

The two solutions (inner and outer) have to coinside with each other at a certain point, fitting point $m_{\rm F}$. The inner solution is integrated outward from the centar by Henyey method deescribed the previous section, and the outer solution is by inward integration from the surface by Runge-Kutta method.

The parameters to be corrected are four, i.e., y_3^N, y_4^N, L, and R. One needs three conditions, and they are written as follows:

$$V_{\rm in}(y_1^N,\ y_2^N,\ y_3^N,\ y_4^N)(=V^N) = V_{\rm ex}(R,\ L) \tag{A.57}$$

$$W_{\rm in}(y_1^N,\ y_2^N,\ y_3^N,\ y_4^N)(=W^N) = W_{\rm ex}(R,\ L) \tag{A.58}$$

$$\log\rho_{\rm in}(y_1^N,\ y_2^N,\ y_3^N,\ y_4^N)(=\log\rho^N) = \log\rho_{\rm ex}. \tag{A.59}$$

As y_1^N and y_2^N are expressed in terms of y_3^N and y_4^N, and L is assumed to be equal with y_4^N, these conditions are expressed as functions of y_3^N, y_4^N, and $\delta\log R$ (R

is expressed in log scale). Then we obtain three linear equations for fitting:

$$\frac{\partial V^N}{\partial y_3^N}\delta y_3^N + \frac{\partial V^N}{\partial y_4^N}\delta y_4^N - \frac{\partial V_{\rm ex}}{\partial y_4^N}\delta y_4^N - \frac{\partial V_{\rm ex}}{\partial \delta \log R}\delta \log R = V_{\rm ex} - V^N \tag{A.60}$$

$$\frac{\partial W^N}{\partial y_3^N}\delta y_3^N + \frac{\partial W^N}{\partial y_4^N}\delta y_4^N - \frac{\partial W_{\rm ex}}{\partial y_4^N}\delta y_4^N - \frac{\partial W_{\rm ex}}{\partial \delta \log R}\delta \log R = W_{\rm ex} - W^N \tag{A.61}$$

$$\frac{\partial \log \rho^N}{\partial y_3^N}\delta y_3^N + \frac{\partial \log \rho^N}{\partial y_4^N}\delta y_4^N - \frac{\partial \log \rho_{\rm ex}}{\partial y_4^N}\delta y_4^N - \frac{\partial \log \rho_{\rm ex}}{\partial \delta \log R}\delta \log R = \log \rho_{\rm ex} - \log \rho^N. \tag{A.62}$$

We can obtain $\delta y_3^N, \delta y_4^N$, and $\delta \log R$ from the above three equations. Using δy_3^N and δy_4^N, we can obtain all the other variables η^j $(2 \leq j \leq N)$ one after another due to Equation A.52. We can solve outer region by setting the new outer values $\log R + \delta \log R$ and $L + \delta L = y_4^N + \delta y_4^N$. We repeat the above process and obtain corrected solutions until the correction $|\delta y_i^j / y_i^j|$ become small enough.

REFERENCES

Abel, T., Bryan, G.L., & Norman, M.L. 2000, ApJ, 540, 39

Abel, T., Bryan, G.L., & Norman, M.L. 2002, Science, 295, 93

Ahn, K., & Shapiro, P. R. 2007, MNRAS, 375, 881

Baraffe, I., Heger, A., & Woosley, S. E. 2001, ApJ, 550, 890

Barkat, Z., Rakavy, G., & Sack, N. 1967, Phys. Rev. Letters, 18, 379

Barth, A. J., Green, J. E., & Ho, L. C. 2005, in Growing Black Holes, eds. A. Merloni, S. Nayakshin, & R. A. Sunyaev (Springer), 154

Begelman, M., Volonteri, M., & Rees, M.J. 2006, MNRAS, 370, 289

Bender, R. 2005, in Growing Black Holes, eds. A. Merloni, S. Nayakshin, & R. A. Sunyaev (Springer)

Bond, J. R., Arnett, W. D., & Carr, B. J. 1984, ApJ, 280, 825

Bromm, V., Coppi, P.S., & Larson, R.B. 1999, ApJ, 527, L5

Bromm, V., Coppi, P.S., & Larson, R.B. 2002, ApJ, 564, 23

Bromm, V., & Larson, R.B. 2003, ARA&A, 42, 79

Bromm, V., & Loeb, A. 2003, ApJ, 596, 34

Bromm, V., & Loeb, A. 2004, NewA, 9, 353

Cayrel, R., et al. 2004, A&A, 416, 1117

Chieffi, A., & Lomongi, M. 2002, ApJ, 577, 281

Colbert, E. J. M., & Mushotzky, R. F. 1999, ApJ, 519, 89

Couchman, H. M. P., & Rees, M. J. 1986, MNRAS, 221, 53

Ebisuzaki, T., et al. 2001, ApJ, 562, L19

Ekström, S., Meynet, G., & Maeder, A. 2006, in ASP Conf. Series, Vol. 353, Stellar Evolution at Low Metallicity: Mass Loss, Explosions, Cosmology, eds. H. J. G. L. M. Lamers, N. Langer, T. Nugis, & K. Annuk, 141

Ekström, S., Meynet, G., Chiappini, C, Hirschi, R., & Maeder, A. 2008, A&A, 489, 685

Fan, X. 2006, New Astronomy Reviews, 50, 665

Fryer, C. L., Woosley, S. E., & Heger, A. 2001, ApJ, 550, 372

Fuller, T. M., & Couchman, H. M. P. 2000, ApJ, 544, 6

Gao, L., Yoshida, N., Abel, T., Frenk, C. S., Jenkins, A., & Springel, V. 2007, Mon. Not. R. Astron. Soc. 378, 449

Glatzel, W., Fricke, K. J., & El Eid, M. F. 1985, A&A, 149, 413

Hansen, B., & Milosavljevic, M. 2004, ApJ, 593, L77

Heger, A., Baraffe, I., Fryer, C.L., Woosley, S.E. 2001, Nuc. Phys. A., 688, 197

Heger, A., & Woosley, S. E. 2002, ApJ, 567, 532

Heger, A., Fryer, C.L., Woosley, S.E., Langer, N., & Hartmann, D. H. 2003, ApJ, 591, 288

Heger, A., Woosley, S. E., & Baraffe, I. 2005, in The Fate of the Most Massive Stars, eds. R. Humphreys and K. Stanek (ASP Conference Series, Vol. 332), 347

Heger, A., & Woosley, S. E. 2008, arXiv:0803.3161

Henyey, L. G., Forbes, J. E., & Gould, N. L. 1964, ApJ, 139, 306

Haiman, Z., Thoul, A. A., & Loeb, A. 1996, ApJ, 464, 523

Hirschi, R. 2007, A&A, 461, 571

Hirschi, R. 2008, in Clumping in Hot Winds, eds. W.-R. Hamann, A. Feldmeier, & L. M. Oskinova, 9

Hix, W. R. & Thielemann, F.-K. 1996, ApJ, 460, 869

Iwamoto, N., Umeda, H., Tominaga, N., Nomoto, K., & Maeda, K. 2005, Science, 309, 451

Johnson, J. L., Greif, T. H., & Bromm, V. 2008, MNRAS, 388, 26

Kudritzki, R.-P. 2000, in The First Stars. eds. A. Weiss, T. G. Abel, & V. Hill (Berlin: Springer), 127

Kirshner, R. P. 2003, Science, 300, 1914

Kippenhahn, R., Weigert, A., & Hofmeister, E. 1967, in 'Methods in Computational Physics', 129

Kormendy, J., & Richstone, D. 1995, ARA&A, 33, 581

Li, Y. et al., 2007, ApJ, 665, 187

Li, Y. et al., 2008, ApJ, 678, 41

Limongi, M., & Chieffi, A. 2003, ApJ, 592, 404

Madau, P & Rees, M. J. 2001, ApJ, 551, L27

Makishima, K et al. 2000, ApJ, 535, 632

Makishima, K. 2008, in Black Holes: from Stars to Galaxies, eds. V. Karas, et al. (Cambridge University Press), in press

Marchant, A. B., & Shapiro, S. L. 1980, ApJ, 239, 685

Marigo, P., Girardi, L., Chiosi, C., & Wood, P. 2001, A&A, 371, 152

Matsuda, T., Sato, H., & Takeda, H. 1969, Prog. Theor. Phys., 42, 219

Matsumoto, H., Tsuru, T, G., Koyama, K., Awaki, K., Canizares, C. R., Kawai, N., Matsushita, S., & Kawabe, R. 2001, ApJ, 547, L25

McKee, C. F., & Tan, J. C. 2008, ApJ, 681, 771

Meynet, G., Ekström, S., & Maeder, A. 2006, A&A, 447, 623

Micic, M., Holley-Bockelmann, K., Sigurdsson, S., & Abel, T. 2007, MNRAS, 380, 1533M

Nakamura, F. & Umemura, M. 1999, ApJ, 515, 239

Nakamura, F. & Umemura, M. 2002, ApJ, 569, 549

Nakazato, K., Sumiyhoshi, K., & Yamada, S. 2006, ApJ, 645, 519

Neo, S., Miyaji, S., Nomoto, K., & Sugimoto, D. 1976, PASJ, 29, 249

Nomoto, K. 1982, ApJ, 253, 798

Nomoto, K. & Hashimoto, M. 1988, Phys. Rep., 163, 13

Ober, W. W., El Eid, M. F., & Fricke, K. J. 1983, A&A, 119, 61

Ohkubo, T., Umeda, H., Maeda, K., Nomoto, K., Suzuki, T., Tsuruta, S., & Rees, M. J. 2006, ApJ, 645, 1352

Omukai, K. & Nishi, R. 1998, ApJ, 508, 141

Omukai, K. & Palla, F. 2003, ApJ, 589, 677

O'Shea, B. W., & Norman, M. L. 2006a, ApJ, 648, 31

O'Shea, B. W., & Norman, M. L. 2006b, ApJ, 654, 66

Ostriker, J. P. & Steinhardt, P. 2003, Science, 300, 1909

Palla, F., Salpeter, E. E., & Stahler, S. W. 1983, ApJ, 271, 632

Peebles, P. J. E., & Dicke, R. H. 1968, ApJ, 154, 891

Plowman, J., Jacobs, D.C., Hellings, R.W, Tsuruta, S., & Larson, S.L. 2008, in preparation

Portegies Zwart, S. F., Makino, J., McMillan, S. L. W., & Hut, P. 1999, A&A, 348, 117

Portegies Zwart, S. F., Baumgardt, H., Hut, P., Makino,J., & McMillan, S.L.W. 2004, Nature, 428, 724

Portegies Zwart, S.F. 2004, in Joint Evolution of Black Holes and Galaxies, eds. M. Colpi, V. Gorini, F. Haardt & U. Moschella (Bristol and Philadelphia: IOP Publishing), in press (astro-ph/0406550)

Qian, Y.-Z, Sargent, W.L.W., & Wasserburg, G.J. 2002, ApJ, 588, 1099

Qian, Y.-Z, & Wasserburg, G.J. 2002, ApJ, 567, 515

Rakavy, G., Shaviv, G., & Zinamon, Z. 1967, ApJ, 150, 131

Rakavy, G., & Shaviv, G. 1968, Astrophys. Space Sci, 1, 429

Rees, M. J. 2002, in Lighthouses of the universe: Most Luminous Celestial Objects and Their Use for Cosmology, eds. M. Gilfanov, R. Sunyaev, & E. Churazov (Springer), 345

Rees, M. J. 2003, in The Future of Theoretical Physics and Cosmology, eds. G. W. Gibbons, E. P. S. Shellard, & S. J. Rankin, 217

Sanchez, N., et al. 2006, MNRAS, 366, 189

Sesana, A., Volonteri, M., & Haardt, F. 2007, MNRAS, 337, 1711S

Spergel, V., et al. 2007, ApJS, 170, 377

Spruit, H. C. 1992, A&A, 131

Stahler, S. W., Palla, F., & Salpeter, E. E. 1986, ApJ, 302, 590

Sugimoto, D., & Nomoto, K. 1975, PASJ, 27, 197

Suwa, Y., Takiwaki, T., Kotake, K., & Sato, K. 2006, AIPC, 847, 476

Suwa, Y., Takiwaki, T., Kotake, K., & Sato, K. 2007, ApJ, 665, 43

Tan, J. C., & McKee, C. F. 2004, ApJ, 603, 383

Tanaka, T. & Haiman, Z 2008, AstroPh arXiv: 0807.4702v1

Tegmark, M., Silk, J., Rees, M. J., Blanchard, A., Abel, T., & Palla, F. 1997, ApJ, 474, 1

Tominaga, N., Umeda, H., & Nomoto, K. 2007, ApJ, 660, 516

Tsuribe, T. & Inutsuka, S. 2001, Ap&SS, 276, 1097

Umeda, H., Nomoto, K., & Nakamura, T. 1999, in The First Stars, eds. A. Weiss et al. (Berlin: Springer), 150 (astro-ph/9912248)

Umeda, H. & Nomoto, K. 2002, ApJ, 565, 385

Umeda, H. & Nomoto, K. 2005, ApJ, 619, 427

Umeda, H. & Nomoto, K. 2008, ApJ, 673, 1014

Volonteri, M., Madau, P., & Haardt, F. 2003, ApJ, 593, 661

Volonteri, M. & Rees, M.J. 2006, ApJ, 650, 669

Yoshida, N., Abel, T., Hernquist, L., & Sugiyama, N. 2003, ApJ, 592, 645

Yoshida, N., Omukai, K., Hernquist, L., & Able, T. 2006, ApJ, 652, 6

Yoshida, N., Oh, S. P., Kitayama, T., & Hernquist, L. 2007, ApJ, 663, 687

Yoshida, N., Omukai, K., & Hernquist, L. 2008, Science, 321, 669

Wasserburg , G.J., & Qian, Y.-Z. 2000, ApJ, 529, L21

Woosley, S. E. 1986, in Nucleosynthesis and Chemical Evolution eds. B. Hauck, A. Maeder, & G. Meynet (Switzerland:Geneva Obs.), 1

Woosley, S. E., Blinnikov, S., & Heger, A. 2007, Nature, 450, 390